Title
Thermal Imaging of Single Living Cells Using Semiconductor Quantum Dots

Author
Yang, Jui-Ming

Publication Date
2009

Peer reviewed|Thesis/dissertation

Thermal Imaging of Single Living Cells Using Semiconductor Quantum Dots

by

Jui-Ming Yang

A dissertation submitted in partial satisfaction of the

requirements for the degree of

Doctor of Philosophy

in

Engineering – Mechanical Engineering

in the

Graduate Division

of the

University of California, Berkeley

Committee in charge:

Professor Liwei Lin, Chair

Professor Albert P. Pisano

Professor Ming C. Wu

Fall 2009

Thermal Imaging of Single Living Cells Using Semiconductor Quantum Dots

by

Jui-Ming Yang

Abstract

Thermal Imaging of Single Living Cells Using Semiconductor Quantum Dots

by

Jui-Ming Yang

Doctor of Philosophy in Engineering – Mechanical Engineering

University of California, Berkeley

Professor Liwei Lin, Chair

Direct observation of temperature distributions inside single living cells is a challenging yet fundamental research topic. In this work, semiconductor nanocrystalline quantum dots (QDs) were introduced as tiny temperature markers and three distinctive achievements have been accomplished: (1) optical property characterizations of QDs with respect to temperature and chemical changes inside single living cells; (2) temperature characterizations of micro heaters using QDs; and (3) imaging of thermogenesis inside single living cells due to chemical and thermal stresses.

The spectral shift of a single CdSe/ZnS core shell QD coated with a layer of organic polymer, and conjugated with streptavidin, was successfully characterized as 0.1 nm/°C around room-temperature. Empirical relations and statistical analyses concluded that about 1200 QDs are required to achieve 1°C statistical measurement precision in optical readouts. The proof-of-concept experiment utilized QDs to characterize the temperature distributions of a MEMS heater. Both experimental and simulation results showed good consistency and a 267 nm spatial resolution has been achieved.

QDs with central emission wavelength at ~655 nm were delivered to living cells by endocytosis and distributed in the form of vesicles in the cytoplasm. Their temperature-dependent spectral shift was measured and characterized with a linear relationship at 0.06 nm/°C. It was also observed that pH variations due to chemical changes have little effects on the spectra shift of QDs.

Thermogenesis of single living cell with respect to external chemical and temperature stresses were investigated. NIH/3T3 cells showed a measureable temperature increase with respect to high concentration of calcium influx. A cold-shock assay was conducted in a 15 min experiment, whereby the ambient temperature of cell culture was precipitously lowered from 37 to 20^{o}C. It is found that single living cells exhibited higher average temperature than the environmental stimulations during the cold-shock experiments. This implies possible heat generation during cold exposure, presumably resulting from the complicated biochemical reaction networks, as a self-defense mechanism. Moreover, the observations of temperature distribution are in sharp contrast between live and dead cells, in both calcium influx and cold shock experiments. It suggests that heat generation is indeed a characteristic of living mammalian cells, with dead intact cells as controls. A negative control experiment using heat-shock was performed and results showed the temperature of NIH/3T3 fibroblasts trace closely with the external environmental temperature in a heating process from 35 to 50^{o}C. Furthermore,

intracellular temperature difference has been observed and recorded as large as 5^{o}C during cold shock experiments.

These experiments demonstrate that quantum dots are capable of mapping intracellular temperature dynamically in single living cells with statistically improved spatial resolution and sensitivity. With no complex experimental setup, this technique could be widely applicable for the thermodynamic studies of single living cells.

Dedicate to my parents.

Contents

Acknowledgements

No man is an island and this is certainly true in graduate school. I would like to thank all the students and professors whom I interacted with at Lin's lab and the Berkeley Sensor and Actuator Center (BSAC). I will attempt to acknowledge them all here but for those whom I inadvertently miss, I humbly issue heartfelt thanks.

I thank my research group in Carnegie Mellon University for preparing my biological backgrounds. I thank Professor Philip R. LeDuc gave me the opportunities to work in an interdisciplinary research area during my master studies. I thank Jim Kubicek and Lab Mays on training me cell culture techniques. I thank Chao-Min Cheng and Theresa Cassino provided great discussion and research ideas.

I thank Takeshi Kawano, Tomonori Fujii, Sha Li, Lei Luo, Kedar Shah, Brian Sosnowchik, Mike (Yiin-Kuen) Fuh for helping and training me on equipment and procedures in the microlab. Ethan (I-Cheng) Chen was a great research partner in the NIST project and always offered me great advice on research. I thank Jonathan Ames and Armon Mahajerin for helping on the NIST project. I would like to thank Peter Yang helped in various lab works and advised on the projects. Ryan Sochol and Armon Mahajerin entertained us with their creative plays.

I would like to thank Sha Li and Kai Zhang for initiate the quantum dots project. I would like to thank Hu Cang helped me on the optical setups and preparations of chemicals. I thank Erika Parra and Adrienne Higa helped on the cellular studies and advice. Special thanks to Qin Zhou for valuable inputs and helpful discussions on my research projects and data analysis.

On the life side, I thank Ting-Ta Yen, Chun-Hung (Simon) Hung, Tsung-Te Liu, Chi-Shen Tsai, Chiung C. Lo, Chieh Chang, Darsen Lu, Emma Yu, Jimmy Chen, Keng-Hao Chang, Wei-Chun Kao, Ricky Chien, Nora Han, Matilda Lai, Yingqi Jiang, and many others brought joy to my life at Berkeley.

I thank my advisor Professor Liwei Lin whom provided the great opportunity to join his group and got me involved in MEMS research. I also thank my quals and dissertation committee members Professor Albert. P. Pisano, Ming C. Wu, Haw Yang and Dorian Liepmann for their advice and time.

Finally, I thank my family for always being there and providing a source of strength for me through the thick and thin. I can never repay me parents for supporting me through my graduate studies both in Carnegie Mellon University and UC Berkeley.

Chapter 1
Introduction

1.1 Introduction

Accurate temperature measurement with fine spatial resolution is a challenging engineering problem. Many temperature sensing techniques have been based on the physical property changes of temperature sensing materials such as expansion/contraction of volume, thermo-optical and thermo-electronic properties. Recent developments in microfluidic systems for chemical and biological analyses also require precise temperature measurements in order to monitor their temperature profiles for the control of biological or chemical processes. For instance, precise temperature control over time and/or space is essential for on-chip amplification of DNA sequences by polymerase chain reaction (PCR) [1]. In another case, a strong temperature-dependence and stringent regulations of the embryonic development of *Drosophila melanogaster* was demonstrated using a microfluidic device that generates a temperature differential across the embryos [2]. Non-invasive temperature measurements are generally preferred in biological systems to avoid any possible interference.

The analysis of cell and molecular biology from a thermodynamic perspective, such as heat shock proteins [3-5], is essential to advance the fundamental understanding of cell biology. Heat generation in cellular activities has been studied in various aspects, such as an indicator for specific metabolic heat generation, immunomodulators on cellular activity, intracellular enzyme activity and the effectiveness of drugs [6]. The ability in sensing intracellular temperature distributions dynamically can help analyzing energy expenditure and heat generation inside living cells. This dissertation reports efforts in developing a methodology based on the spectra shift of QDs as tiny thermometers for the thermal imaging of cellular temperature with high spatial resolution.

1.2 Goals of Dissertation

In order to develop a new protocol by using QDs as local temperature markers for temperature measurements, three specific experiments have been planned in sequence as shown in Figure 1.1. The first diagram in Figure 1.1a illustrates temperature characterization of a micro heater by using QDs. Historically, these heaters may have width in the range of a few microns that is smaller than most of the temperature detection limitations. For example, the sizes of typical thermalcouples are much larger than the width of the heaters and the spatial resolutions of infrared sensors are also bigger than a few microns. Here, a thin layer of QDs are placed on top of the micro heater and their spectra shifts are utilized as temperature indicators to measure the temperature changes on the micro heater. Figure 1.1b and c show the second and third experiments using QDs as thermometers inside single living cells with chemical and thermal stresses, respectively. It is well known that chemicals, such as calcium, could stimulate the heat generation of cells. However, there have been no quantitative characterizations on the intracellular temperature changes due to the addition of calcium concentration. The third

experiment is to investigate if the environmental temperature changes such as heat-shock or cold-shock may stimulate cellular responses.

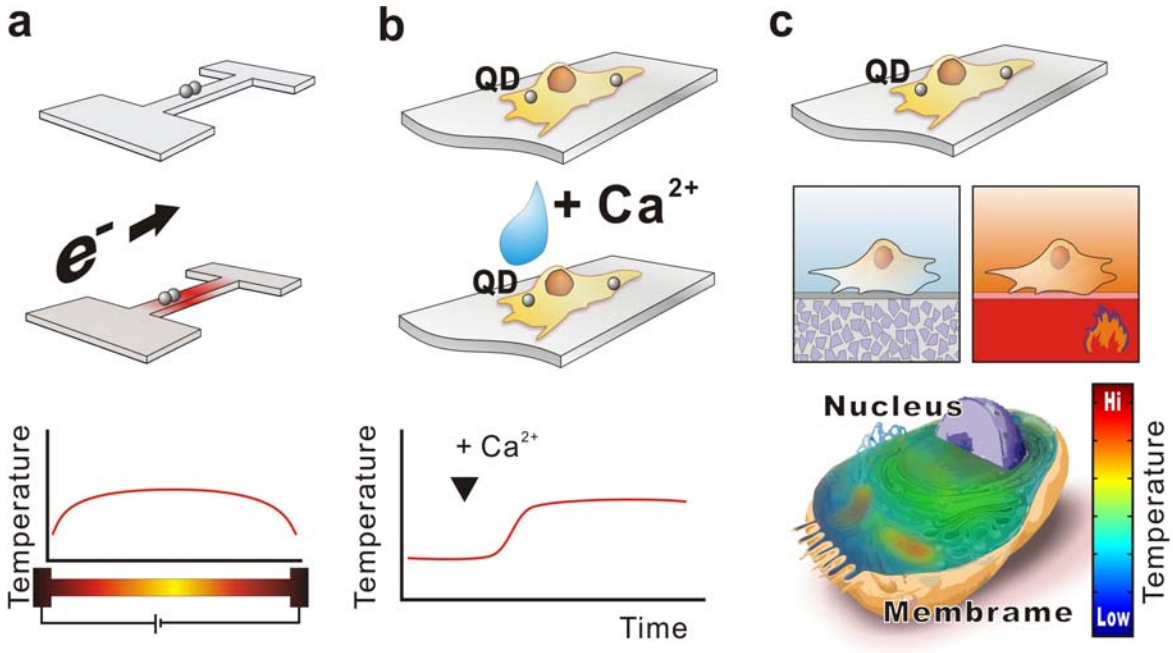

Figure 1.1 Illustration of three temperature measurement experiments via QDs. **a.** Temperature characterization of a micro-heater. **b.** Cellular temperature measurement with respect to chemical stimuli, and **c.** thermal stresses.

Because all levels of biological and biochemical processes are greatly influenced by temperature, including protein folding, diffusion dynamics, biochemical reactions, and membrane permeability, thermal imaging of single living cells is an important basic parameter to be characterized in order to explain various cellular behaviors. At the single cell level, temperature measurement remains a great challenge due to lack of proper tool. The current state-of-the-art tools do not provide good spatial resolution and reading accuracy. The usage of quantum dots as non-contact, far-field temperature sensors can be used to measure local temperature distributions inside living cells. Researchers have reported that the placement of QDs (with bio-compatible coating and/or micelle encapsulation) inside living cells can be realized by passive endocytosis into cytoplasm [7, 8]. QDs with antibodies and specific sub-cellular compartments can also be delivered to specific organelles inside living cells [9, 10]. These advancements provide initial supports for the development of using QDs for local temperature measurements of single living cells.

1.3 Dissertation Outline

In this dissertation, the usage of QDs as temperature indicators is presented. Chapter 2 focuses on the initial characterization of optical properties of QDs. An experimental setup has been developed to detect the emission spectra of the CdSe/ZnS core shell quantum dots.

Individual QDs exhibited a spectra shift with respect to environmental temperature changes for possible temperature sensing applications remotely through optical readout. A line-shape micro-heater was designed and fabricated by metal deposition and lift-off process. When a current is applied to the micro heater, its temperature rises and this effect is recorded as QDs on top of the micro heater will have red shift. Both experimental and simulation results are consistent.

In chapter 3, an experiment has been design to internalize QDs into NIH/3T3 cells. In order to obtain reference temperature for cell surroundings, a protocol was developed to leave portion of QDs remain at the outside of living cells. The properties of temperature dependent of QDs embedded in single cells are detailed and discussed. Several control experiments have been performed to test the potential effects and limitations of using QDs as temperature markers.

In chapter 4, two experiments have been designed to explore the possible applications on cellular temperature measurements. The first approach is to induce the thermogenesis of single living cells with the infusion of calcium ions. A heat generation has been triggered by adding chemical to the culture environment while the temperature profiles of living cells were continuously monitored. The second approach is to use cold shock as an external temperature stimulus for heat generation in single living cells. Cells exhibited a measureable temperature increase in both experiments. Finally, a two-dimensional temperature map of living cells with the infusion of calcium ions was reconstructed by a scanning confocal microscope in a 15-minute experiment.

Chapter 5 concludes various topics of this dissertation and provides a summary of the results. Future research directions are discussed to improve the measurement techniques and to extend potential applications in various fields.

Chapter 2
Quantum Dots as Submicron Temperature Markers

2.1 Introduction

When the characteristic dimension of functional structures reduces down to the nanometer range, it becomes extremely challenging to measure their temperature using conventional techniques either in the contact or in the non-contact modes. For example, a conventional thermocouple could have a spatial resolution of 100 μm [11] while temperature-sensitive paints have spatial resolution in the range of 1 μm [12]. Far field detection scheme is also important in constructing temperature profiles in micro-scales since microstructures are usually fragile and are operated at specific conditions and environments. To extend the potential temperature measurement techniques into biological application, non-invasive tools are essential for probing living organisms without severely interrupting their normal behavior. Temporal resolution of the measurement is another key requirement in temperature studies in microstructures because of reduced thermal time constant. In this chapter, semiconductor nanocrystalline particles, quantum dots (QDs), are used as tiny thermometers by virtue of their small sizes and favorable photostability with far-field optical readouts for temperature measurements in micro- and nanostructures. These luminescence-based sensors are sensitive with temperature variations with the potential for noncontact micro/nano temperature measurements.

In this chapter, literature reviews of various temperature measurement techniques are discussed prior to studies in quantum dots temperature-dependent properties. Physical properties of quantum dots and their applications, both in optoelectronics and biology, are reviewed. The properties of temperature dependence of quantum dots, which can be used as nano-scale thermometers, are detailed and summarized. Characterizations of temperature dependent properties are presented. Finally, a proof-of-concept experiment by using quantum dots as temperature markers is demonstrated.

2.2 Temperature Measurement Techniques

Temperature is one of the fundamental thermodynamic properties. The unit of thermodynamic temperature is Kelvin (K) and is defined in terms of the interval between the absolute zero and triple point of pure water, 273.16 K. Another unit is Celsius (^{o}C) and the magnitude of 1^{o}C is numerically equal to 1 K. A variety of techniques are available for temperature measurement while accurate temperature measurement on the small scale with high spatial resolution is still challenging. Advances in microtechnology and biotechnology desire precise thermometry down to the nanoscale, where conventional methods fail to provide accurate measurements. The development of a nanoscale thermometer has broad impact to a variety of applications. Here, we review several measurement techniques, especially in biological applications, and describe their advantages and limitations.

Microcalorimetry has been used for studying metabolic heat and various aspects of cellular activity, such as the effectiveness of drugs [6, 13], specific metabolic heats [14], and

cellular activity in hyperthyroidism [15]. Although microcalorimeters used for these studies have high thermal resolution, they have poor spatial and temporal resolution as they are used to measure steady-state heat production of large numbers of reactants in suspension. In another example, heat generation associated with potential propagation in neuronal tissue has been studied by pyroelectric films [16], which have high temporal resolution but low spatial resolution. Furthermore, the thermal conductivity between the tissue and the sensor is poor. Microfabricated thermocouples for temperature measurement have been used in microfluidic devices [17-20] and biological samples [21-23]. The usage of a lithographically fabricated or vapor-deposited thermocouple has been developed [24, 25]. The vapor-deposition process is used to deposit one metal onto nanostrips made from another metal, in order to form a nanoscale bimetal sensor. Lithography enables the connection of two p- and n-type nanowire electrodes in the substrate to create nanoscale thermocouples in a parallel array. In these thermometers, the spatial resolution is generally determined by the geometrical size of the thermocouple. However, they all share the same drawback - it constrains the measurements to fixed positions and requires an invasive, contact measurement scheme.

As an alternative to these approaches, spectroscopic methods can provide temperature measurements with submicron spatial resolution by using the temperature dependence of material properties of chemicals [26-33]. For instance, thermochromic liquid crystals (TLC) have been successfully used as thermal probes [31, 34-38], but the high viscosity of TLCs limits their applications. The spatial resolution of TLCs is about 1 μm, limited by the encapsulated particles sizes. Fluorescent dyes are another class of commonly used thermosensitive chemicals, such as rhodamine [33, 39-41], Eu-TTA [42, 43] and others [28, 44-51]. However, measurements are based on the intensity profiles of fluorescence dyes, which are often affected by environmental factors. Furthermore, fluorescent organic dyes bleach quickly in about 30 minutes, such that they are not suitable for applications that require long-term monitoring of temperature. To overcome the drawback of the intensity-based temperature measurement, ratiometric fluorescence techniques and fluorescence lifetime imaging have been demonstrated since the readout signal is independent of intensity [26, 29, 52, 53]. Sakakibara and Adrian [54] further advanced the fluorescence techniques and measured Rayleigh–Benard convection using two-color laser-induced fluorescence with an accuracy of $\pm 0.17^{o}$C. These measurement techniques have strong dependence on pH values and surrounding materials, and are potentially toxic to biological samples. Several groups have attempted to eliminate environmental factors by placing fluorescent dyes into a micropipette [23, 55] which limits spatial resolution of the measurements. Embedding dye molecules in the PDMS matrix has also been reported to reduce the environmental factors [56], but measurement accuracy and time resolution have been affected due to the effect of heat transfer through PDMS matrix.

Infrared (IR) thermography has been used in measuring thermogenesis in large scale cell cultures [57, 58] as well as temperature characterizations for microfluidic chips [59, 60]. However, IR Thermography can only map surface temperatures limiting their applications in cellular studies. Nuclear magnetic resonance (NMR) thermometry has also been used to measure temperatures [61, 62]. A disadvantage of this technique is that the spatial resolution is limited. Recently, a carbon-wrapped nanoscaled thermometer has been explored for temperature sensing in biological environments [63, 64] using NMR, with spatial resolution of 10-30 μm. Another technique is Raman spectroscopy [65, 66]. It offers spatial resolution of 1-5 μm and only probes one point at a time with a slow acquisition rate of 2 second per point. In a different approach,

Brownian motion of submicron particles has been used for temperature measurements [67-70]. However, temperature measurements by Brownian particle displacements has a poor temperature resolution of $\pm 3^{o}C$ [69] and high uncertainty of about 5% [71]. This technique also has strong dependency on the flow and viscosity of fluid.

The use of DNA molecular beacons as temperature probes is a new and fascinating approach [72-74]. Such techniques rely on a thermo-transformable response, leading to high spatial resolution. For example, the change in double-stranded DNA structure from B-DNA to Z-DNA shows potential as a molecular nano-thermometer. Researchers also report that certain messenger RNAs change their conformation in response to temperature [75-77]. However, these measurement techniques require sophisticate measurement equipments, such as nuclear magnetic resonance spectroscopy. Reports have also shown that molecular spring assemblies and superstructures could be applied for thermometry in biological applications. Kotov et al. showed a reversible nano-thermometer comprised of a dynamic superstructure of two types of NP connected by polymeric spacers [78]. The fluorescence intensity change is used to detect the conformation change of polyethyleneglycol (PEG) in the temperature range of 20-60°C [78, 79].

An alternative method is to use luminescent quantum dots (QDs) as the nano-thermometers [80-83]. They can emit stronger fluorescence signals and have higher resistance to photobleach when compared with fluorescent dyes [84]. Furthermore, they respond to temperature changes. For example, CdSe QDs show a spectral shift sensitivity of 0.1 nm/ ^{o}C in the temper[85].

2.3 Quantum Dots Properties

Advances in synthesis of colloidal semiconductor nanocrystalline particles, quantum dots (QDs), have generated great interests for possible applications in the fields of biology and medicine. These nanometer-sized crystalline particles are composed of periodic groups of II–VI (e.g., CdSe) or III–V (e.g., InP) materials. Their size is usually several nanometers in diameter with biological protection and targeting coatings and is suitable for single cell and molecular level studies (Figure 2.1). They are robust fluorescence emitters with tunable emission wavelengths. Their high brightness and resistance to photobleaching enables the use of low power laser for long term observation, making them potentially useful for live-cell imaging, such as consecutive acquisition of z-stacks for high-resolution three-dimensional (3-D) reconstructions over time [86]. Many studies have shown the great potential of using quantum dots as new probes in vitro and in vivo [86, 87]. In this section, the fundamental properties of quantum dots and their bio compatibility are reviewed.

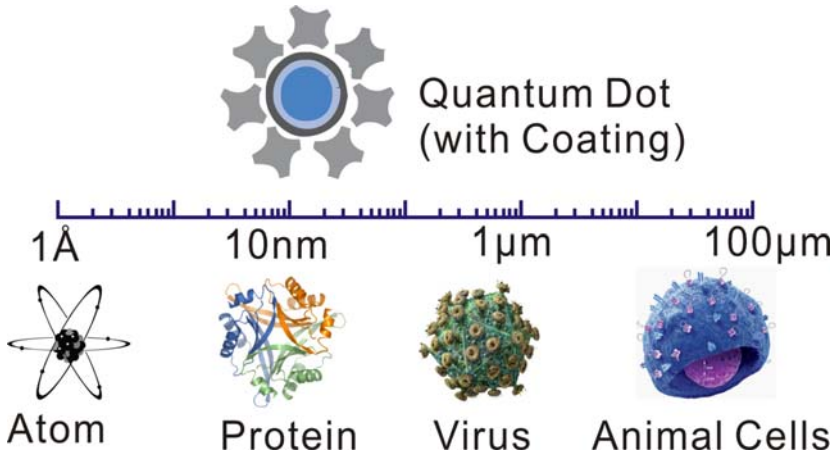

Figure 2.1 Size comparison of semiconductor nanocrystalline particles, or quantum.

2.3.1 Synthesis and Optical Properties

The synthesis of semiconductor nanocrystals, such as CdSe, CdS, or CdTe, can be achieved by injecting liquid precursors into hot coordinating organic solvent [88, 89]. The size of QDs can be adjusted by the amount of precursors and growth time [89]. The quantum yield of the bare nanocrystal core synthesized is relatively low (less than 10%) [90]. A shell of high band-gap semiconductor material, such as ZnS, can be epitaxially grown around the core to achieve higher yield of up to 80% [90].

QDs, which are a few nanometers in diameter, exhibit size dependent energy levels. Band gap energy, from ultraviolet to infrared [87], can be achieved by varying the size and the composition of QDs (Figure 2.2). For example, small QDs (~2 nm) made of CdSe emit in the range between 495 to 515 nm, whereas larger CdSe nanocrystals (~5 nm) emit between 605 and 630 nm. Furthermore, QDs have several different optical properties when compared to organic fluorophores. Organic dyes typically have narrow absorption spectra, which mean they can only be excited within a narrow window of wavelengths and they have asymmetric emission spectra broadened by a red-tail. In contrast, QDs have broad absorption spectra, usually toward to UV region, enabling excitation by a wide range of wavelengths. Their emission spectra are symmetric and narrow because of band-to-band transition. Consequently, multicolor labeling can be achieved by a single excitation source with wavelength shorter than emission wavelengths of QDs. QDs are also very stable light emitters owing to their inorganic composition, making them less susceptible to photobleaching than organic dye molecules [8].

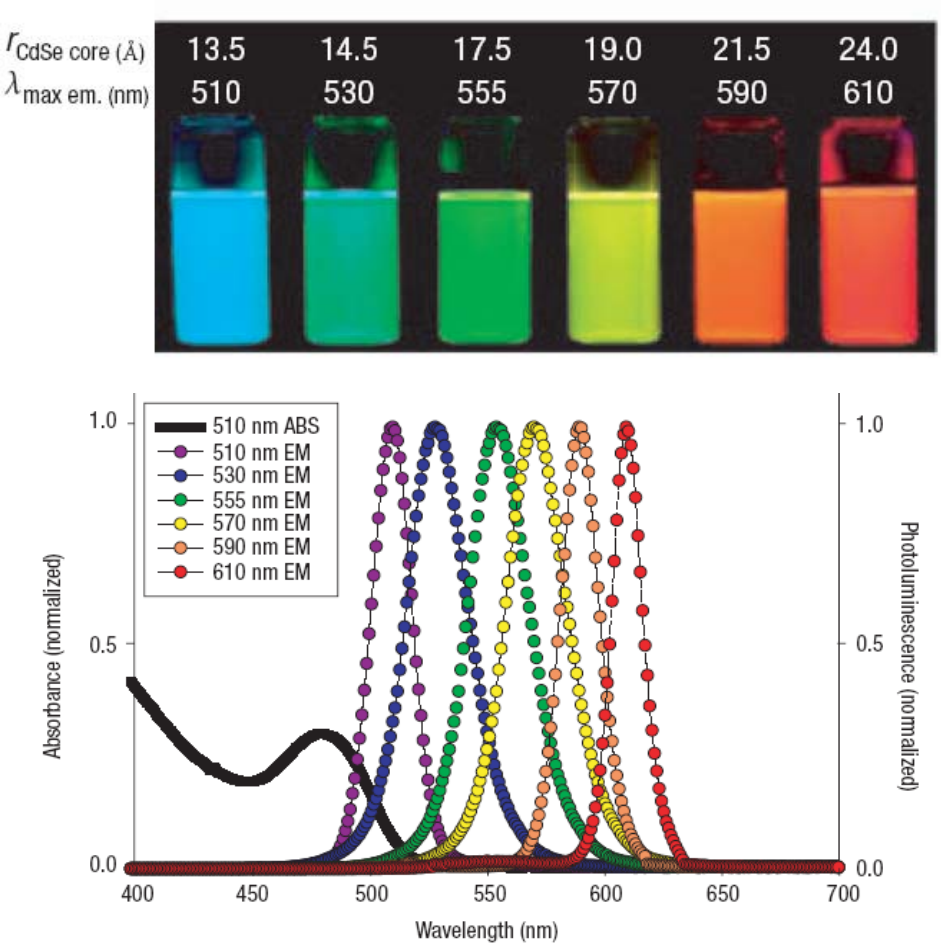

Figure 2.2 Excitation and emission spectra of quantum dots in six different sizes. Photo demonstrating the size-tunable fluorescence properties and spectral range of the six QD dispersions [87].

Another unique optical characteristic of QDs is their fluorescence lifetime of 10 to 40 ns [8, 91], which is significantly longer than typical organic fluorophores. Combined with pulsed laser and time-gated detection, the use of QD labels can produce images with greatly reduced levels of background noise and thus enhance the imaging sensibility. However, QDs suffer a blinking effect, which is, QDs randomly alternate between an emitting state and a non-emitting state. This intermittence in emission of QDs is universally observed from single dots, which imposes some limitations in QD applications. It has also been reported that QD fluorescence intensity increases upon excitation, an event as referred to photobrightening [92], which is problematic in fluorescence quantization studies.

2.3.2 Biocompatible Capping

The core and core-shell QDs are hydrophobic and only soluble in nonpolar solvents. For biology application, the surface of QDs should be hydrophilic. Several strategies have been used

to stabilize core-shell nanocrystals in aqueous solutions (Figure 2.3). The easiest approach is to exchange the hydrophobic surfactant molecules with bi-functional molecules, which are hydrophilic on one side and hydrophobic on the other side [93-95]. The long-term stability of the QDs using these bonds is not strong; therefore, water solubility of core-shell-capped QDs is limited.

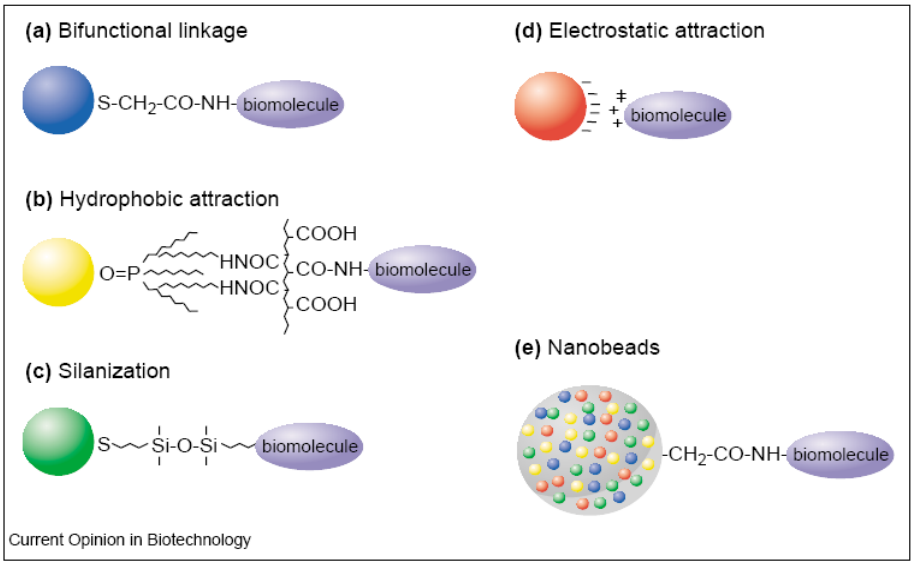

Figure 2.3 Schematic illustrations of five different bioconjugation methods [101].

An alternative approach is to grow a silica shell around the particle, also called surface silanization [92]. The silica shells can be highly cross-linked to QDs and silanized QDs are extremely stable. Recently, other solubilization methods have been reported, one of which involves coating the surface with polymers [96]. Instead of exchanging the hydrophobic surfactant, the particles in this case are coated with a cross-linked amphiphilic polymer. However, the final size of the QDs after polymer coating is rather large. Other approaches, such as coating the QDs with phospholipid micelles [97], dithiothreitol [98], organic dendron [99] have also been reported.

To make QDs for in-vivo applications, QDs should be conjugated to biological molecules without disturbing the biological function of these molecules. Several approaches have been used to link biological molecules to QDs, including adsorption of oligonucleotides [100], electrostatic interaction, and covalent linkage between QDs and biomolecules [87, 92, 98, 101].

2.4 Temperature Dependence of Photoluminescence of Quantum Dots

Since quantum dots are semiconductor materials, a relation for the variation of the band gap energy (Eg) and temperature (T) can be formulated as [102]**:**

$$E_g(T) = E_{g0} - \alpha \frac{T^2}{(T + \Theta)}$$

Equation 2.1

where E_g is band gap energy, E_{g0} is the band gap energy at 0 K, α and Θ are constants. Most of the variation in the band gap energy with temperature is due to the following two mechanisms:

a. A shift in the relative position of the conduction and valence bands due to the temperature-dependent dilatation of the lattice. It has been studied that at high temperatures, the temperature-dependent effect is linear. At low temperature, however, the thermal expansion coefficient is nonlinear with respect to temperature.

b. The second mechanism is due to a temperature-dependent electron lattice interaction.

Several groups have been studying the temperature-dependent optical absorption and luminescence bands of bulk quantum dots [83]. The maximum wavelengths of the fluorescence have been characterized as function of temperature. Valerini has shown that the emission of bulk CdSe quantum dots shift to the lower energy with high temperature, meaning the red spectrum, as shown in Figure 2.4 [82]. Walker demonstrated that the photoluminescence intensity of CdSe/ZnS QDs increases by a factor of 5 when the temperature is decreased from 315 to 100 K, and the peak of the emission band is blue shifted when temperature is reduced by 20 nm over the same range [83]. The change in photoluminescence intensity is linear and reversible for temperatures close to ambient conditions. Furthermore, temperature-dependent linewidths, or full width half maximum (FWHM) of CdSe materials were investigated [103] and similar studies were carried out with ZnSe quantum dots [81, 104]. Labeau has shown that the bulk CdSe lifetime is decreased with respect to increasing temperature, but saturated when temperature is higher than 70 K [105]. Donega has further studied QDs properties in a wider temperature range from 1.3 to 300 K [106]. He found that the lifetime is actually saturated both at low and high temperature, at 4 K and 50-70 K. Figure 2.5 shows the fitted model along with their experimental data. The temperature dependence of the absorption and fluorescence spectra of colloidal CdSe nanocrystals was also studied in different shapes, such as dots, rods, and tetrapods [80]. While the shift of the peak fluorescence wavelengths indicates little dependence on the shape of QDs, the broadening of the emission spectrum behaves differently for dot- and rod-shapes, indicating shape-dependent spectrum broadening mechanisms.

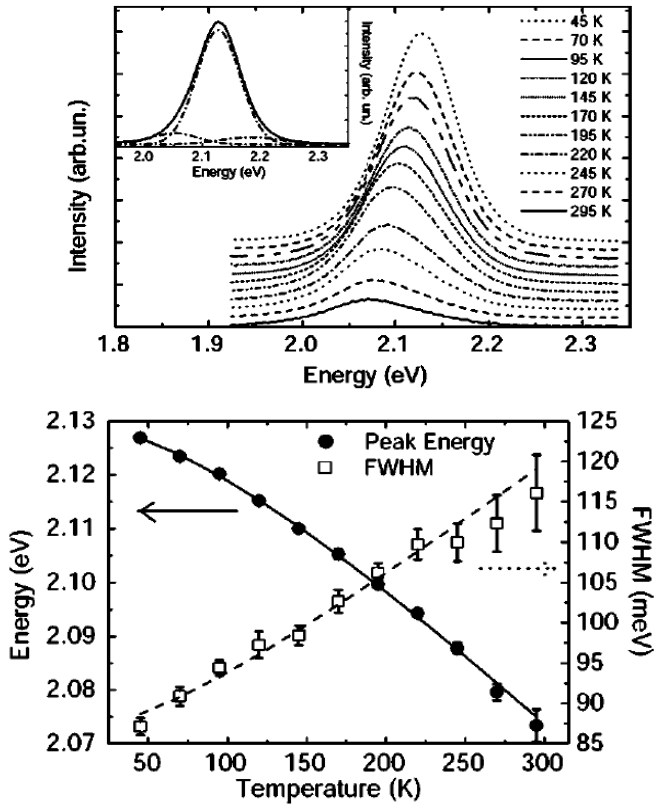

Figure 2.4 Characterization of the emission from bulk CdSe quantum dots [82].

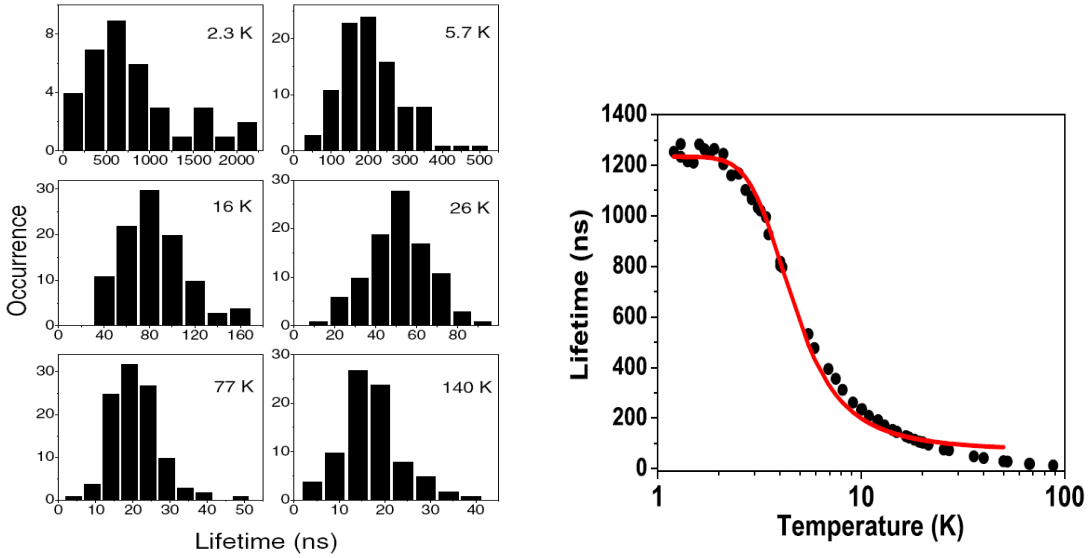

Figure 2.5 Bulk CdSe luminescence lifetime as function of temperature [105,106].

2.5 Characterization of Temperature Dependence of Single Quantum Dots

Although previous reports have studied spectroscopic characteristics of CdSe QDs with respect to temperature, the effectiveness of individual QDs as a temperature marker has not been investigated. In this section, an experimental procedure has been designed to explore if emission spectrum from individual QDs is sensitive to environmental temperature changes.

2.5.1 Experimental Setup

The schematics diagram of the experimental setup is illustrated in Figure 2.6. The sample was mounted on a home built sample holder whose temperature was regulated in the water bath, and the entire sample holder is secured on an inverted microscope (IX-71, Olympus). To maintain the whole system at the same temperature, a temperature regulated collar was mounted on the objective. A thermocouple (5SC-TT-K-36-36; Omega Engineering, Inc.) was taped onto the top of a small glass cover slip next to the observation point to monitor the device temperature. A 532-nm continuous-wave laser (Compass 315M-100; Coherent) was used to excite single QDs through a microscope. The total internal reflection fluorescence (TIRF) objective (100x with a numerical aperture of 1.45) was used to acquire the image and spectrum of individual quantum dots. The emission from each QD was collected by the same objective through a dichroic mirror (560lp; Chroma) to reject the excitation light. The spectrally filtered emission was further dispersed by a spectrograph (SP2150i, Princeton Instruments/Acton-Research, grating 600 g/mm blazed at 500 nm) and imaged by an intensified camera (Cascade 512B; Roper Scientific).

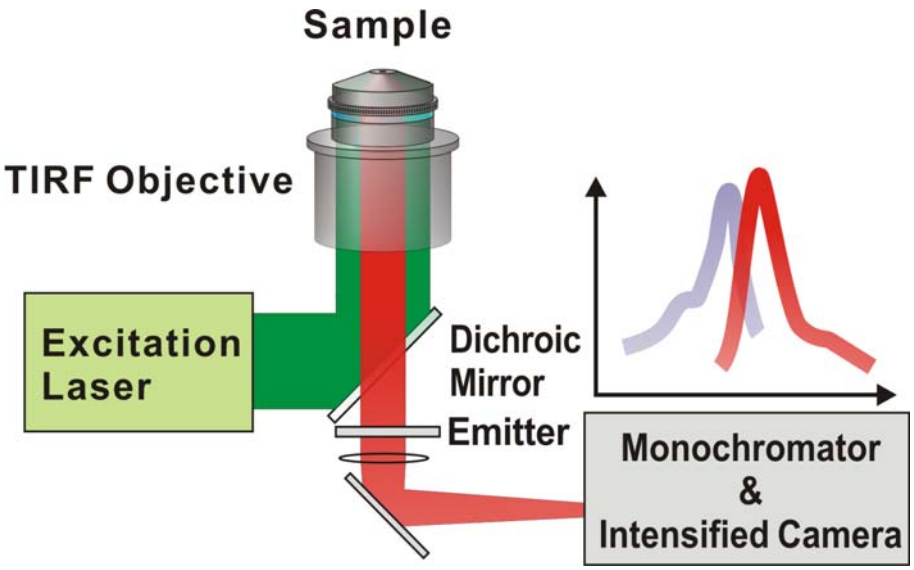

Figure 2.6 Optical setup for temperature measurement via spectra shift of quantum dots.

The entrance slit of the spectrograph, which is placed at the image plane of the microscope, also helps minimizing the influence of other QDs outside the centerline region. The entrance slit was set to 30 μm wide and the central wavelength of the spectrograph was set to 655 nm. The dispersion of the grating at 655 nm is 8.857 nm/mm. The size of the image sensor

of the camera is 8.2×8.2 mm^2, with 512×512 pixels. Thus, the spectra resolution of the experimental setup is 0.14 nm/pixel.

2.5.2 Sample Preparation

The commercially available water-soluble CdSe quantum dots with an emission maximum at ~655 nm (Qdots/Invitrogen) came encapsulated by a ZnS shell, coated with a layer of organic polymer, and conjugated with streptavidin. The stock QDs solution was diluted in phosphate–buffered saline (PBS) to final concentration of ~0.5 pM. The concentration of the QD sample was kept low to optically resolve individual dots. A total 20 µL of this dilution was pipetted and sandwiched between two 24×50 mm^2 glass cover slips. After a period of 10-minute incubation at 100^{o}C in order to dehydrate QD solution, the cover slips were separated. Afterwards, 10 µL of premixed poly-dimethylsiloxane (1:1 mixture of PDMS base and curing agent, Sylgard 184) was added on one cover slip to fix the position of QDs. Afterwards, a 22×22 mm^2 glass cover slip was placed on the sample and sealed by nail polish on the edges. Typically, about 10 single QDs were recorded in a field of view of 80×10 μm^2 in our optical setup. The detail steps are illustrated in Figure 2.7.

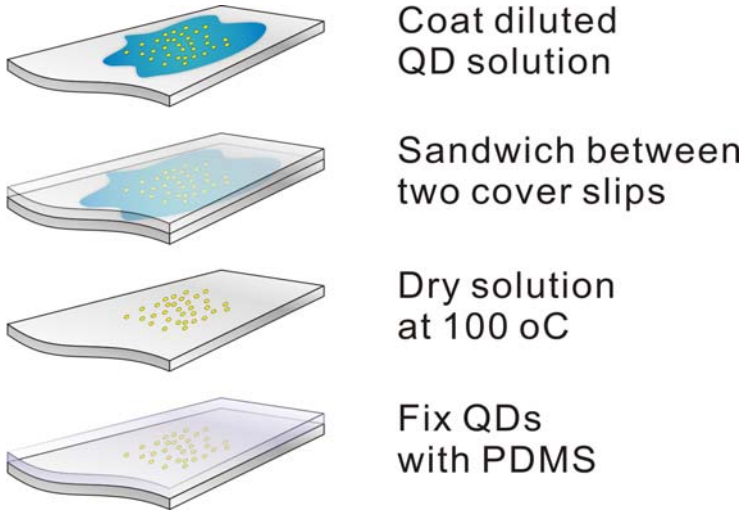

Figure 2.7 Sample preparation for single quantum dots visualization and characterization.

2.5.3 Imaging Acquisition

Initially, the entrance slit of the monochromator was set to wide open to have larger field of view for easier observation. After locating and focusing QDs, the entrance silt was closed down to 10 µm in width. To capture multiple individual QDs simultaneously, the sample stage was gradually moved to have several QDs fell inside the observation field. The images were collected via WinView32 (Roper Scientific). Figure 2.8 shows the fluorescence image of seven QDs lined up at the entrance slit of the spectrograph, where bright spots are the single QDs, as indicated in arrow heads. To capture the emission spectra of individual QDs, the wavelength of monochromator was set to 655 nm to separate the spectrum of each single quantum dot inside the observation field into vertical lines as shown in Figure 2.8. The center of the image in the y axis indicates the set wavelength 655 nm in monochromator and the total span with this grating is 72 nm from 619 to 691 nm as marked in Figure 2.8. The intensity of each pixel along the bright

line corresponds to the relative intensity of the spectrum at that particular wavelength indicated in the y axis.

When individual quantum dots are observed using a fluorescence microscope, they emit fluorescence intermittently, causing a blinking effect. Figure 2.9 shows the time lapse of raw spectra of individual QDs at the same observation field. Because of the fluorescence intermittency, different QDs were emitting fluorescence between images. To eliminate the blinking effects and to characterize the spectral information of individual QDs, we captured multiple frames with long exposure time to solve the blinking problems. In each sample, 100 frames were acquired with a 2-second/frame exposure time at each regulated temperature. Before recording the emission spectra, the temperature of the sample holder and the QDs sample was regulated and stabilized by circulated water with controlled temperature. The temperature reading from the thermocouple attached at the cover slip was recorded as the reference temperature. Generally, the position and focus of the QDs could shift due to thermal expansion effects. The stage was adjusted each time after heating so that every single quantum dot was at its original coordinates.

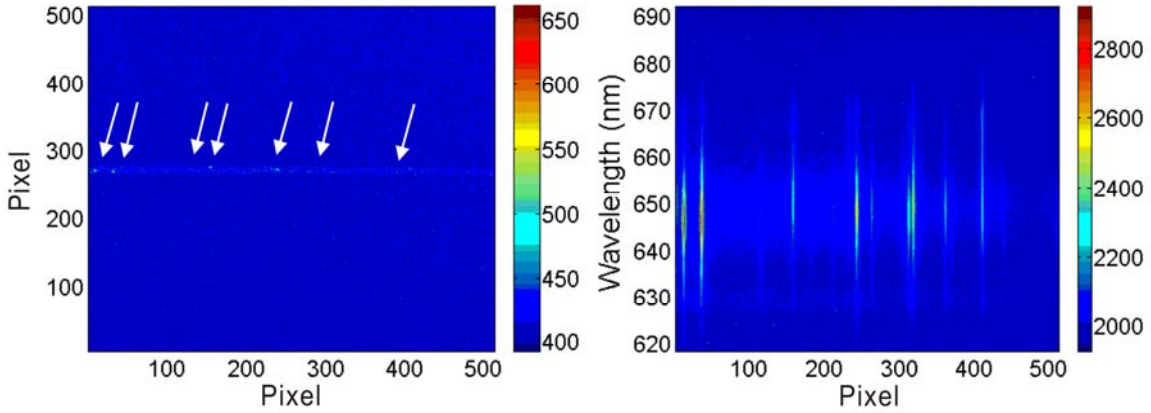

Figure 2.8 Examples of QDs luminescence in wild field image and their emission spectrum. Since QDs are blinking, each frame may have different QD emission. In the left panel, 7 single QDs were counted and indicated at arrow heads.

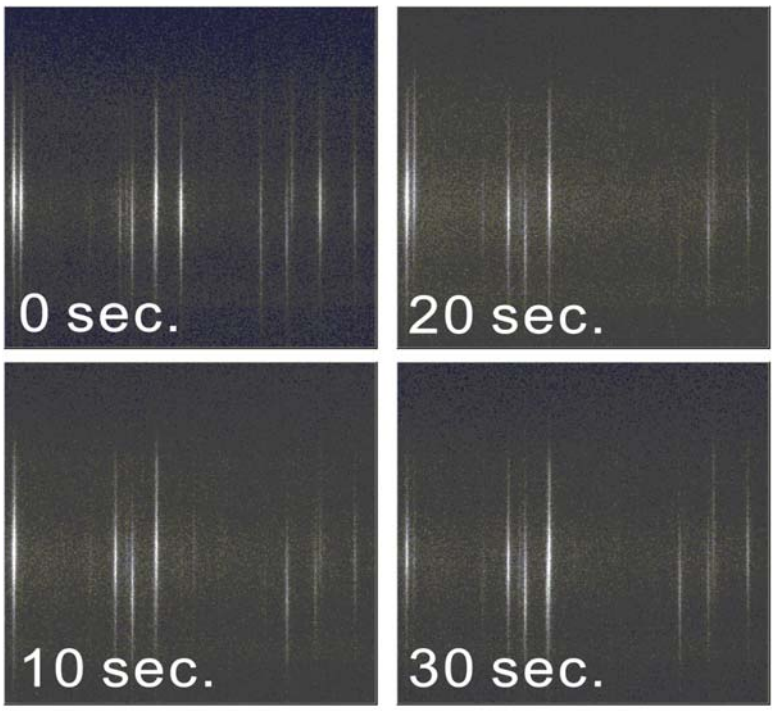

Figure 2.9 Time lapse fluorescent images in spectral mode showing blink effect of single QDs.

2.5.4 Data Analysis

All raw images were analyzed by MATLAB (Mathworks, Natick, MA) and 100 frames of data were collected into one image with several spectra information from different QDs. First, the positions of spectra signals in each frame were flagged and spectra from same position in different frames were averaged to get the final spectra information. The measured emission spectrum from single QD can be plotted as the function of wavelength in x axis and emission intensity in y axis, as shown in Figure 2.10b. To obtain the wavelength of peak emission, a first-order Gaussian curve, as shown in Equation 2.2, was used to fit the peak region of intensity-wavelength profile of the raw data.

$$I = A * \mathrm{Exp}\left(\frac{-(x-x_0)^2}{2*\sigma^2}\right)$$

Equation. 2.2

where I is the emission intensity, A is the amplitude fitting parameter, x_0 is the peak wavelength, and σ is the peak width.

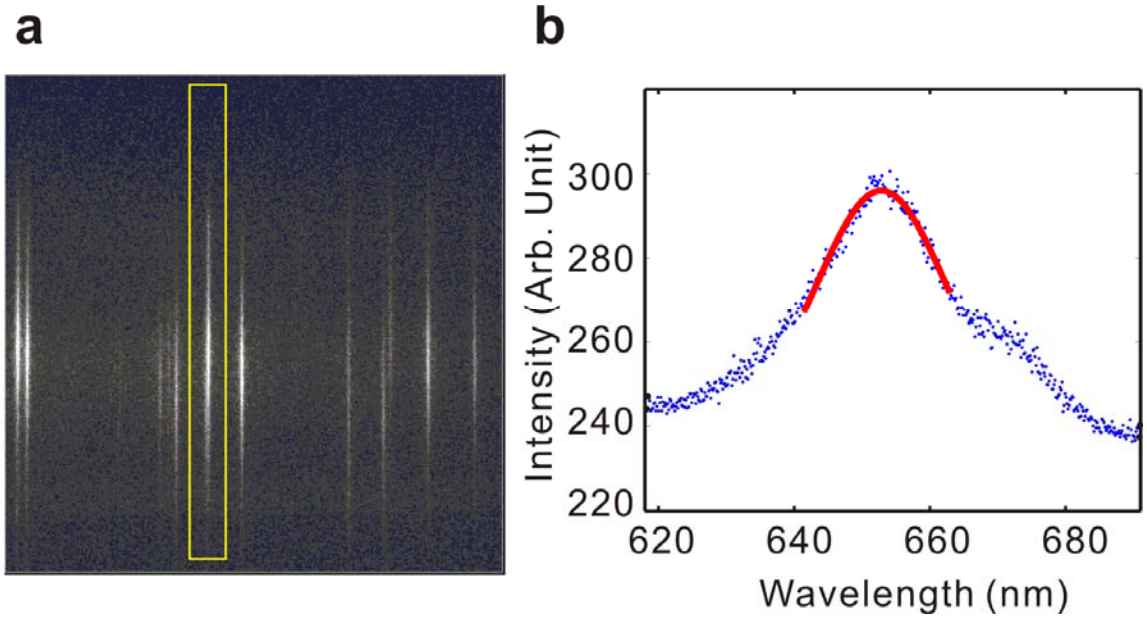

Figure 2.10 a. Raw image of emission spectra of QDs. **b**. The measured spectrum (blue dots) and its Gaussian fitted curve (red solid line).

2.5.5 Results

The distributions of peak wavelength of individual QDs were characterized and small variations were observed probably due to small size and shape differences of as-synthesized QDs. For example, Figure 2.11 shows the distribution of emission peak wavelength of quantum dots at 35°C, with sample population of 328 single QDs. The standard deviation of the peak wavelength is about 0.7 nm.

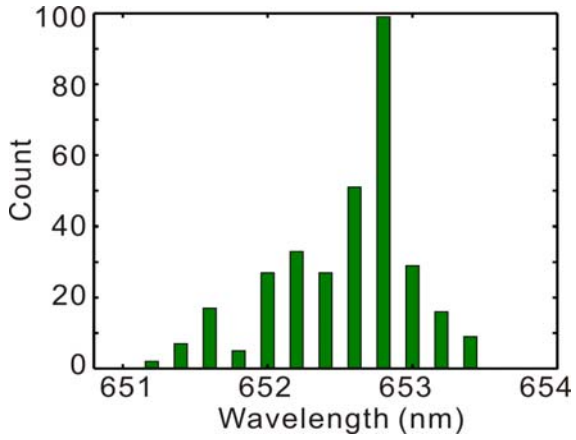

Figure 2.11 Histogram of peak wavelength of individual QDs.

Next, the temperature effects of individual QDs were investigated. Figure 2.12 displays representative emission spectra of a single QD when the substrate temperature was increased from 24.4 to 43.6°C. The raw spectra and Gaussian fits are shown as dots and solid lines, respectively. Using this QD as an example, it is observed that the peak wavelength of a single QD exhibits a red shift to longer wavelengths as the temperature increases. Furthermore, the wavelength shift can be approximated as a linear function of temperature in this temperature range with sensitivity about 0.1 nm per degree Celsius. This number is consistent with previous bulk measurements which gave an expected ~0.093 nm/°C dependence at this temperature range [103]. Temperature-dependent shift in the wavelength has been explained theoretically in terms of temperature-dependent dilatation of the lattice and electron-lattice interaction [102]. Furthermore, it is found that the emission intensity at peak wavelength decreases linearly with respect to temperature and the full width half maximum (FWHM) has a linear relationship with temperature and broadens at higher temperature. Emission intensity and spectral width as function of temperature are plotted in Figure 2.13a and 2.13b, respectively. The statistical significance of the observation is examined by repeating the same experiment over 71 single quantum dots. To evaluate the uncertainties of a mean value, the error bar was calculated as $\Delta\lambda / \sqrt{N}$, where $\Delta\lambda$ is the standard deviation of the wavelength and N is the number of data points, which is 71. The results are displayed in Figure 2.14, which shows that on average the peak wavelength of emission spectra changes with temperature.

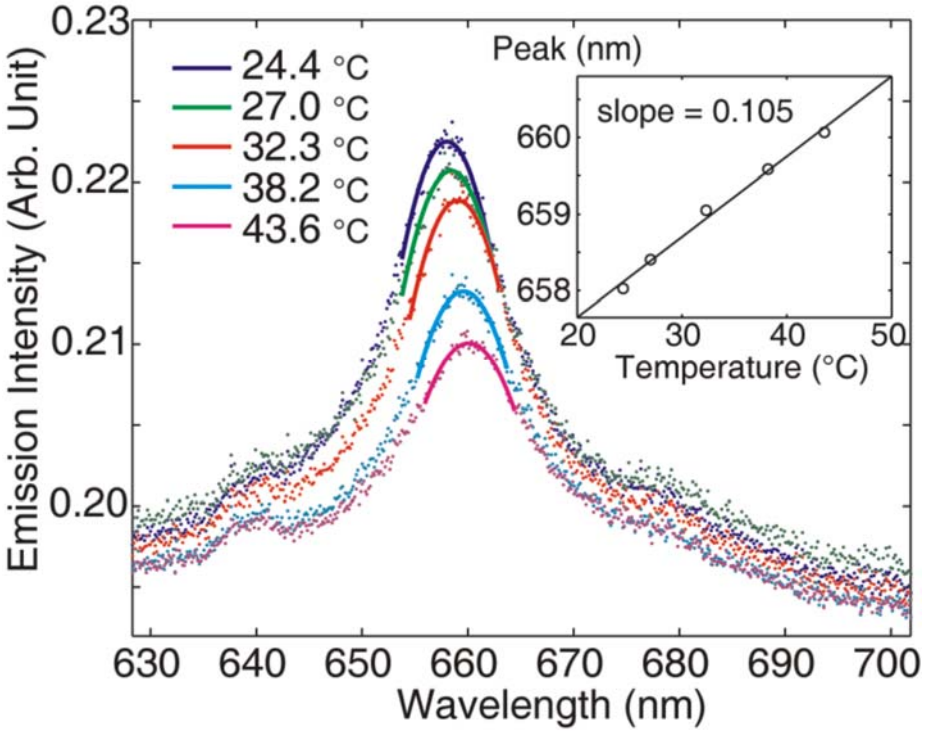

Figure 2.12 Temperature-dependent spectral shifts of a single QD from 24.4 to 43.6°C. The raw spectra and Gaussian fits are shown as dots and solid lines, respectively. Insert: Wavelength shift is a linear function of temperature in this temperature range.

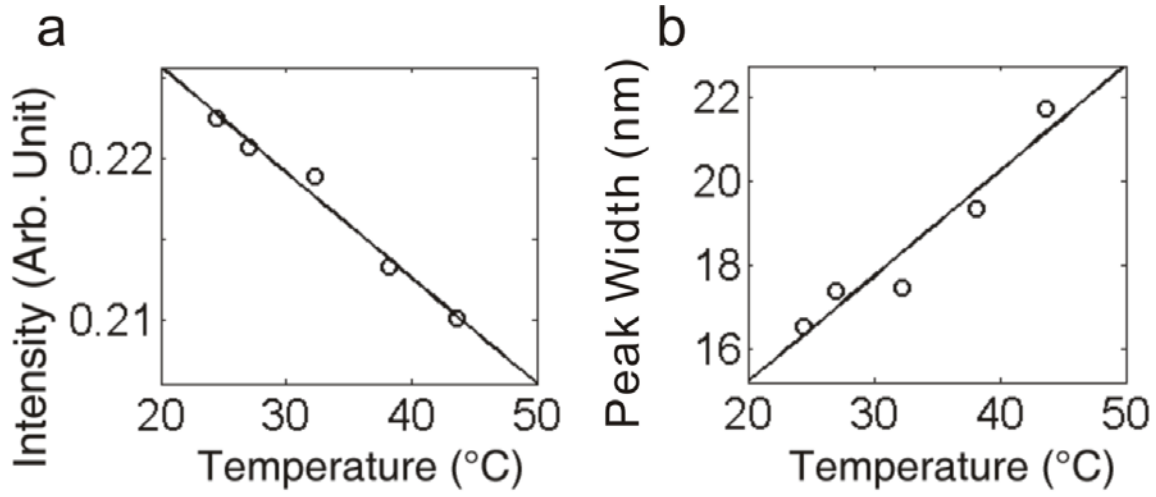

Figure 2.13 a. Plot of the emission intensity as a function of temperature. **b.** Spectral width as a function of temperature.

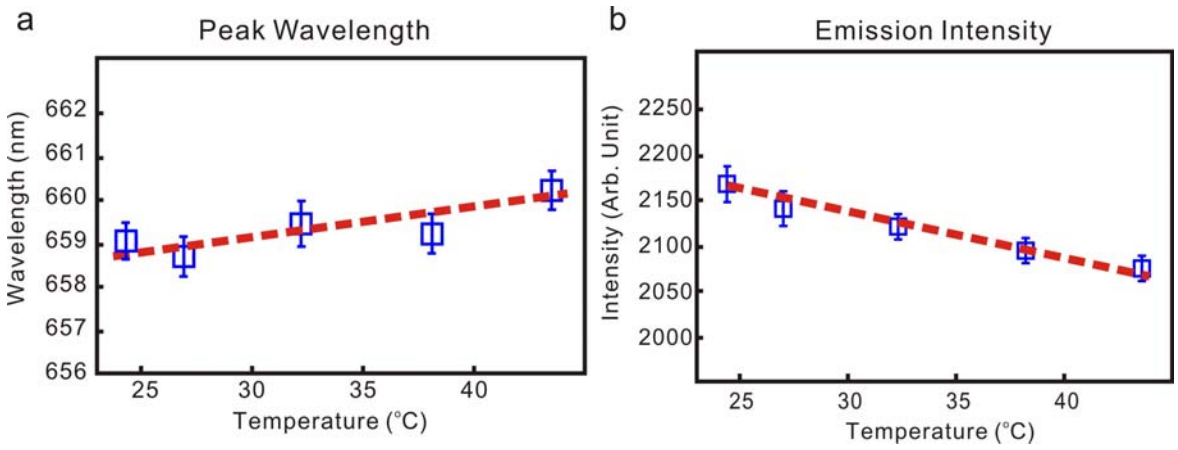

Figure 2.14 Average peak wavelength and emission intensity of QDs under different temperature.

2.5.6 Discussion

Since the CdSe Quantum dots are semiconductor nanocrystalline particles, the temperature dependence of emission spectra can be considered as the variation of band gap energy of the material with respect to temperature. The relation of band gap energy and temperature in semiconductors was discussed in Eq (2.1), where Θ can be approximated as the Debye temperature of the material. The measured temperature-dependent characterization from single QDs was fitted to this relationship and corresponding parameters were derived in Table 2.1 and compared with bulk material and observations made by other research groups.

	E_{g0} (eV)	α (meV/K)
Single QD	*1.951*	*0.336*
Bulk [83]	*1.757*	*0.37*
Valerini [82]	*2.13*	*0.32*

Table 2.1 Fitting parameters for equation 2.3.

The average emission intensity and the spectral width were found to decrease and broaden at higher temperatures (Figure 2.13a and 2.13b). One explanation for the decrease in intensity can be attributed to the Maxwell distribution of the exciton kinetic energies, where the intensity is proportional to the exponential of $(1/kT)$ - k is Boltzmann constant and T is temperature in Kelvin. The broadening of the "full width half maximum" can be attributed to escalated interaction between exciton and longitudinal optical phonon in the CdSe core at elevated temperatures, resulting in enhanced non-radiative decay [80, 82]. The other observation is the variations in peak emission wavelength varied from dot to dot probably due to small variations in the size and shape of QDs [89, 106]. This fact implies that it could be challenging to measure "absolute temperatures" based on results of peak wavelength of a single QD as it has to be individually calibrated. However, it could be possible to use the average peak wavelength of a group of QDs as the foundation for absolute temperature measurements. This consideration motivated us to evaluate the required minimum number of particles to give a reliable temperature reading. To address this question, we first performed the bootstrap statistical analysis [107] on single QD data to investigate the minimum number of particles needed for them to converge to the bulk results. The bootstrap algorithm can be summarized as the following steps:

a. Draw 'N' number of samples from the database.
b. Take mean of these N samples. Compute the relative deviation with respect to the whole sample mean.
c. Repeat steps a and b (25*sampling size/N) times. Calculate mean of these relative deviation.
d. Repeat steps a-c 10 times. Each time save the relative deviation.
e. Calculate the mean and standard deviation of the relative deviation of these in step d.
f. Increase drawing sample size N until reaching the maximum. Maximum N is equal to half of the whole sample size.

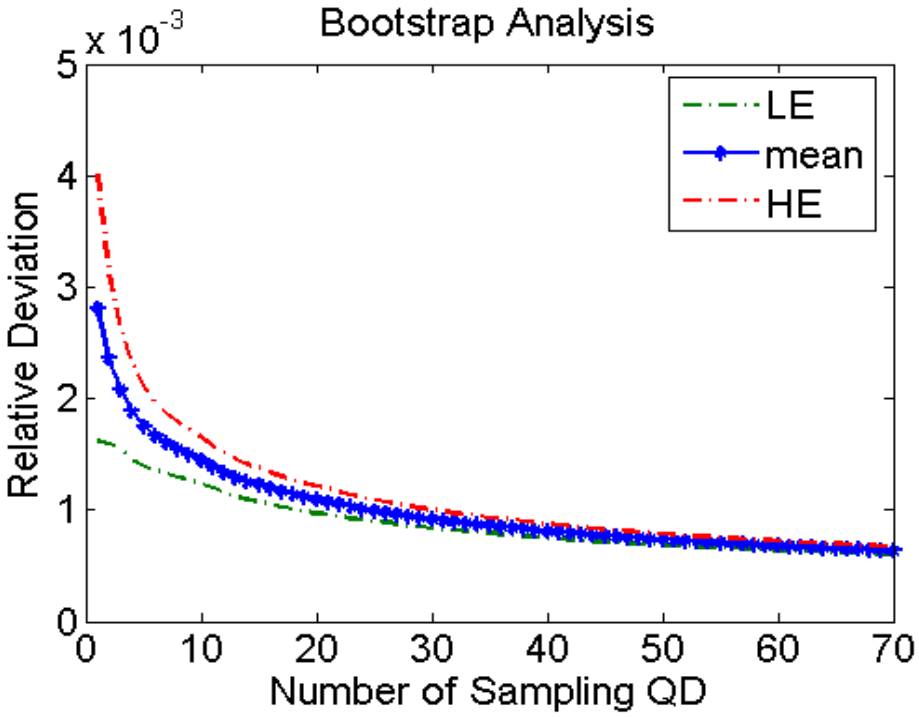

Figure 2.15 Bootstrap analysis on relative deviation of the quantum dots emission peaks.

The bootstrap analysis is presented in Figure 2.15, where blue solid line is the mean of the relative deviation computed in "step e," and green and red dashed lines are the low and high estimates. We found that the relative deviation of the averaged spectral mean scales as $N^{-1/2}$, where N is the number of particles being considered: $\left|\langle\lambda\rangle_N - \langle\lambda\rangle_{\text{ensemble}}\right| / \langle\lambda\rangle_{\text{ensemble}} \approx A/\sqrt{N}$, where $A = 5.28\times10^{-3}$ at room temperature (22°C). Using this empirical relation and the ~0.1 nm/°C temperature-dependent spectral shift, one can estimate the number of particles needed to achieve a certain precision in the optical temperature readouts. For example, it will take about 1200 particles to make a temperature measurement with 1°C in precision. Assuming that the particle diameter is about 10 nm, we estimate that it will require ~174 nm in diameter to accommodate 1200 particles.

2.5.7 Conclusion and Summary

This experiment demonstrates that individual QDs are capable of sensing temperature variations and reporting temperature changes remotely through optical readouts. Furthermore, empirical relations and statistical analyses conclude that about 1200 particles are needed to achieve 1°C precision in optical temperature readout statistically and the spectral shift of a single quantum dot was characterized as 0.1 nm/°C around room temperature.

2.6 Proof-of-Concept Demonstration

To further demonstrate the capability of using QDs as temperature marker through noncontact, optical measurements, we implement this idea to a MEMS application where the

remote sensing of local temperature with good spatial resolution is very challenging. To create a temperature gradient at micro-scale, MEMS line heater has been chosen since its temperature is controllable via input power and there are analytical models to predict the temperature distributions.

2.6.1 Heater Design and Fabrication

Aluminum line heaters have been used with dimension of 1200 μm in length and 40 μm in width. The fabrication process of the aluminum line heaters is shown in Figure 2.16. The heaters are fabricated on a 4-inch Pyrex 7740 wafer. Wafer was first cleaned in piranha at 120°C for 10 minutes and dried in spin/rinse dryer. After 10 min dehydration in 120°C oven, the wafer was coated with HMDS in vacuum at 90°C by Primeoven. A 2 μm G-line photoresist (OCG 825) was coated on the wafer at 2200 rpm and soft-baked 120 seconds at 90°C by a SVG 8626 photoresist coat track. The wafer was exposed by Karl Suss MA6 mask aligner using hard contact. The exposure dose was 146.9 mJ/cm^2 (UV intensity = 23.7 mW/cm^2, exposure time = 6.2 s). After the exposure, the wafer was developed in OCG 934 2:1 developer for 30s by the SVG photoresist develop track and baked in 120°C for 90 seconds. Afterwards, the wafer was hard backed in the 120°C oven for 1 hour and transferred into a Veeco 401 Vacuum system to thermally evaporate 500 nm-thick Aluminum. A crystal monitor was used in Veeco 401 to inspect the film thickness. The current used to evaporate the aluminum shots is 90~120 A and the deposition rate is controlled at around 6 Å/s. After evaporation, the wafer was put into an ultrasonic acetone bath to lift off the photoresist film for 1 hour. A clean-room swab was used to wipe the surface gently to get rid of any residues left on the wafer and the wafer was cleaned in acetone and DI water. A 2 μm-thick photoresist layer for dicing protection was coated by SVG coat track and Disco dicing saw was used to dice the wafer into chips. Finally, the diced chips were clean in acetone bath to remove the photoresist protection layer. Gauge 30 wires were used in a conductive epoxy bonding (ITW Chemtronics) process onto 1.5 mm in-diameter circular contact pads.

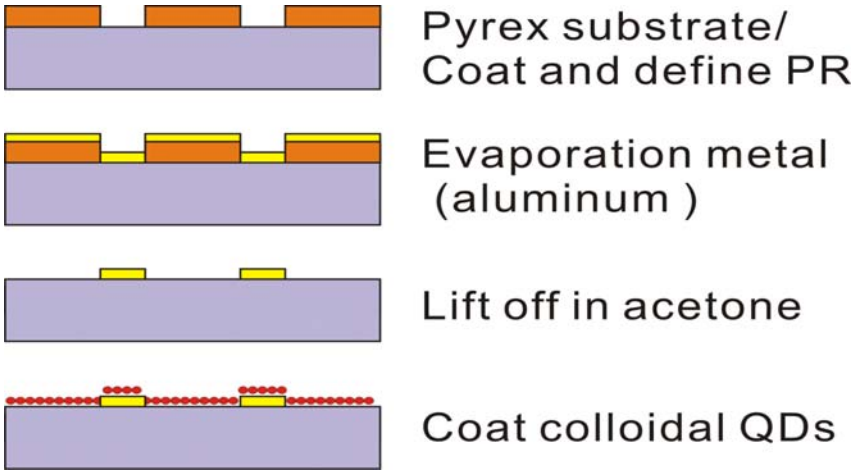

Figure 2.16 Fabrication process of the micro-heater.

2.6.2 Experimental Setup

The detection system setup is similar to that used in the single QDs spectra measurements. The micro-heater was directly secured on the microscope stage, and a 60x objective with a numerical aperture of 1.45 was used to collect the spectra. A grating of 1200 g/mm blazed at 500 nm was used in the spectrograph (SP2150i, Princeton Instruments/Acton) for resolving the QDs emission spectra and an intensified camera (Cascade 512B, Roper Scientific) was used to record the spectra image. The entrance slit of the spectrograph was set to 30 μm-wide for spectra imaging.

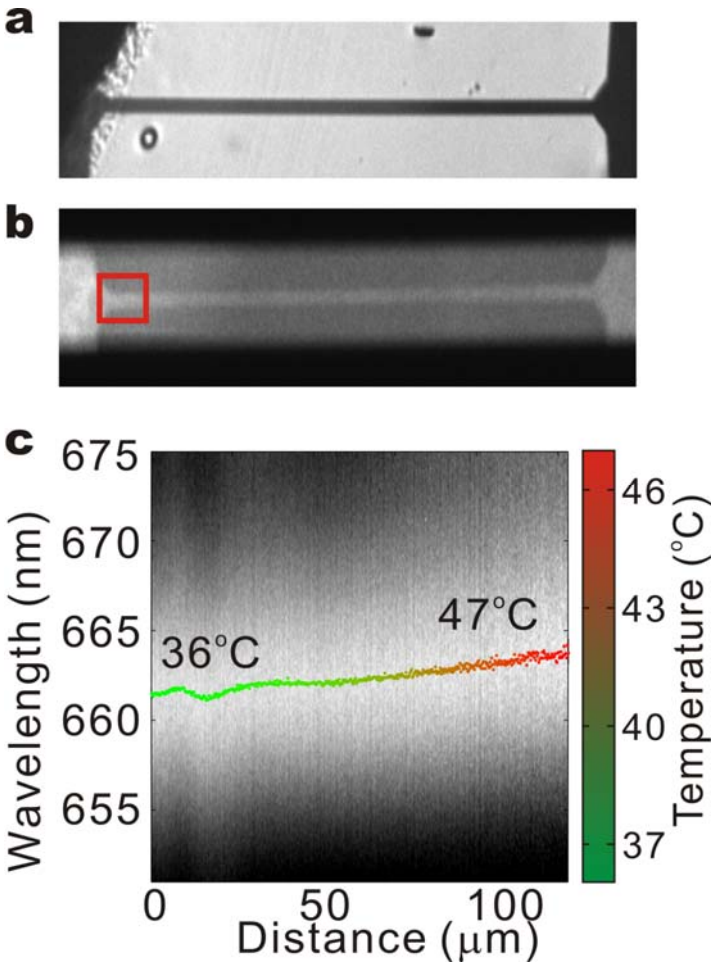

Figure 2.17 a. Wide-field image of a fabricated aluminum micro-heater. **b.** Fluorescent image of the micro-heater coated with CdSe QDs. **c.** QD spectrum-position image of the red rectangle indicated in **b**. Pseudocolor indicates the temperature differences.

Prior to the experiments, 3 μL of 200 pM CdSe QDs solution was applied to the heater chip and dried in air for 30 minutes. Figure 2.17a and 2.17b show respectively the bright field image and the fluorescent image of the micro-heater coated with CdSe QDs under low magnification. Two leads of the micro-heater were connected to a DC power supply (E3612A,

Hewlett-Packard). The temperature of the micro-heater was adjusted by applying different voltages, from 1 to 5 V. For each set of spectral recording, 10 frames of spectral image were acquired with 1 second/frame exposure time. The spectral data were collected after the heater reached steady state. The experimentally measured temperature profile was obtained based on the calibration results from the aforementioned single QD experiment.

2.6.3 Experimental Results

For the non-contact temperature measurement, a 60x air objective was used. When projected on the camera (512×512 pixels), each spectrum-position image corresponded to 136 μm in length along the heater. Therefore, each pixel along the abscissa (along the heater) in the spectral image corresponded to a physical width of ~267 nm on the heater. The entrance slit of the spectrograph placed at the image plane of the microscope was set to 30 μm wide, corresponding to a 500 nm-wide strip along the axis perpendicular to the heater length direction. Therefore, each spectrum relatively corresponds to 500×267 nm^2 area at the sample. The QD emission from each area was spectrally resolved by the spectrograph so that the peak emission of the spectrum reports the local temperature. The peak emission was calculated by Gaussian fit as described in previous section. A representative QDs spectra-position image is shown in Figure 2.17c. The dots indicate the peak wavelengths of the spectra from a Gaussian fit and are color coded to reflect the corresponding temperatures.

Each image covered only 136 μm of micro-heater length. Experimentally, 12 images were required to cover the entire 1.2 mm-long heater and the overlapping portions between consecutive images were averaged in the data analysis. The relative wavelength shift with respect to initial recording at room temperature was used to compute the temperature changes after applying power to the micro-heater. Figure 2.18a shows the raw data of the temperature profile along the aluminum micro-heater after combining the spectrum-position images. To remove the low-frequency interference pattern (at ~0.03 μm^{-1} due to the excitation laser), a band-pass Fourier filter was coded in Matlab and was used to filter the raw data. We were able to reconstruct the temperature profile along the aluminum heater under different input voltage, as shown in Figure 2.18b. With higher input voltage, it is clear to see that the temperature is higher.

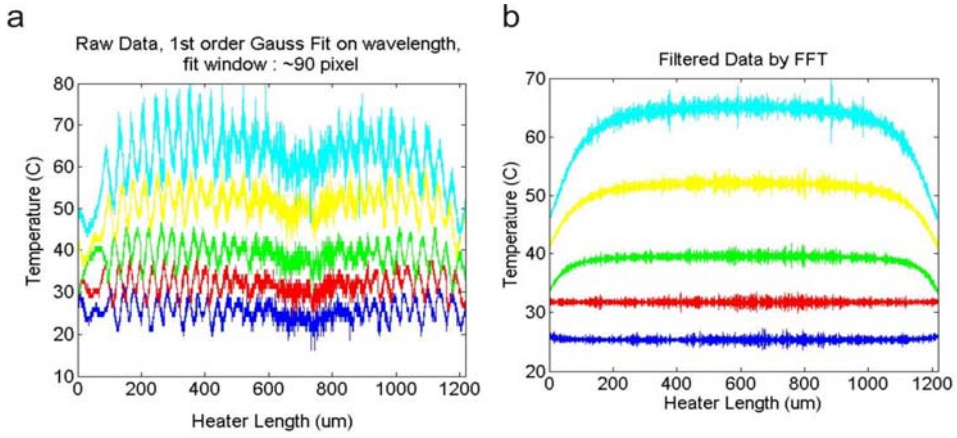

Figure 2.18 a. Raw data of the temperature profile along the aluminum micro-heater after combining images. **b.** Temperature profile along the aluminum micro-heater after a band-pass Fourier filter calculation.

2.6.4 Analytical Model

Analytically, temperature characteristics of the micro-heater are determined by various parameters such as current density, geometry, and thermal properties including temperature coefficient of the resistivity. The lumped one-dimensional eletrothermal model has been derived by the law of energy conservation as a second-order partial differential heat equation[108]

$$\frac{\partial^2 T}{\partial x^2} = \frac{1}{\alpha_p}\frac{\partial T}{\partial t} + \varepsilon(T - T_{ref}) \qquad \text{Equation 2.3}$$

where T is the temperature along the micro-heater, t is time, and α_p is the thermal diffusivity of substrate. Both ε and T_{ref} are functions of resistor dimensions and thermal properties, and can be formulated as

$$\alpha = \frac{k}{c\,d} \qquad \text{Equation 2.4}$$

$$\varepsilon = \frac{F}{z^2} - \frac{J^2 \rho\, \xi}{k} \qquad \text{Equation 2.5}$$

$$T_{ref} = T_\infty + \frac{J^2 \rho}{k\,\varepsilon} \qquad \text{Equation 2.6}$$

where k is thermal conductivity [$Wm^{-1}K^{-1}$] of the substrate, c is specific heat [$Wm^{-1}K^{-1}$], d is density [kg m^{-3}], z is the thickness [m] of the substrate, ρ is resistivity [ohm-cm], ξ is resistivity coefficient with respect to temperature [K^{-1}], and F is an excessive shape factor, which is used to account for the heat conduction loss to the substrate and environment. The steady-state solution can be derived as

$$T(x)_{ss} = T_{ref} - \frac{(T_{ref} - T_\infty)\left(\cosh\left[\sqrt{\varepsilon}\left(x - \frac{L}{2}\right)\right]\right)}{\cosh\left[\frac{\sqrt{\varepsilon} L}{2}\right]} \qquad \text{Equation 2.7}$$

The steady-state temperature profile of micro-heater can be approximated by this model, assuming the two big contact pads remain at ambient temperature during experiments. The shape factor can be estimated by a finite element simulation of a transverse cross section of the aluminum heater with heat lost to the substrate and air, and was set to 5. All other parameters are based on the geometry and material of the aluminum heater. The calculated temperature profiles across the micro-heater under different applied voltages are plotted (dash lines) in Figure 2.19, along with the QDs temperature profile extracted from the spectrum measurements (solid lines). It is observed that the two independent methods predict similar temperature results qualitatively and quantitatively, in all five different input powers. A discrepancy comes at the two ends of micro-heater where QDs measurements indicate temperature higher than the ambient temperature. As the contact pads at the ends of micro-heater could heat up and the QDs measurements might reveal these temperature increases.

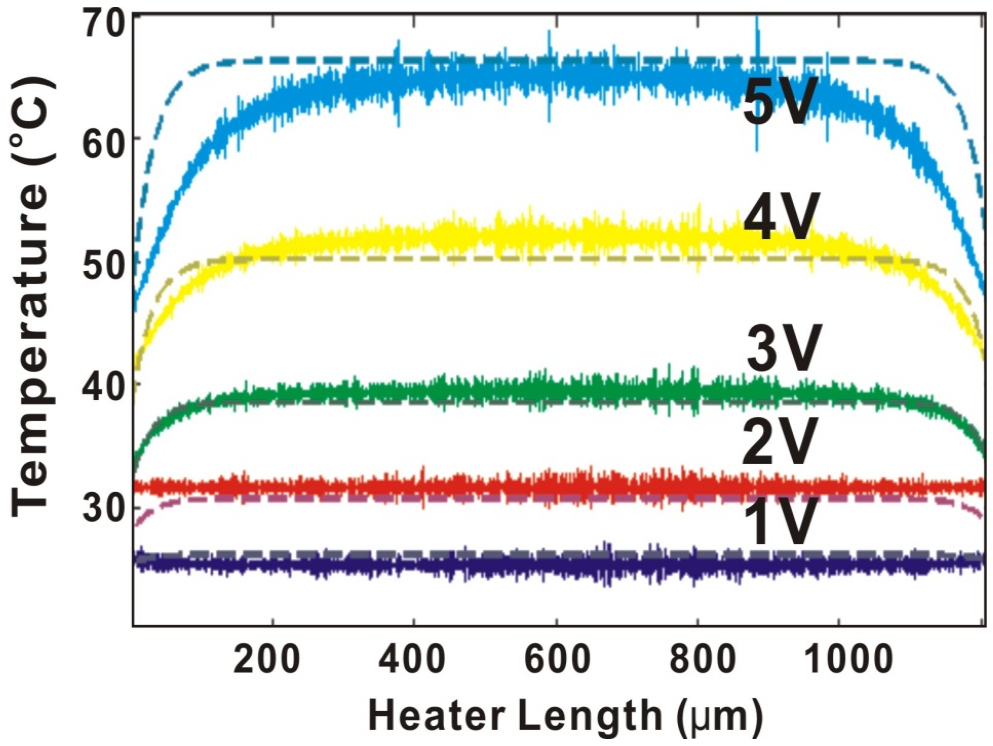

Figure 2.19 Measured temperature profile along the aluminum heater under different input voltage shown in solid lines. Calculated temperature profiles based on Equation 2.8 shown in dash lines.

2.6.5 Conclusion and Summary

The temperature profiles of a micro-heater were reconstructed using spectral shift of QDs. Both experimental and simulation results show good consistency with a 267-nm spatial resolution that is limited by the optical setup. As such, this technique has the potential to be applied to noncontact micro/nano temperature measurements.

2.7 Summary

Temperature measurement with nanoscale spatial resolution remains a challenging issue in nanoscale researches. In this chapter, temperature measurement techniques in micro- and nano-scale were reviewed and the corresponding advantages and disadvantages were discussed. The semiconductor nanocrystalline particles, or quantum dots, were introduced. A short review on the quantum dots synthesis, optical properties, and biocompatibility has been briefed and temperature-dependent optical properties of QDs have been discussed. Furthermore, the possibility of using single quantum dots for temperature sensing has been investigated experimentally. The spectral shift of a single quantum dot was successfully characterized as 0.1 nm/°C around the room-temperature. Furthermore, empirical relations and statistical analyses conclude that about 1200 QDs are needed to achieve 1°C precision in optical temperature readout. As a proof-of-concept experiment, a MEMS heater has been fabricated

with QDs on top for temperature measurements using spectral shift of QDs. Both experimental and simulation results show good consistency with a 267-nm spatial resolution which is limited by the current optical setup. As such, this technique has the potential to be applied for noncontact micro/nano temperature measurements.

Chapter 3
Characterizations of QDs in Single Living Cells

3.1 Introduction

The fluctuations of environmental conditions affect activities of living cells which can have broad implications in energy generation/conversion and health-related metabolism processes beyond the basic molecular cell biology. The influences of these perturbations must be analyzed quantitatively in order to characterize the fundamental heat generation and regulation mechanisms in living bodies, especially at the single cells level. Several attempts have been made to probe the cellular temperature, yet with limited success. Micro-thermocouple has been proposed to probe the cellular temperature [109], but their spatial resolution is usually poor due to large tip sizes (Figure 3.1).

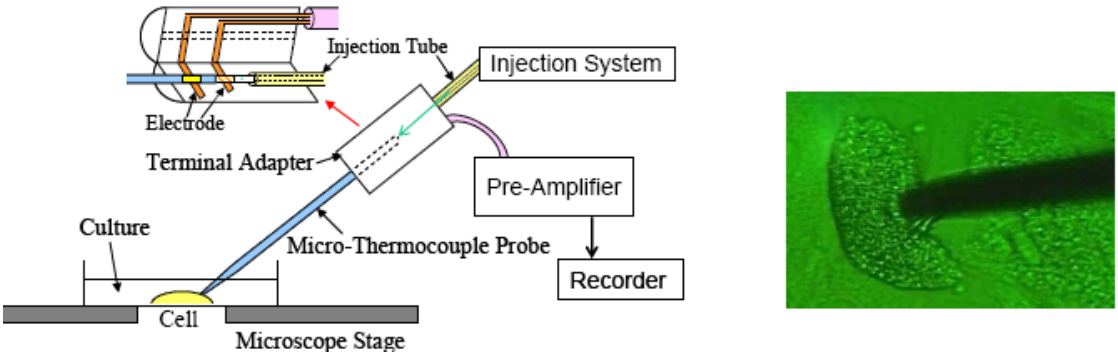

Figure 3.1 Micro-thermocouple probe for measurement of cellular thermal responses [109].

Several dye-based temperature sensing methods have been reported [110-112] for probing biological samples. For example, the phosphorescence intensity of thermo-sensitive dye, Europium(III) thenoyltrifluoroacetonate (Eu-TTA) [110], decreases as a function of elevating temperature as a result of increased fluctuation-induced, non-radiative decay rate as illustrated in Figure 3.2 for surface temperature characterizations [113, 114]. It has been used to image thermal activation of single actomyosin motors [115]. For cellular applications, Eu-TTA has been used to measure the receptor-activated heat production in Chinese hamster ovary cells (Figure 3.3) [43], and the time-dependent response of thermogenesis in HeLa cells induced by ionomycin [23]. In general, however, the dye-based temperature sensing methodology exhibits shortcomings that may limit their application to cellular studies. Emission intensity-based sensing is generally difficult to calibrate because of the many non-specific quenching that can occur inside a cell such as membrane fluidity [45]. Dyes are prone to photo-bleaching, complicating the intensity-based temperature readout and severely curtailing the duration of observation. However, in many cellular studies, prolonged monitoring (tens of minutes) are necessary. The spectroscopic characteristics of dyes are also susceptible to changes by pH [43]. Nevertheless, these studies illustrate the possibility of measuring intracellular temperature with

intriguing results. For instance, experiments by Suzuki *et al*., underestimated the real temperature but they still reported measurable increase as high as 1°C in HeLa cells [23].

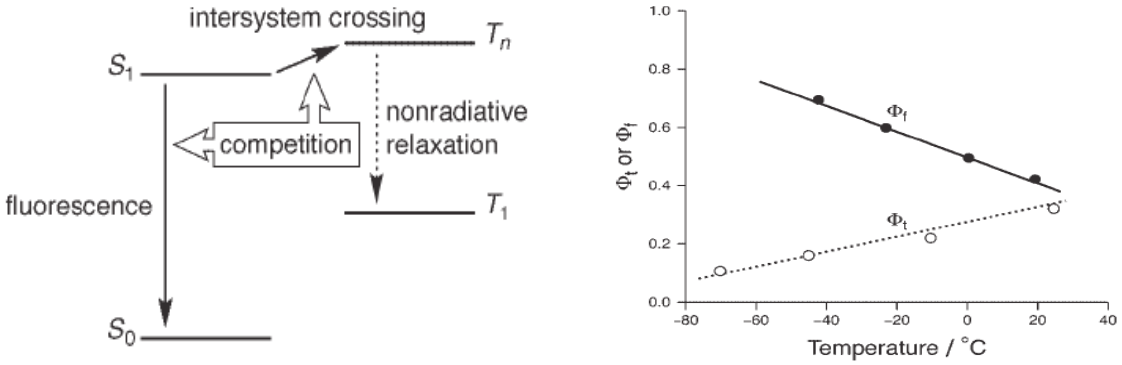

Figure 3.2 (left) Excitation of the TTA ligand is transferred via its triplet electronic level, which fluoresces in a narrow band. **(right)** At room temperature, the quantum efficiency of Eu-TTA phosphorescence declines rapidly with increasing temperatures because of competition with nonradiative processes and coupling between the electronic energy levels and the environment [111].

To accommodate the temperature measurement within the single cells, we proposed the usage of quantum dots (QDs) as temperature indicators in live samples. In chapter 2, it has been shown that QD intensity, emission spectrum, and excited-state lifetime are all strong functions of temperature and therefore can be used to sense temperature [80, 82, 83, 103]. This provides an illustrious fashion for recording temperature based on non-contact, far field optical readout, which is widely used in biology communities. This potential technique has the advantages of diffraction limited spatial resolution and sampling rate limited temporal resolution. Additional advantages over dye-based techniques include drastically improved photo-stability and less sensitive to pH changes. Furthermore, several reports have shown that the internalization of quantum dots with bio-compatible coating and/or with micelle encapsulation can be realized by passive endocytosis into cytoplasm [10, 116]. QDs with antibodies and specific subcellular compartments with signal peptides have been delivered into cells and selectively targeted to specific organelles [9, 21]. Therefore, bringing together advances in nanotechnology, biology, and microscopy, the thermal mapping of the living cells could be achieved.

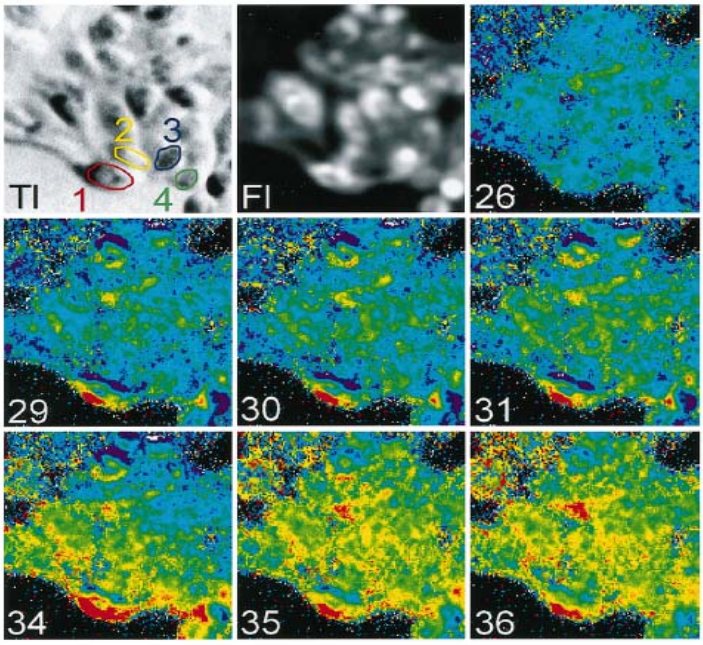

Figure 3.3 Thermal imaging of the heat wave evoked in a cluster of -EuTTA cells after a puff of ACh. The pseudo-color images are color-coded from blue through green and yellow to red (blue represents the highest gray level, i.e., colder areas, and red represents the lowest grey level, i.e., warmer areas) [43].

In this chapter, characterizations of QDs inside living cells are discussed; including (1) delivery methods to place QDs inside living cells, (2) properties of QDs within single cells with control experiments; and (3) potential issues and limitations of using QDs as temperature markers inside single cells.

3.2 Intracellular Delivery of Quantum Dots

The ability to tag and track sub-cellular structures with QDs in living cells represents a powerful tool in cell biology. The first experiment where semiconductor CdSe/ZnS nanocrystals were used was to stain F-actin in fixed cells [87]. Afterwards, a variety of experiments have tagged QDs to specific molecules in cells and tissues, both in live and fixed specimens. QDs can be internalized by cells, by either receptor-mediated [117] or nonspecific endocytosis [7, 8]. The internalized QDs accumulate in vesicles in the perinuclear region [7, 118]. For example, Dubertret et al. have demonstrated that encapsulated nanocrystals in phospholipid block–copolymer micelles can enter cells for both in vitro and in vivo imaging experiments [97]. Matteakis and coworkers [119] have used peptide-mediated transportation to incorporate QDs into a variety of live mammalian cells.

Cells can also be loaded with QDs by microinjection. Dubertret *et al*. [97] microinjected phospholipid-coated QDs into early-stage *Xenopus* embryos and tracked the embryogenesis using fluorescence visualization. The microinjected QDs were homogenously distributed

throughout the cell and were not compartmentalized. Derfus *et al*. studied and compared both biochemical (translocation peptides, cationic liposomes, dendrimers) and physical methods (electroporation and microinjection) of delivering QDs into cells (Figure 3.4) [10]. In their study, cationic liposomes provided the highest delivery efficiency of QDs to live cells, and QD aggregates of several hundred nanometers in diameter were formed during the internalization process. Electroporation is an efficient scheme to deliver QDs to the cytoplasm for a large population of cells with large aggregations. In contrast, microinjection delivers QDs to the cell interior as monodisperse nanoparticles.

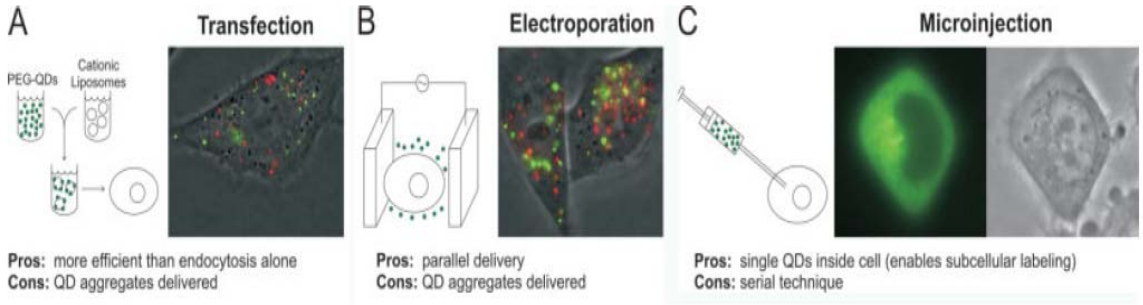

Figure 3.4 Comparison of QDs delivery methods inside cells. (A) transfection; (B) electroporation; (C) microinjection [10].

3.3 Cell Culture with Intracellular Quantum Dots

Experimentally, NIH/3T3 (CRL-1658, American Type Culture Collection) cell line was used to study the thermodynamics of the cellular behavior using QDs. NIH/3T3 cells are a standard fibroblast cell line and are originally derived from Swiss mouse embryo tissue. They have stable growth rate and their size is around 30 to 50 μm in diameter, under normal culture condition in the attached form. CdSe QDs were chosen as the temperature markers as we have characterized their temperature dependence properties in the previous chapter.

3.3.1 Cell Culture

NIH/3T3 mouse fibroblasts were cultured in high-glucose Dulbecco's modified Eagle's medium (DMEM, 30-2002, ATCC) with 10% calf bovine serum (30-2031, ATCC) with antibiotic mixture (1 % sodium pyruvate solution, 1% nonessential amino acid solution, and 1x Pen-Strep, Biofluids) in a 25 ml tissue culture flask. Cells were incubated at 37^{o}C with 5% carbon dioxide (CO_2) and fed with fresh growth media every 3-4 days, and sub-cultured when cells reached 80% confluence or more. The sub-culture protocol is listed below:

a. Aspirate and discard old culture medium.
b. Rinse once with 2 ml sterile Phosphate Buffered Saline (PBS) and aspirate.
c. Briefly rinse the cell layer with 0.25% (w/v) Trypsin - 0.53 mM EDTA solution to remove all traces of serum which contains trypsin inhibitor.
d. Add 2.0 ml of Trypsin-EDTA solution to flask and observe cells under an inverted microscope until cell layer is dispersed (usually within 5 to 15 minutes).

e. Add 6.0 ml of complete growth medium and aspirate cells to a centrifuge tube by gently pipetting.
f. Process cell suspension at 3000 rpm in centrifuge for 5 minutes. Gently aspirate and discard the supernatant media and leave the compressed cells at the bottom.
g. Add 6.0 ml of fresh growth medium to the centrifuge tube.
h. Add appropriate aliquots of the cell suspension to a new culture flask.
i. Incubate cultures at 37^{o}C.

In order to prepare the samples for the temperature measurements, 50 mm in diameter glass bottom Petri dishes (P50G-0-14-F MatTek) were used to culture the cell with cell density of 10,000 cells per well. After cells were sub-cultured into the glass bottom Petri dishes, they were incubated at 37^{o}C for 8 hours or reaching 30-40% confluence prior to the experiments. Cells were incubated with 3.7% formaldehyde in PBS at 37^{o}C for 10-15 minutes to fix the cells.

3.3.2 Quantum Dots Placements into Living Cells

QDs with emission peak at 655 nm (Qtracker Cell Labeling Kits, Q25021MP, Molecular Probes) were used for loading live cells in culture. The Qtracker Cell Labeling Kits use a custom targeting peptide to deliver QDs into the cytoplasm of living cells. Cytoplasmic delivery by this mechanism is not mediated by enzyme and the delivery is accomplished in less than one hour. Experimental protocols for labeling adherent cells listed by the provider were used and slightly modified as follows:

a. Prepare 10 nM labeling solution by pre-mixing 1 μL of Qtracker® Component#A and Component#B in a 1.5 mL microcentrifuge tube. Incubate at room temperature for 5 minutes and proceed immediately to step b.
b. Add 200 μL of fresh DMEM growth medium to the microcentrifuge tube and vortex for 30 seconds.
c. Remove the culture dishes from incubator.
d. Aspirate the old media, and rinse cells with 1x PBS once.
e. Add 202 μL of labeling solution to the glass bottom Petri dishes with cultured cells.
f. Incubate the culture dish at 37ºC for 60 minutes.
g. Wash cells three times with 1x PBS and once with DMEM growth medium.
h. Add 0.5-1 mL of complete growth medium.
i. Place the Petri dish on the imaging station for subsequent experiments or incubate at 37^{o}C up to 3 days. It is noted that a longer incubation time will lower the concentration of quantum dots in each individual cells due to cell growth and proliferation.

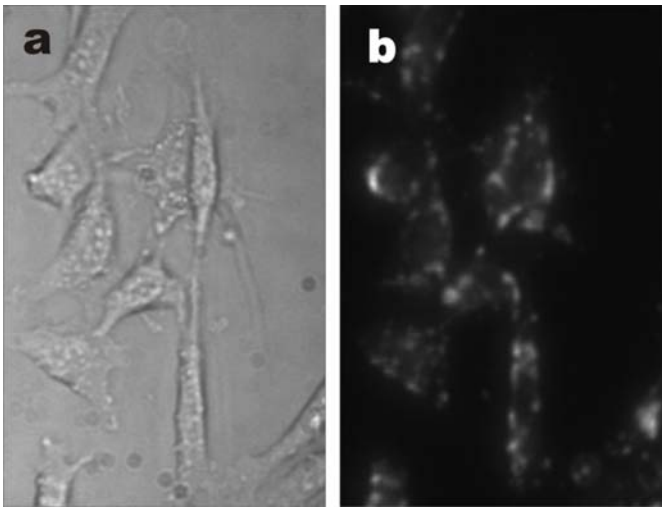

Figure 3.5 Wild field image (a) and fluorescent image (b) of NIH/3T3 cells with QDs inside.

Figures 3.5a and 3.5b show the wild field image and fluorescent image of NIH/3T3 cells with QDs inside from Olympus IX71 with 20x objective. It is observed that several clusters of aggregated quantum dots were delivered into cells. In order to verify that QDs were in the cytoplasm region of the cell, multiple-color staining of fixed intact cells with QDs was imaged by confocal microscopy (Zeiss LSM510 and Zeiss LSM700). After internalization of QDs, cells were fixed and stained with mitochondria or endoplasmic reticulum (ER), actin filaments, and nuclei. To label the mitochondria, live cells were cultured and stained with 100 nM MitoTracker Red CMXRos (M7512, Molecular Probes) for 30 minutes. Cells were subsequently fixed in 3.7% formaldehyde in PBS for 10 minutes and then permeabilized with a solution of 0.1% Triton X-100 for 3 minutes. Cells were then immunostained using standard methods with 165 nM phallotoxins (O7466, Molecular Probes) for 20 minutes for F-actin labeling and with 300 nM DAPI (D3571, Molecular Probes) for 3 minutes for nuclei stain. For endoplasmic reticulum stain, we used SelectFX Alexa Fluor Labeling Kit (S34200, Molecular Probes) and followed the suggested protocol for fixed cells labeling. Figures 3.6a shows the fluorescent image of QDs in white, and the composite image with mitochondria labeling in red, actin filaments labeling in green and nuclei labeling in blue. Similarly, Figures 3.6b shows a confocal fluorescent micrograph of cells with quad-labeling in quantum dots (white), endoplasmic reticulum (magenta), actin filaments (green) and nuclei (blue). The confocal images revealed that the internalized QDs were distributed inside the cytoplasm region and did not enter the nuclei.

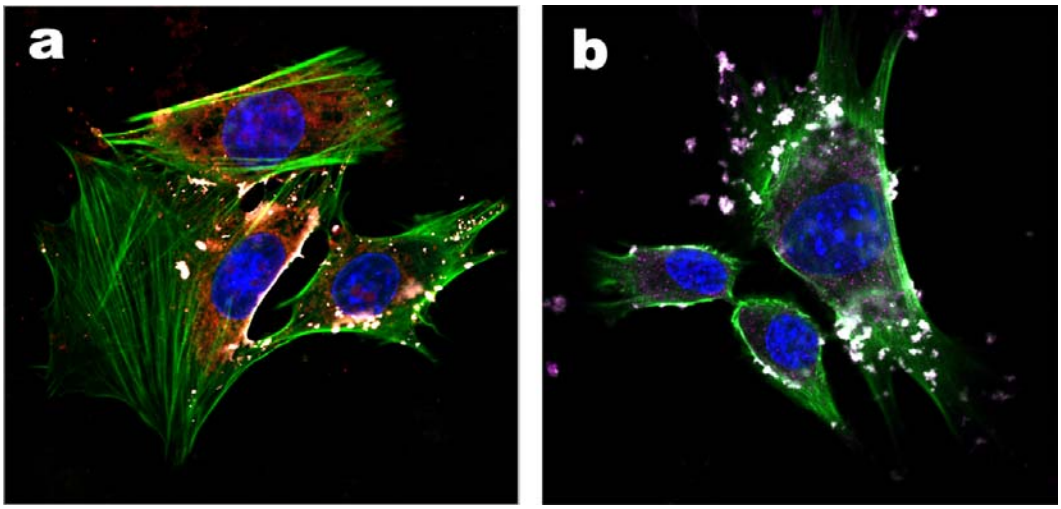

Figure 3.6 A confocal fluorescent micrograph of intact cells with quad-labeling with **a.** quantum dots (white), mitochondria (red), F-actin (green) and nuclei (blue). **b.** Sample with quad-labeling with quantum dots (white), endoplasmic reticulum (magenta), F-actin (green) and nuclei (blue).

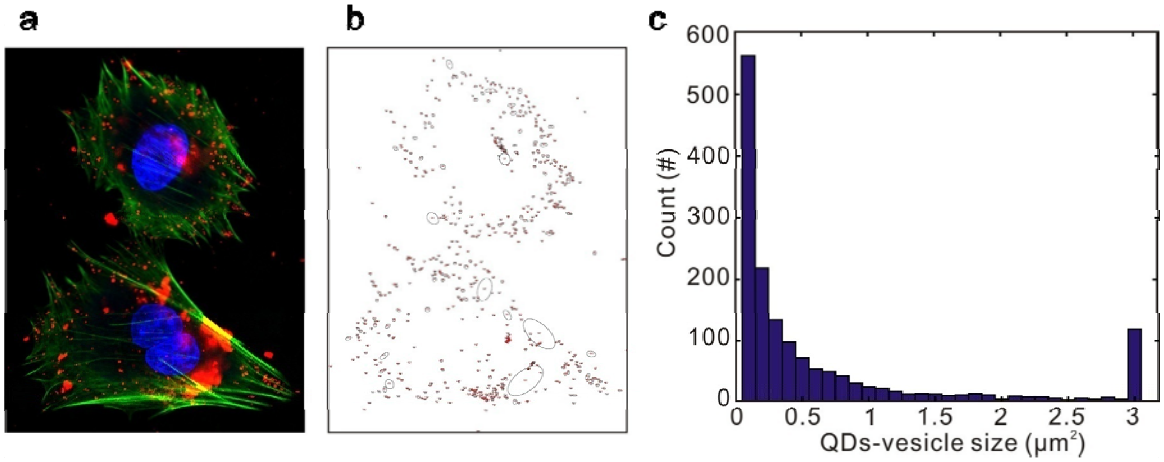

Figure 3.7 a. A confocal fluorescent micrograph of cells with QDs shown in red. **b.** Outlines of QDs-vesicles shown in **a.** **c.** The histogram of the distribution of sizes of QDs-vesicles. Vesicles' sizes larger than 3 μm^2 are shown as 3 μm^2 in this plot.

The delivery protocols of QDs were based on endocytosing into the cells and QDs were encased and confined in endocytotic vesicles. The size of QDs-vesicles was estimated by confocal fluorescent images and analyzed by ImageJ software (NIH). The diameter of the vesicles were mostly from 200 nm up to 3000 nm or larger, and the histogram of the vesicle sizes is displayed in Figure 3.7, for a total of 1546 vesicles.

3.3.3 Reference Quantum Dots Trace

The internalized QDs served as temperature markers and temperature readouts were calibrated with respect to extracellular QDs immobilized on the surface of the sample chamber.

In order to have reference temperature, a protocol was developed to leave some QDs vesicles outside the living cells. A homogeneous layer of collagen I (C3867, Sigma-Aldrich) with embedded QDs was coated on top of the glass bottom Petri dishes. Cells were seeded onto the QDs layer and they engulfed and absorbed QDs as they migrated. Surfaces that were not in the cell migration path could leave behind a layer of QDs, as illustrated in Figure 3.8a. The detail protocols are listed below:

a. Pre-mix collagen coating buffer. Add 100 μL collagen stock solution to 4.5 mL PBS at pH 7.3 and store at 4°C.
b. Add 1 mL of collagen coating buffer (step a.) per Petri dish and incubate at 37°C for 2 hour.
c. Pre-mix 1 μL of Qtracker® Component A and 1 μL of Component B in a 1.5 mL microcentrifuge tube. Incubate for 5 minutes at room temperature. Prepare the solution right before step d.
d. Carefully aspirate the residual collagen solution and leave a thin layer of collagen solution on the glass bottom surface.
e. Add 20 μL PBS to pre-mix QDs solution and vortex the QDs working solution for 30 seconds.
f. Immediately add 22 μL QDs working solution onto the wet collagen layer.
g. Leave the chamber to dry under UV light in the sterile laminar flow hood.
h. Trypsinize the cells by adding 1 mL of 0.25% trypsin to the culture flask. Incubate until the cells begin to detach from the dish. Add 10 ml of complete growth media and transport the suspended cells to a centrifuge tube.
i. Count and determine the number of cells required for a final density of 10,000 cells per Petri dish.
j. Pellet this required number of cells by centrifugation at 200*g* at room temperature for 5 min. Discard the supernatant.
k. Re-suspend the cells in 1 ml of complete growth media and add to Petri dish with QDs layer on top of the surface.
l. Incubate at 37°C for 24 hours.

Figure 3.8b shows the fluorescent image of NIH/3T3 cells with QDs, and the yellow lines indicate the outlines of cells. Figure 3.8b was captured about 4.5 hours after the sample preparation. Cells have attached to the surface and migrated very little, such that QDs were embedded in the collagen-QDs layer as observed. Images from the confocal microscope in Figure 3.6 and 3.7 confirm that QDs were located inside the cells. By this assay, QDs left outside of cells can be very close to the living cell, which can be captured simultaneously in one field of view under microscopy imaging. Those extracellular quantum dots could serve as markers for temperature references. Extracellular QDs are also useful for image calibration for potential mechanical drift during long-term observation.

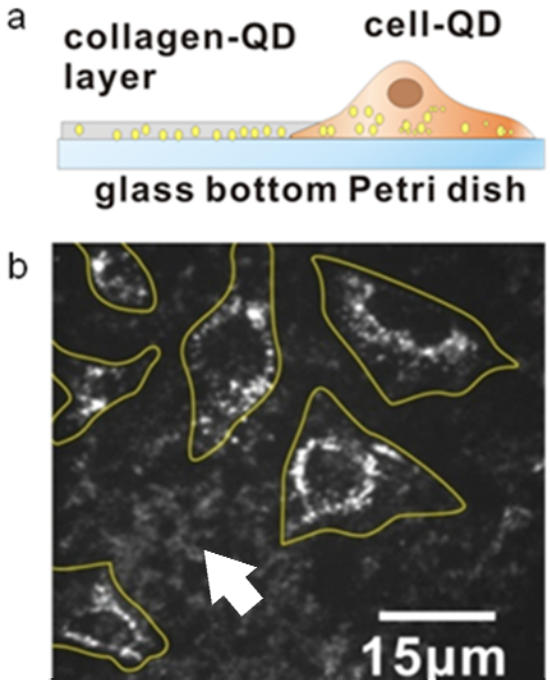

Figure 3.8 a. The schematic drawing shows that collagen-QDs layer serving as the reference local temperature markers. **b.** The fluorescent image shows both cell and collagen-QDs layer. The yellow lines indicate the outlines of living cells. The arrow indicates the collagen-QDs layer.

3.3.4 Viability Study

The cytotoxicity of the materials use in Qtracker® Cell Labeling Kits has been tested in a variety of cell lines including CHO, HeLa, U-118, 3T3, HUVEC, and Jurkat cells. Labeling with Qtracker® Cell Labeling Kits should exert minimal impact on cellular surface expression, cell proliferation, cellular enzyme activity, and cell motility. The effect of QDs loading on cellular viability was examined using dye exclusion method by trypan blue stain. In a viable cell, trypan blue is not absorbed since cells are selective in compounds passing through their membranes. On the other hand, trypan can penetrate the membranes of dead cells. The detail experimental procedure for the viability study for cells with intracellular QDs was described as the following steps:

a. Load QDs into NIH/3T3 cells described previously.
b. Place the glass bottom culture dishes on the temperature controller plate for 10 to 20 minutes.
c. Cell layer was dispersed by 0.25% Trypsin - 0.53 mM EDTA solution.
d. Cell suspensions were stained by 0.4% Trypan blue with DMEM for 5 minutes at room temperature.
e. The rate of viable cells was counted under Hemocytometer.

The results show that the viability of NIH/3T3 cells is not affected after QDs labeling, both under 37^{o}C and room temperature incubation. Table 3.1 summarized that labeling with

QDs and incubating without CO_2 concentration regulated environments for 20 minutes has no significant effect on cell viability.

	Viability
NIH/3T3 Cells 37 °C and 5% CO_2	97%
NIH/3T3 Cells Room temperature	95%
NIH/3T3 Cells with QDs 37 °C and 5% CO_2	97%
NIH/3T3 Cells with QDs Room temperature	94%

Table 3.1 Viability study of NIH/3T3 cells with quantum dots internalization.

3.4 Temperature Dependence of Quantum Dots in Single Cells

3.4.1 Temperature Controller

In order to regulate the temperature of the culture dish, a temperature control plate was designed and machined in-house. The temperature control plate has been installed the stage of a microscope to hold one Petri dish with 50 mm in diameter. The temperature control plate was made by brass (brass alloy 360, Metal Supermarkets, Redwood City) for the purpose of fast heat conduction, and machined in the mechanical engineering machine shop at UC Berkeley. Thermoelectric Peltier temperature control units were attached to the brass plate by silver thermal adhesive (TE-ASTA-7G, Custom Thermoelectric, Inc.) and used to regulate the temperature of Petri dish. Eight small Peltier units (No. 81162, Ferrotec) were used at the bottom of Petri dish and two large Peltier units (No. 83335, Ferrotec) were used to control the temperature of the brass plate. Figure 3.9 shows the temperature controller plate on top of the microscope stage. A thermocouple (5SC-TT-K-36-36; Omega Engineering, Inc.) was placed at the center of Petri dish to monitor the temperature of the cell culture. A temperature controller (FTC controller, Ferrotec) and two DC power supplies (E3612A, Hewlett-Packard, and 285-1616-ND 12 V, 26 A, Digi-Key Corporation) were connected to Peltier units to regulate the temperature.

Figure 3.9 Temperature control plate.

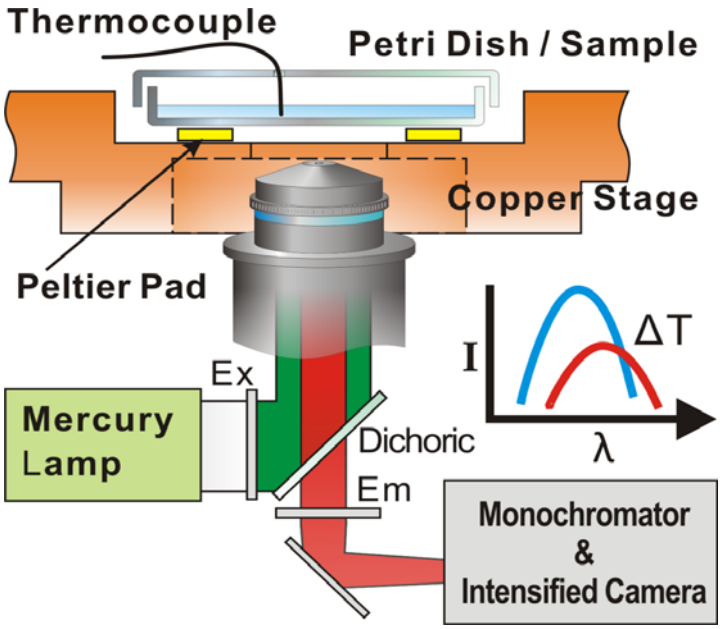

Figure 3.10 The optical setup of the cellular temperature measurement via spectral shift of QDs.

3.4.2 Experimental Setup

The experimental configuration is illustrated in Figure 3.10. The Petri dish sample chamber with an embedded thermocouple was mounted on the Peltier temperature control unit. The entire platform was secured on an inverted microscope (IX-71, Olympus) with a mercury lamp as excitation light source. The attenuated and spectrally filtered exciting light was directed through the microscope objective (20x or 40x) and focused on the sample. The emission from the cell and endocytotic quantum dots was collected by the same objective, channeled through an emission spectral filter and a spectrograph (SP2150i, Princeton Instruments/Acton-Research,

grating 600 g/mm blazed at 500 nm) for resolving the quantum-dot emission spectra, and imaged by an intensified camera (Cascade 512B; Roper Scientific) with single-molecule sensitivity.

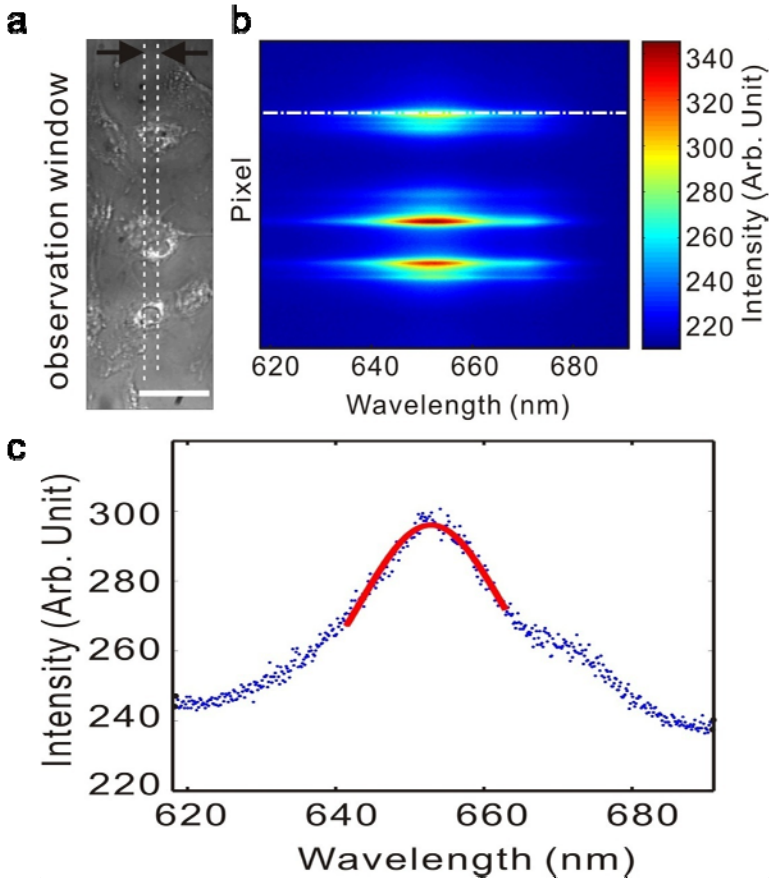

Figure 3.11 The spectra measurement of QDs. **a.** The wild field image of three cells within the observation field. Scale bar is 15 um. **b.** The spectra of QDs at corresponding vertical axis of the observation slit of **a.** **c.** The spectrum (blue dots) showed at white dash line of **b.** and its fitted curve (red solid line).

The entrance slit of the spectrograph served as a means to minimize the influence of other QDs outside the centerline region and had an opening of 100 μm in width in spectra imaging mode. The dispersion of the optical setup (600 g/mm grating in spectrograph) is 8.857 nm/mm at the image plane. The size of the image sensor is 8.2×8.2 mm, with 512×512 pixels, which covers about 70 nm wavelength differences in the spectra mode. The spectra resolution of the experimental setup is 0.14 nm/pixel. To cover larger area of cells with more QDs signals in a field of view, 20x objective was used to record the emission spectra. In the position axis, along the entrance slit, the spatial resolution is 800 nm per pixel. In the axis perpendicular to the entrance slit, the observation field is limited by the width of the entrance slit, which is 100 um in width at the image plane. At the sample plane, the width of the entrance slit is 100/20 = 5 um. Thus, in the position-spectra images, one wavelength data point corresponds to an average emission peak from a rectangular area, 5 um by 800 nm, of the sample.

To locate intracellular quantum dots, the grating of the spectrograph is set at the zero-th order for imaging (Figure 3.11a). Once a suitable cell and quantum dot spot is located, the grating is switched for time-dependent spectroscopic investigation (Figure 3.11b). The spectra images were collected at integration times from 30 to100 ms via WinView32 (Roper Scientific). In Figure 3.11b, three groups of QDs shown in the spectral mode correspond to three cells shown in Figure 3.11a. Each cell covers about 50 or more pixels in the vertical direction. The details inside the cell can be extracted by looking at the wavelength shifts of individual pixels.

3.4.3 Spectra Characterization on Dead Cells

Dead cells with embedded QDs were tested to establish the optical characteristics of QDs in the range of 17-47°C. Spectra were captured when the culture dish reached steady state temperature and processed by procedures detailed in chapter 2.5.3 and 2.5.4 as shown in Figure 3.12. It is observed that spectra shifted toward longer wavelength with increasing temperature and the peak wavelength-temperature slope is 0.06 nm/°C, which is smaller than the single QDs experiments presented in chapter 2. The differences in the slope magnitude may be attributed to different surface coatings, wet samples, and cellular components.

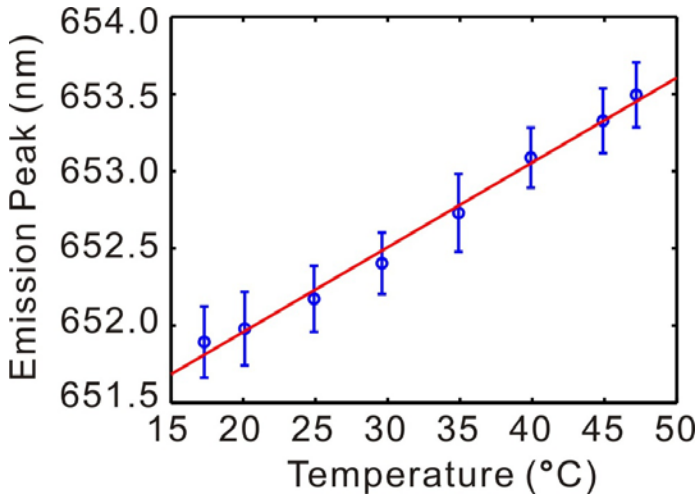

Figure 3.12 The spectral characteristic of QDs inside cells at different temperature (17°C to 47°C).

The intensity of excitation light source does not affect the emission spectra of QDs. We characterized emission spectra of QDs in dead cells with respect to input excitation power. Figure 3.13 shows plots of the peak-wavelength with respect to four excitation powers at room temperature. Red lines indicate the average value and blue lines indicate the upper and lower quartiles of the data. Black lines indicate the measured extreme values. The average emission peaks remained stationary under four different excitation intensities. It is found that lower excitation power resulted in broader spread of peak wavelength probably due to the poor signal-to-noise ratio in low light conditions.

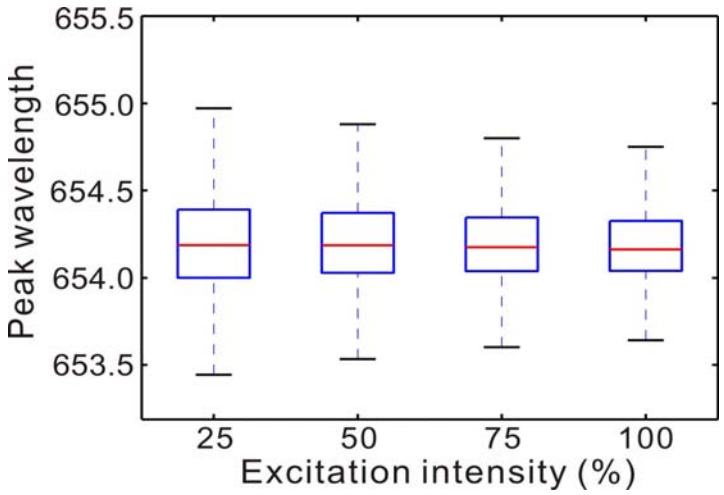

Figure 3.13: The spectral characteristic of QDs inside cells at different excitation intensity. Red lines indicate the average value, while blue lines indicate the upper and lower quartiles of the data. Black lines indicate the extreme values.

Furthermore, QDs are known to have high resistance to photo bleaching for long-term studies. Emission spectra of QDS in dead cells were recorded for 1 hour at 37°C as displayed in Figure 3.14. The measured temperatures of dead cells varied within ±1°C, due to the overall system measurement errors.

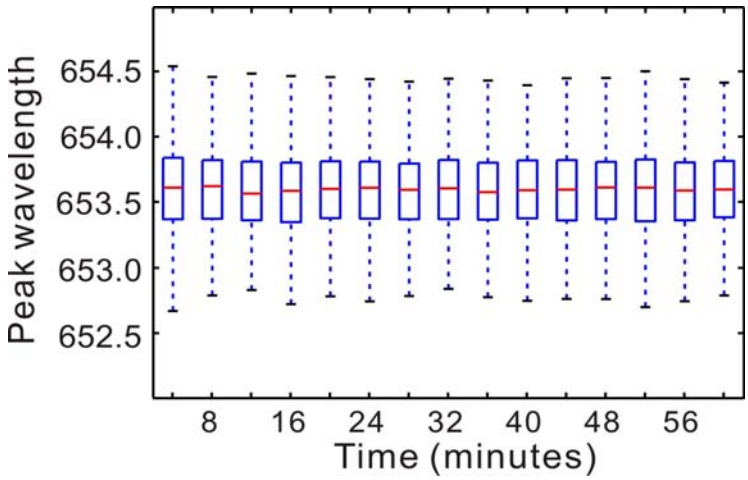

Figure 3.14 The recorded spectra of QDs inside dead cells at 37°C for 60 minutes. Red lines indicate the average value, while blue lines indicate the upper and lower quartiles of the data. Black lines indicate the extreme values.

3.4.4 Effects of Intracellular pH on Spectra of QDs

Spectroscopic properties of organic dyes tend to be a strong function of pH such that organic dyes are not appropriate tools for local temperature measurements inside living cells, where pH is expect to differ in different compartments and time. CdSe/ZnS core/shell quantum dots, on the other hand, have been shielded from the chemical environment by the ZnS shell and

streptavidin coating. Therefore, it is expected that the impact of pH changes to the spectra of QDs should be small. Here, characterizations of QDs spectra changes with respect to pH values inside living cells are conducted. The experimental procedure is listed below:

a. Pre-mix different buffer solutions with pH 4-10 with increment of 1 pH by buffer pH 4 and buffer pH 10 (Fisher Scientific).
b. Fix cells with 3.7 % formaldehyde in PBS for 10 minutes.
c. Rinse with 1x PBS three times.
d. Add 1 mL buffered solution to the Petri dish.
e. Control the Petri dish temperature to 37^{o}C and capture spectra information under imaging station.
f. Keep the Petri dish in the temperature control plate. Aspirate the buffer solution and rinse with 1x PBS three times.
g. Add 1 mL next level buffered solution to the Petri dish.
h. Repeat steps e, f, and g until all pH level are tested.

The results are displayed in Figure 3.15. Across a range of 5 pH scales from 4-10, the peak-wavelength changed about 0.029 nm per 1 pH value changes. Since it is difficult to maintain 1 pH value changes at steady-state, the impact of pH value to the spectra changes of QDs is expected to be negligible and should be ignored.

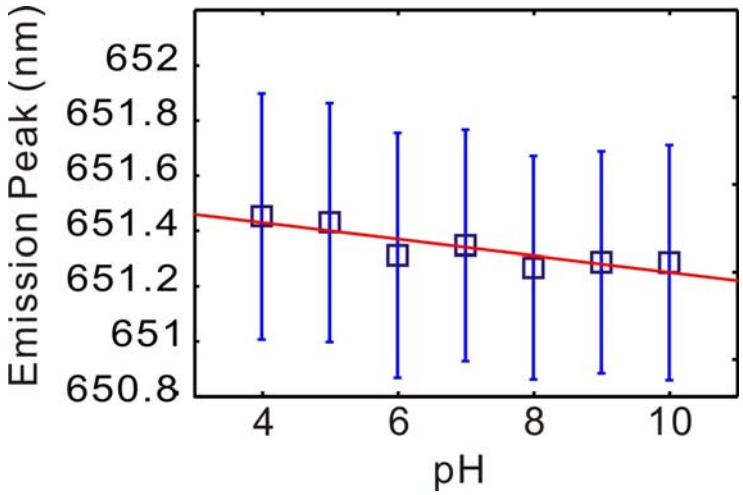

Figure 3.15: The spectral characteristic of QDs inside cells at different pH level (4 to 10).

3.4.5 Living Cells Observations

Temperature profiles of living cells were measured by QDs at room temperature using NIH/3T3 cells for 30 minutes and 12 seconds per frame with 30ms integration time for a total of 150 frames. The emission peak wavelength characterize from the first frame were used as the reference to compute the relative shift of the peak wavelength for the rest of 149 frames. Results are displayed in a plot as function of time verse relative wavelength shift in Figures 3.16 for living cells in (a) and fixed dead cells in (b). The solid lines represent the mean value of the spectra shift, while the dashed lines are the distribution of the standard deviation. Living cells exhibited a larger distribution of the relative spectra shifts, meaning the relative temperature

changes, than that of dead cells. This is expected as living cells have a temperature discrepancy due to various cellular activities, and dead cells are at the environmental temperature.

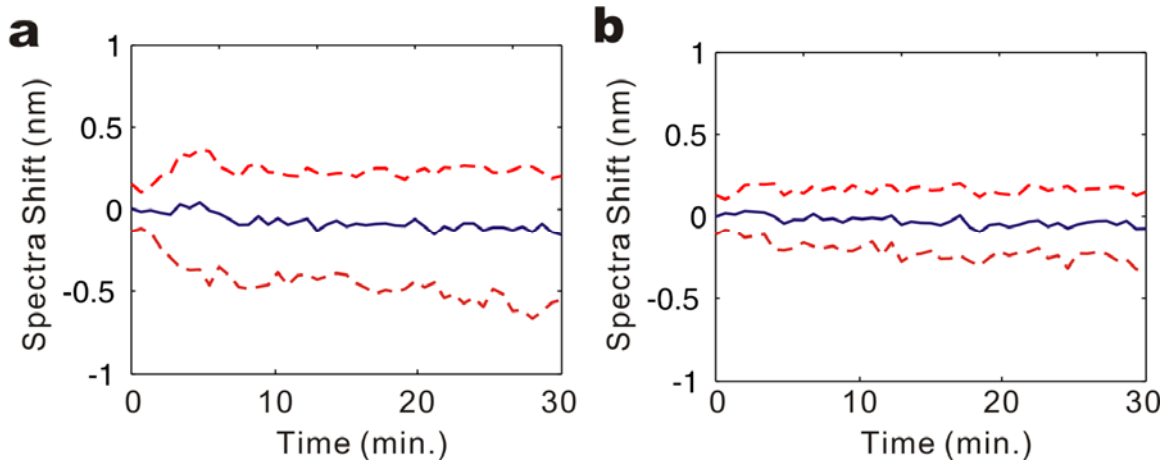

Figure 3.16 Recorded relative spectra shift of QDs in **a.** living cells and **b.** dead cells. The solid lines represent the mean value of the spectra shift, while the dashed lines are the distribution of the standard deviation.

Endocytotic QDs gathered together in the form of vesicles inside cells and they moved from site to site. The transport of QDs-vesicles has been observed in our samples, as illustrated in time-lapse fluorescent images (60 seconds separation between images) in Figure 3.17. The fluorescent images are overlaid with differential interference contrast (DIC) images took by Zeiss 700 confocal microscope with 40x objective. It is necessary in the current spectra measurement that QDs remained stationary to characterize their peak wavelength. The movements of QDs would cause altered light path and scatter the spectra information to result in different peak wavelengths in the analyzing process. While only small portion of QDs-vesicles were moving and most QDs remained stationary, it is necessary to locate stationary QDs for spectra measurements to minimize the system error due to movements of QDs.

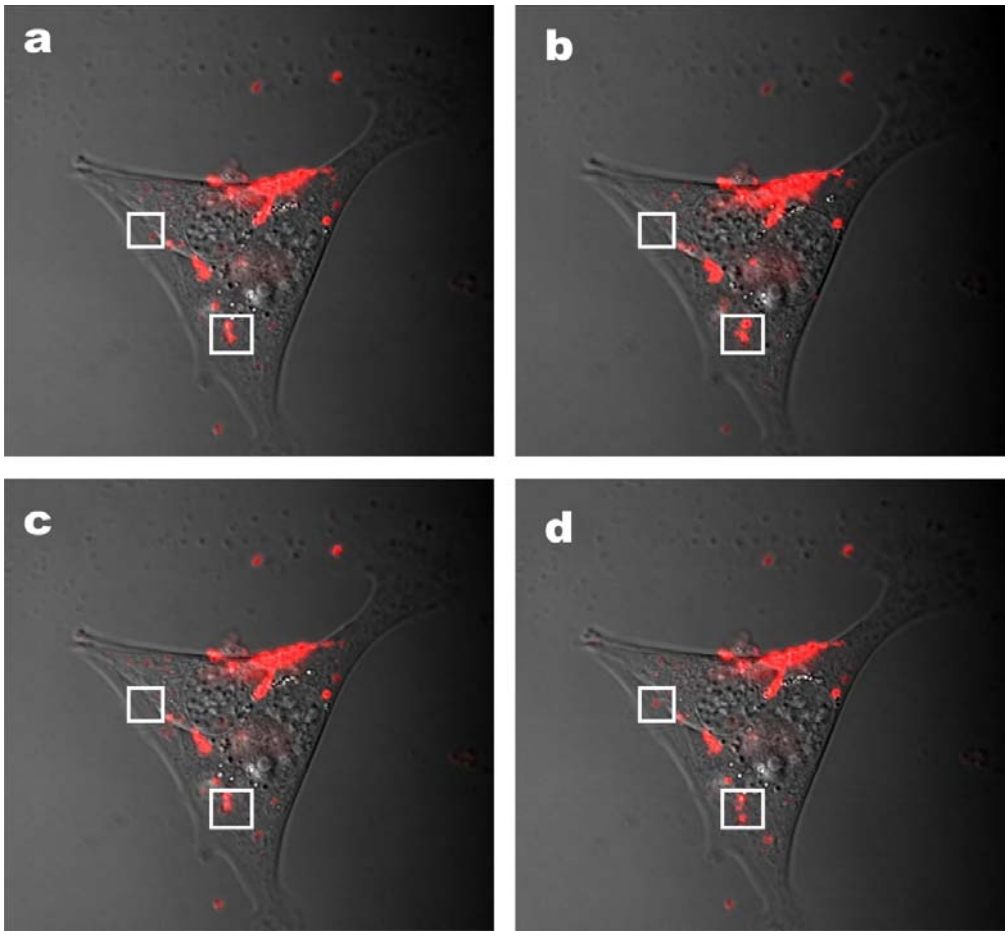

Figure 3.17 Time lapses DIC images are combined with fluorescent images of QDs shown in red. The white box indicates the location of one moving QDs-vesicle in each frame. These photos were separated by 60 seconds.

3.4.6 Thermal Effects of Adding QDs into Cells

Thermal properties of QDs have been studied. From QDs fluorescent images, it is estimated that the area fraction of QDs with respect to living cells was 3~8%, depending on the loading concentration of QDs. The thermal mass of QDs per unit volume was calculated using $C = \rho C_p$, where C is thermal mass [JK^{-1}], ρ is density [kg m^{-3}], and C_p is specific heat [J $kg^{-1}K^{-1}$]. For CdSe quantum dots, ρ = 5810 kg m^{-3}, and C_p = 261 J $kg^{-1}K^{-1}$. The cytoplasm was approximated as water, where ρ = 1000 kg m^{-3}, and C_p = 4.2 kJ $kg^{-1}K^{-1}$. The ratio of thermal mass of CdSe quantum dots to cytoplasm was approximated as 1:2.77. Therefore, 5% volume ratio of QDs, for instance, would have resulted thermal mass increases of 1.8%. This number is relatively small to affect the thermal characteristics of living cells.

Next, thermal diffusivity of the probing system and cytosol are analyzed. The thermal diffusivity can be calculated as $D = k/\rho C_p$, where D is thermal diffusivity [m^2s^{-1}], k is thermal conductivity [$Wm^{-1}K^{-1}$], ρ is density [kg m^{-3}], and C_p is specific heat [J $kg^{-1}K^{-1}$]. The thermal conductivity of CdSe is about 6.2 – 9 W/mK, while water is 0.58 W/mK. The thermal diffusivity

of the CdSe QDs is 6.1×10^{-6} m^2/s, while that of water/cytosol is about 1.38×10^{-7} m^2/s. It is noted that CdSe is encapsulated by bio-materials. If CdSe QDs line up side-by-side with a separation of 200nm as illustrated in Figure 3.18, the combined thermal diffusivity of QDs/biomaterials can be estimated by $\frac{x_{QD}^2}{D_{QD}} + \frac{x_{H20}^2}{D_{H20}} = \frac{x_{all}^2}{D_{all}}$, where x_{QD} is the diameter of the QD core/shell and x_{H20} is the diameter difference between biomaterial coating and QD core/shell. The overall thermal diffusivity is estimated as 1.7×10^{-7} m^2/s. In the assumed model, the heat transfer between them is in the same order as the cell to cytosol. Therefore, thermal diffusivity between accumulated QDs and cells are similar in order and its thermal impact is negligible to the cellular temperature distribution.

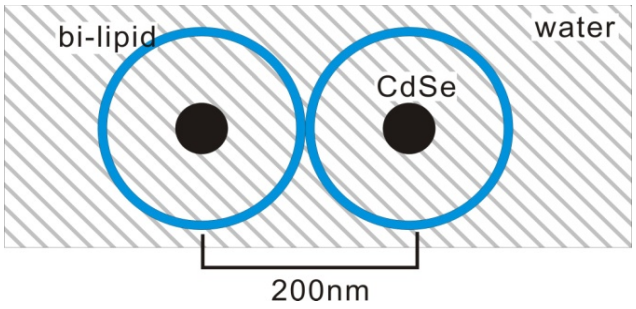

Figure 3.18 Schematic illustrate the QDs line up side-by-side for calculating thermal diffusivity of QDs-cells system.

3.4.7 Error Estimate

Main experimental errors come from three sources: (1) the drift of the stage and/or the movements of QDs and cells, (2) spectrum variation of quantum dots, and (3) the goodness of the curve fitting of raw data. QDs emission spectra have been obtained by an emission spectral filter, a spectrograph and a 100μm-wide entrance slit. Since the entrance slit is not infinite small, the relative position of the QDs (as a point light source) to the slit can alter the observed spectra. The dispersion of the grating at 655nm is 8.857 nm/mm and the pixel size of the CCD chip is 16×16 μm, with 512×512 pixels. In the extreme cases, the peak wavelength shift at two edges of the 100 μm-wide slit can be as large as 0.9 nm. This effect is minimized by tracing the same QDs at the same location to get the relative spectral shift. However, this doesn't solve the issues if cells migrate and/or the stage drift slightly over time.

Secondly, the QDs spectra varied from dots to dots due to the variation in the size and shape of individual synthesized QDs, as well as surface coatings. At a given temperature, the standard deviation of the distribution of QDs' emission peaks is about 0.25 nm (Figure 3.19). This error is partially related to the fabrication process and size control of QDs. The third error is from the least squares error from curve fitting at the peak region of the raw data. We have assumed that the emission around the peak wavelength followed Gaussian distribution and preformed the curve fitting near the peak region. The fitting error is directly related to the data acquisition, which is determined by experimental setup, sample focusing, possible movement of QDs inside the cell during experiments, and camera noises. In general, we estimate the Gaussian curve fitting error of our raw data is less than 0.1 nm in our current setup. The total worst error estimate in our measurement scheme can be calculated as the combination of these three, e^2 =

$e_{mov}^2 + e_{QD}^2 + e_{fit}^2$, where e_{mov} is 0.9 nm, e_{QD} is 0.25 nm, and e_{fit} is 0.1 nm. Therefore, the system error is about 1 nm in the worst cases. In our experiment, we recorded the same sets of QDs' emission peaks and computed the relative peak shifts and compared the emission peaks of the same population of QDs at same location such that e_{mov} and e_{QD} can be ignored. Therefore, our measurement error can be approximated as the fitting error e_{fit}, which is about ±1.6°C.

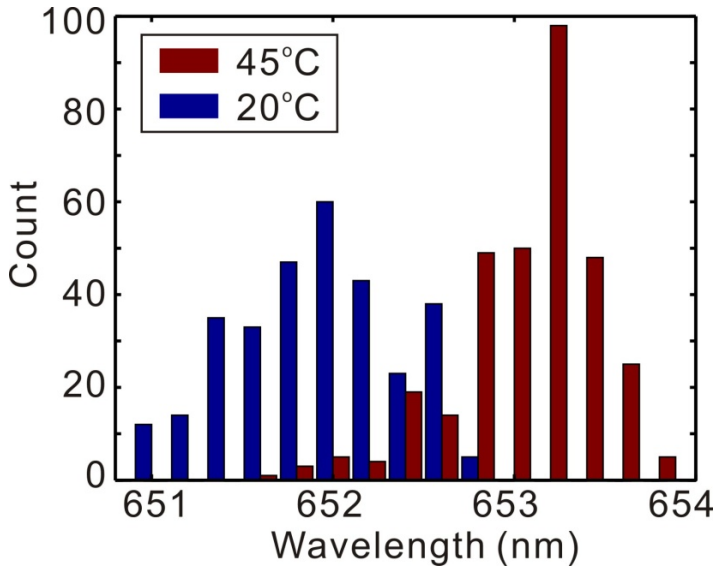

Figure 3.19 The distribution of peak-wavelength of quantum dots, at 20 °C and 45°C.

3.5 Summary

Internalization of QDs has been achieved by endocytosis which spreads the QDs across cytoplasm. A collagen layer with fixed QDs was left at the surface of the culture dish to sever as an *in-situ* temperature reference. A viability study showed that the internalized QDs have little effects on the cell culture and cell viability. It has been characterized that the temperature-dependent spectra characteristics of QDs were not influenced by the cell membrane and cytosol as QDs are embedded inside the cells. The peak-wavelength and temperature relationship has been characterized as linear with a slope about 0.06 nm/°C for QDs inside living cells. It has also been demonstrated that pH values has little effects to the spectral shift of QDs. Furthermore, the temperature resolution of this measurement technique was estimated about 1^oC, under current experimental setups and data analysis procedures. In the thermal analyses, the influence of small amounts of QDs won't change the heat transfer properties of living cells or interfere cellular temperature. Therefore, these characterizations and analyses support that this technique can be widely used in thermodynamic aspect of cell study for biological system.

Chapter 4
Thermogenesis in Single Living Cells

4.1 Introduction

Heat generation in cellular activity has been studied with various aspects, such as indication of metabolic heats, immunomodulators on cellular activity, intracellular enzyme activity as well as the effectiveness of drugs [6]. Heat shock proteins are known to play significant roles in signal pathway mediation, apoptotic machinery [5], and immune responses [3, 120]. Adaptive, no-shivering thermogenesis [121], which is influenced by numerous environmental factors, regulates and produces heat by uncoupling oxidative phosphorylation, usually associated with mitochondrial uncoupling proteins [122-124]. However, these researches are poorly understood in depth owing to the nature of difficulties in examining the temperature variations through the standard molecule and biochemistry analysis tools.

In this chapter, the fundamentals and developments of cellular thermogenesis are reviewed. QDs were used as the temperature sensors to investigate activities of cellular thermogenesis in two experiments. First, thermogenesis was triggered by adding chemical stimulus to the culture environment, and the temperature profiles of living cells were continuously monitored. Secondly, cold shock was used as an external temperature stimulus to detect heat generation in living cells. Furthermore, a different setup is discussed to create two-dimensional temperature maps of living cells by scanning confocal imaging.

4.2 Cellular Thermogenesis

Virtually all levels of biological and biochemical processes are influenced by temperature, such as protein folding, diffusion dynamics, biochemical reactions, and membrane permeability. Therefore, it is useful to analyze energy expenditure of cellular system from a thermodynamic perspective. The key mechanism for living cells to regulate their temperature is thermogenesis which is the result of energy expenditure due to the metabolic processes [123, 125], such as those catalyzed by the mitochondrial respiratory chain, and those that consume ATP (for example, Na^+/K^+ ATPase, Ca^{2+} ATPase, and actinomyosin ATPase) or heat production in response to environmental perturbations [126, 127]. Adaptive thermogenesis is defined operationally as heat production in response to environmental temperature, and serves the purpose of protecting the organism from cold exposure.

Metabolism, which involves the electron transport chain, ATP synthesis, and ATP usage, represents coupled reactions with reactants and products. For example, conversion of glucose to CO_2 generates NADH and FADH; oxidation of NADH and FADH results in pumping protons across the mitochondrial inner membrane and re-entry of protons by means of ATP synthase generates ATP (Figure 4.1). In order to increase the degree of heat generation, the balance of these couplings has to be perturbed [125]. Alternatively, increasing cellular activities by means of ATP consumptions can result in heat generation. For example, muscle relaxation and ion leaks (Na^+ in and K^+ leaking out across the plasma membrane and Ca^{2+} into the cytosol from intracellular stores) will utilize ATPs.

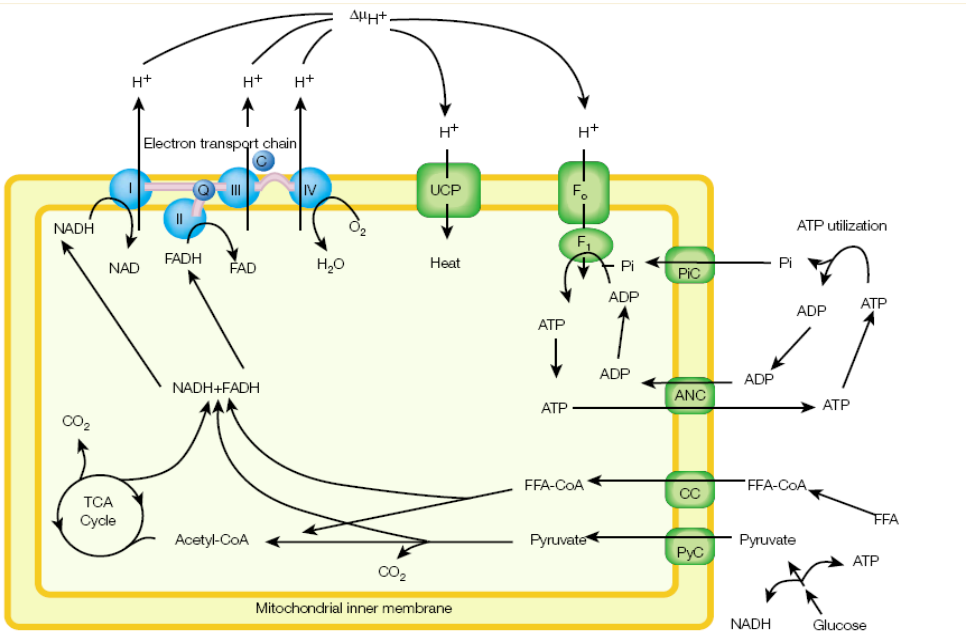

Figure 4.1 Mitochondrial energy metabolisms [121].

Mitochondria are extremely abundant in heater cells, comprising over 60% of total cell volume. Thermogenesis in heater cells is initiated by depolarization, which causes Ca^{2+} to release by the sarcoplasmic reticulum. ATP is then consumed by Ca^{2+}-ATPase, which returns Ca^{2+} to the sarcoplasmic reticulum. The increased demand for ATP required to sustain this cycle drives the heat generation. Thus, depolarization-induced Ca^{2+} entry into the cytoplasm causes ion cyclingmediated thermogenesis.

Energy consumption of cells also changes directly in response to environmental temperature. Oxygen consumption increases close to four fold in rodents after cold exposure (4°C) [128, 129]. With adaptive mechanism, thermogenesis in brown adipose and possibly other tissues can keep cells in desirable temperature [129]. Energy expenditure in humans, as a whole body, is also sensitive to environmental temperature, but the effect on metabolic rate is relative small. As a whole body, exposure to cold is detected by the brain, leading to activation of efferent pathways controlling energy dissipation. The main component of this response is the sympathetic nervous system, which heavily innervates thermogenic targets such as brown adipose tissue and skeletal muscle. Studies show that the sympathomimetic agents, such as β-adrenergic-receptor agonists, could cause an increase in energy expenditure which is comparable in magnitude to that induced by cold.

4.3 Cellular Temperature Responses to Chemical Stress

We first investigated the thermogenesis of living cells with respect to external chemical perturbation. Increasing Ca^{2+} concentration by ionomycin accelerates the activities of ion pumps and respiration rate in living cells and results in heat production inside the cells. Temperature responses of single living NIH/3T3 fibroblasts were recorded by QDs.

4.3.1 Experimental Setup

The experimental configuration was similar to those detailed in chapter 3 and illustrated in Figure 4.2. The glass bottom Petri dish was mounted on the stage of an inverted microscope (IX-71, Olympus) directly. A mercury lamp was used as the excitation light source. The attenuated and spectrally filtered exciting light was directed through the microscope objective (20x) and focused on the sample. The emission from endocytotic QDs was collected by the same objective, and channeled through an emission spectral filter. A spectrograph (SP2150i, Princeton Instruments/Acton-Research, grating 600 g/mm blazed at 500 nm) was used to disperse the emission light for resolving the quantum-dot emission spectra, and imaged by an intensified camera (Cascade 512B; Roper Scientific). With 20x objectives, the special resolution of each pixel is about 800 nm at the sample.

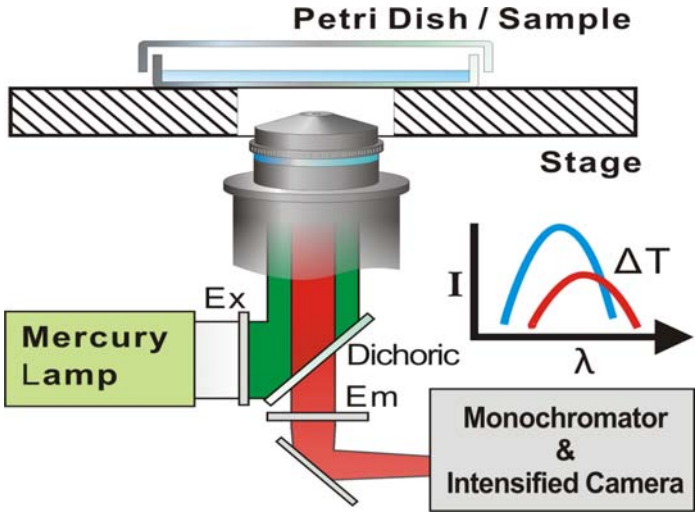

Figure 4.2 The optical setup of the cellular temperature measurement via spectral shift of QDs.

4.3.2 Procedure of Calcium Salt Influx

To trigger cellular thermogenesis, we used ionomycin to manipulate the extracellular calcium concentration. Cells were cultured in the glass bottom Petri dish at standard condition (37^{o}C and 5% CO_2) with implanted quantum dots as temperature markers. Prior to the experiments, the culture dish was lowered to room temperature, as the same temperature as other chemicals, to prevent temperature changes of the medium during addition of calcium solution. After 2 minutes into the recording, ionomycin (10 µL of 0.5 mM solution) was added to the culture dish, containing 500 µL of the medium, to the final concentration of 1 µM. Spectra images were recorded with 30-100 ms integration time for 15 minutes, with 6 seconds interval and 150 frames. The details of the ionomycin solution preparation and experimental procedure are listed below:

a. Make the stock solution, add 200 µL of sterilized methanol to the ionomycin vial (No. I-24222, Molecular Probes) to a final concentration of 6.7 mM, store at -20^{o}C.

b. Prepare working solution, transfer and warm the stock solution to room temperature.

c. Dilute stock solution 11 times in PBS, vortex for 30 seconds.

d. Transport culture cells from 37^{o}C incubator to room temperature for 5 minutes.

e. Rinse cells with 1x PBS three times at room temperature.

f. Add 500 μL complete growth media to Petri dish.

g. Place and secure the Petri dish on imaging station, locate cells with QDs.

h. Adjust the stage to have cells line up in the center of field of view, and close the entrance slit to 100 μm in width.

i. Start the spectra recording for 150 frames with 6 seconds intervals.

j. At 2 minutes into the experiments, (at 20th framed), add 10 μL of diluted ionomycin solution to Petri dish. Complete the imaging recording.

k. Fix the cells with 3.7% formaldehyde in PBS at 37^{o}C for 10 to 15 minutes.

l. Rinse cells with 1x PBS three times.

m. Repeat steps f-j for dead cells experiment.

4.3.3 Data Analysis

Spectra images were captured by using an Olympus IX71 inverted microscope with a 20x objective and an intensified camera with a spectrograph. The spectra images were collected at integration times from 30 to100 ms via WinView32 (Roper Scientific). Raw images were analyzed by MATLAB (Mathworks, Natick, MA). In the case of transient temperature studies, 150 frames were recorded for a total of 15 minutes with 6 seconds intervals. To distinguish QDs signal from background noise and cell auto fluorescence, a specific threshold value was manually chosen in each experiment to cut off the unwanted intensity profiles. When any intensity profile was below the threshold value, the temperature reading was not available.

Emission spectra were calculated by the Gaussian fit of the intensity-wavelength profile for each position and all 150 frames. The fitted peak-wavelengths were displayed in a pseudo color plot as functions of position along the entrance slit and time, as shown in Figure 4.3a. If living cells migrated or QDs moved slightly, the recorded results have skewed curves with respect to time as shown in Fig. 4.3a. This artifact can be fixed by data realignment (Figure 4.3b). The aligned data were subtracted the initial wavelength data in the first frame to obtain the relative spectra shift, which represent the temperature shift of the sample (Figure 4.3c). The linear relationship, 0.06 nm/°C, was used to calculate the relative temperature changes.

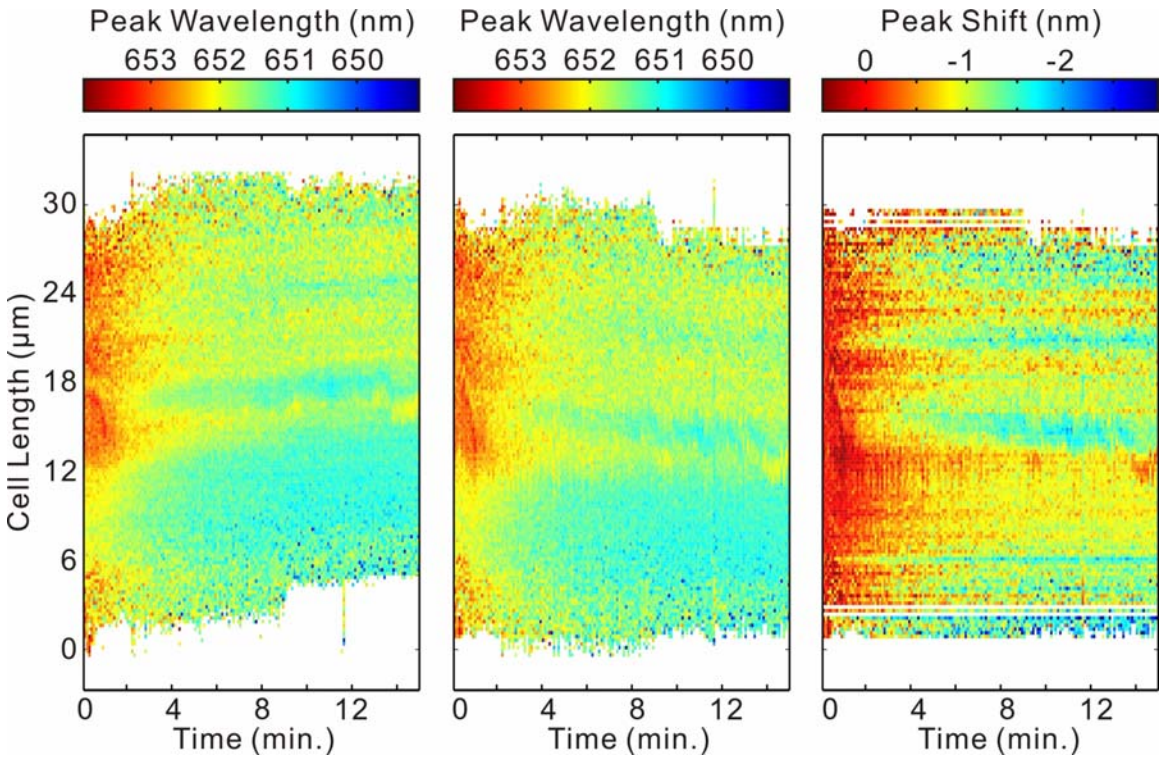

Figure 4.3: The post processes of the spectral data. **a.** The original fitted peak wavelength data of a single cell under cold exposure. **b.** The aligned peak wavelength data with respect to the initial recorded position. **c.** The relative peak wavelength shift with respect to the initial peak wavelength.

4.3.4 Calcium Concentration Indicator

Calcium concentrations in our ionomycin influx experiments were characterized by a fluorescent dye, fluo-4 (F10471, Molecular Probes) in a control experiment. Fluo-4 offers substantially bright fluorescence emission which indicates Ca^{2+} concentration at the range of 100 nM to 1 mM. Flou-4 was loaded to cells and a rise in intracellular [Ca^{2+}] was induced by ionomycin at 40 second into the experiment with a final concentration of 1 μM. The detail protocol is listed below:

a. Subculture NIH/3T3 cells in Petri dish for concentration of 10,000 cells per dish.

b. Prepare 250 mM stock solution of probenecid by adding 1 mL of Fluo-4 Direct™ calcium assay buffer to each 77 mg vial of water-soluble probenecid (Component B for Cat. nos. F10471) Vortex. Store unused probenecid stock solution at ≤–20°C.

c. Prepare the 2x Fluo-4 Direct™ calcium reagent solution with a final probenecid concentration of 5 mM. Add 10 mL Fluo-4 Direct™ calcium assay buffer and 200 μL of 250 mM probenecid stock solution to one bottle of Fluo-4 Direct™ calcium reagent (Component A).

d. Remove Petri dish containing cells from the incubator. Rinse with 1x PBS once.

e. Add 250 μL complete growth media to Petri dish.

f. Add 250 µL of 2x Fluo-4 Direct™ calcium reagent loading solution (step c.) to dish containing cells in culture medium.

g. Incubate Petri dish at 37°C for 45 minutes and at room temperature for 20 minutes.

h. Place the Petri dish under imaging station. Excite with 488 nm laser and collect emission with band pass filter 530/60 nm.

i. Locate the cells and record the fluorescent images for 3 minutes with 2-second interval.

j. At 40 second into the experiments, add 10 µL of diluted ionomycin solution to Petri dish. Complete the imaging recording.

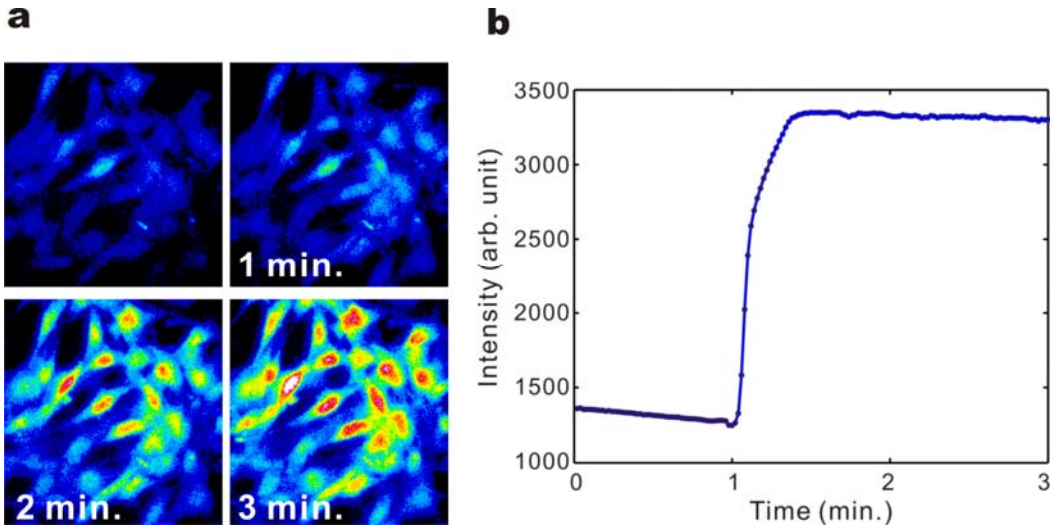

Figure 4.4 Fluorescence image of the Fluo-4 calcium indicator. **a.** Time course fluorescent image. The intensity is color coded from blue to green to red. **b.** The intensity plot of Fluo-4. Ionomycin with final concentration 1 uM was added 40 seconds after the recording started.

The time lapses of the fluo-4 fluorescent images are shown in Figure 4.4a, and the average intensity of fluo-4 is displayed in Figure 4.4b over time. The result indicated that the calcium concentration was elevated by about two orders of magnitude higher than the original value after ionomycin was added to the culture.

4.3.5 Results

Cells were incubated in standard cultural media with Ca^{2+} concentration at 10~100 nM and ionomycin were added 2 minutes into the experiments to make the final [Ca^{2+}] at 1 µM. Figure 4.5 shows one typical measurement result, calculated by relative spectra shift, versus time, where dots are the average temperatures, and lines show the ranges of lower quartiles to upper quartiles of the data. It is observed that three minutes after the calcium influx, approximately 1.5°C temperature rise was recorded in living cells while dead cells shows no observable temperature change with white noise of 1°C. Using z-test statistics, the dead cell experiments showed a 95% confidence interval of -0.005 to +0.009 nm in average spectra-shift, which implied calcium ions concentration didn't affect the emission spectra of QDs. Figure 4.6 shows

the temperature map of a single living cell as function of position and time, with calcium influx at 2 minutes into the experiment. The y-axis represents the location of the cell along the entrance slit of the spectrograph, and color of pixels indicates the relative temperature changes. The thermal image shows hot spots along the detection slit which illustrates that QDs are capable of providing intracellular temperature difference. This thermal image provides spatial resolution of 800 nm per pixel with 20x objective.

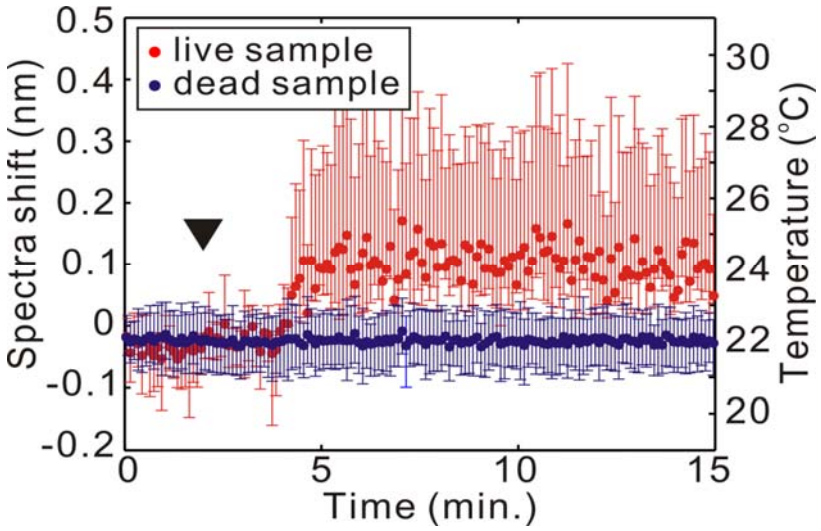

Figure 4.5 The temperature responses of one living cell and one dead cell with calcium influx as function of time. Ionomycin was added to the sample at the moment as the arrowhead indicated to achieve 1 μM final concentration of ionomycin. The dots are the average temperatures, and lines show the ranges of lower quartiles to upper quartiles of the data.

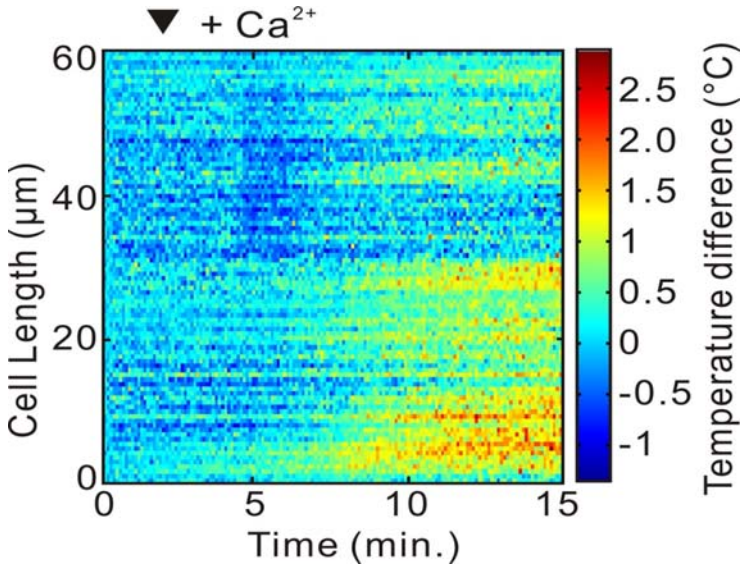

Figure 4.6 The intracellular temperature profile of the cell as function of time recorded under calcium influx. Ionomycin was added to reach 1 μM at the moment as the arrowhead indicated.

The statistical analysis of the observations was examined by repeating the same experiment over 38 cells, with different batches of cells. Figure 4.7 displays the relative temperature changes of all 38 cells as function of time with calcium influx at 2 minutes into the experiments. With some time delay after the calcium influx, temperature elevated about 1 to 2^{o}C over time in most of cells. Figure 4.8 shows the average temperature changes and standard deviation of 38 living cells in calcium influx experiments. The average temperatures of each individual cell were used to construct the color-coded histogram of the cellular temperature behavior over time. The result is plotted in Figure 4.9a and shows that on average the temperature is higher after the calcium influx. Among these cells, more than 20 cells whose temperature had one degree Celsius higher than the initial temperature are counted in our procedure (Figure 4.9b). This discrepancy is possibly due to the combination of heterogeneous of the cells, probing different compartments of the cells, and the limited temperature resolution on the measurement scheme.

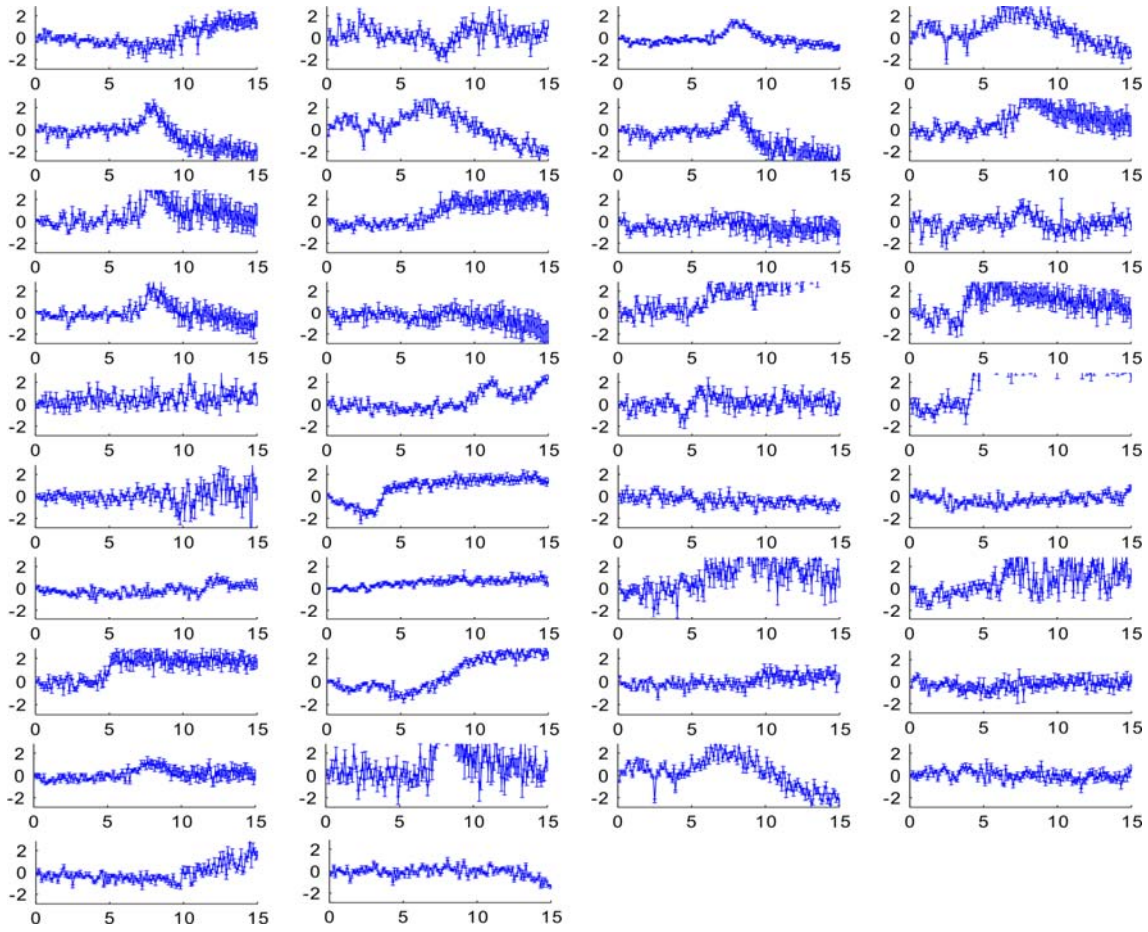

Figure 4.7 Relative temperature changes of all 38 cells as function of time with calcium influx at 2 minutes into the experiments.

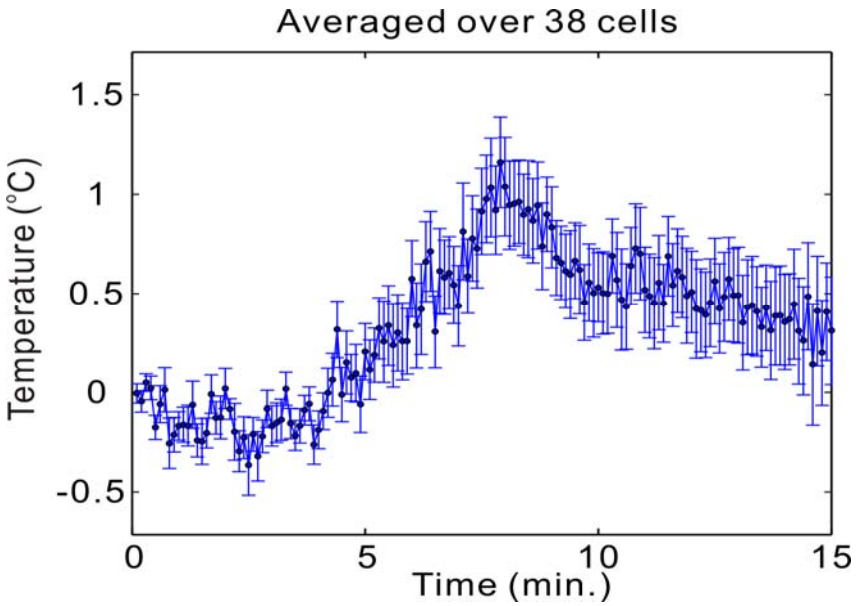

Figure 4.8 Average temperature changes (black dots) and standard deviation (extended blue lines) of 38 living cells in calcium influx experiments.

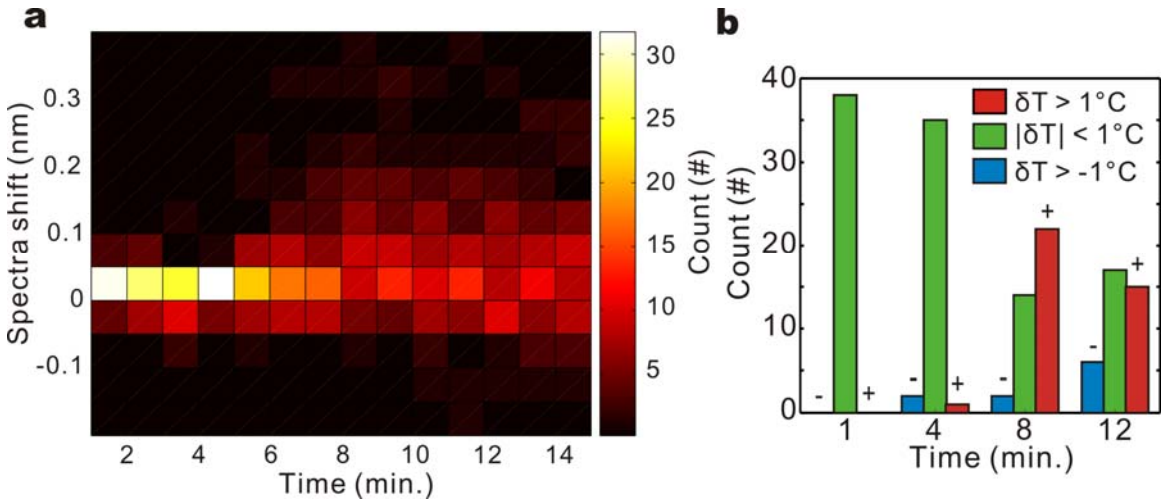

Figure 4.9 a. The color-coded histogram of average spectra shifts of 38 living cells. **b.** Cell counting of increasing and decreasing one degree Celsius shown in red and blue, respectively, after calcium influx over time.

4.3.6 Summary

Cellular temperature elevated about 1 to 2^{o}C after high calcium influx, and the results can be repeated in different batches of cells. This observation indicated that heat generated in living NIH/3T3 cells can be significant and measureable with calcium stimulants.

4.4 Cellular Temperature Responses to Temperature Stress

We hypothesized that the intricate biochemical reaction inside living cells will produce heat while dead cells won't such that cold shock could be an external stimulus to differentiate heat generation in live and dead cells. The intracellular temperature readouts, both before and after cold shock of live and dead cells will be calibrated against extracellular quantum dots immobilized on the surface. Those extracellular quantum dots will serve as temperature references and position references for potential mechanical drift of cells and QDs during long-term studies.

4.4.1 Experimental Setup

The experimental configuration is the same as the ones described in chapter 4.3. The temperature control unit was added to the experimental setup to regulate the temperature of Petri dish from 10 to 60^{o}C. A thermocouple was placed inside the Petri dish to monitor temperature changes and used as feedback to the controller.

4.4.2 Experimental Procedure

In a typical experiment, the quantum dots are introduced inside NIH/3T3 cells using the Qtracker Cell Labeling Kits (Q25021MP, Invitrogen). NIH/3T3 cells were placed in the Petri dishes with collagen / quantum dots layer to allow intake of QDs for 8 hours before imaging. To locate intracellular QDs, the grating of the spectrograph was set at the zero-th order for imaging. Once a suitable cell and quantum dot spot was located, the grating was switched to the first order mode for time-dependent spectroscopic investigations. The spectral images were collected with integration time ranging from 30-100 ms using WinView32 (Roper Scientific) and analyzed using MATLAB (Mathworks, Natick, MA). The experimental protocol is detailed as follows:

a. Prepare the glass bottom Petri dish with collagen layer and quantum dots as detailed in chapter 3.3.
b. Seed NIH/3T3 cells to the Petri dish with a final density of 5,000 cells per dish.
c. Incubate at 37^{o}C, 5% CO_2 for 8 hours or overnight.
d. Rinse cells with 1x PBS once and add 500 μL complete growth media to Petri dish.
e. Transfer Petri dish to imaging station.
f. Place the sterilized thermocouple into Petri dish, and set the control temperature to 37^{o}C. Wait the temperature stable at 37^{o}C for 5 minutes.
g. Locate cells with QDs and position them at the center of the field of view.
h. Adjust the entrance slit of spectrograph to 100 μm and start recording the spectra for 15 minutes with 150 frames.
i. Start cooling the Petri dish by setting the temperature to 15^{o}C on the temperature controller. In the heating experiment, set the temperature to 60^{o}C.
j. Complete the imaging recording.
k. Fix the cells with 3.7% formaldehyde in PBS at 37^{o}C for 10-15 minutes.
l. Rinse cells with 1x PBS three times.

m. Repeat steps f-j for dead cells experiment.

4.4.3 Heat Shock as the Control Experiment

Since there is no known active mechanisms that will allow a living cell to dissipate excessive heat, one should expect that the temperature-time responses inside a living cell will follow the environmental changes. This is a control experiment for the cold-shock test. Figure 4.10 displays the representative results of the average temperature profile of a single living cell under heat shock from 35-50^{o}C in 4 mins. The red dots are from experimental data of temperatures inside a living cell. The black curve is from the mean temperature of the quantum dot layer outside the living cell. Results show that intracellular temperature does follow that of a cell's immediate environment upon heat shock.

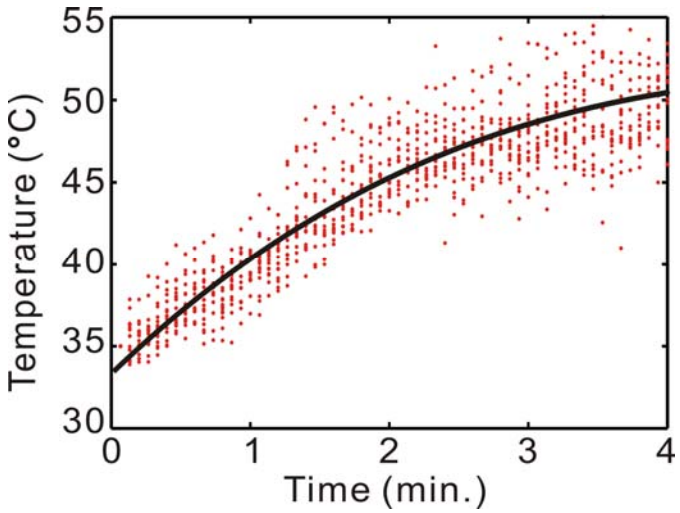

Figure 4.10 Temperature profiles of cells undergo heat shock from 35°C to 50°C. The red dots are represented the experimental data of temperature inside of cells, while the black solid line is the controlled temperature.

4.4.4 Cold Shock Experiments

In the cold-shock experiment, the temperature of the sample chamber was precipitously cooled from 37°C to 20°C and both intracellular and extracellular temperatures were recorded. The results are displayed in Figure 4.11, where red dots are from experimental data of intracellular temperatures and the black curve is from the mean temperature of extracellular QDs. It shows that living cells tended to maintain a temperature that is relatively higher than the environmental temperature during cold shock. The observation was in sharp contrast with that from heat shock shown in Figure 4.10. This implies possible heat generation in cytoplasmic region during cold exposure as a self-defense mechanism by living NIH/3T3 fibroblast cells. To verify that heat generation was a characteristic of living cells, presumably resulting from the complicated biochemical reaction networks, cold shock experiments were carried out on dead cells for comparison. Figure 4.12a and 4.12b show the temperature map of the exactly the same cell both in the living and dead states as a function of position and time, respectively. The y-axis represents the position of the cell and color of pixels indicates the relative temperature changes.

Results revealed that living cells showed a measureable local temperature rise while temperature inside the dead cells relatively followed the environmental temperature changes as the dead cell is incapable of adapting to sudden environmental changes.

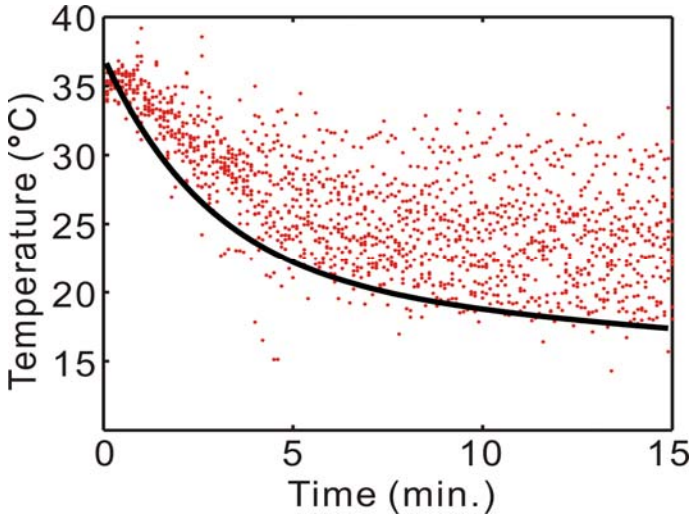

Figure 4.11 Temperature profiles of cells undergo cold shock from 37°C to 20°C. The red dots are represented the experimental data of temperature inside of cells, while the black solid line is the controlled temperature.

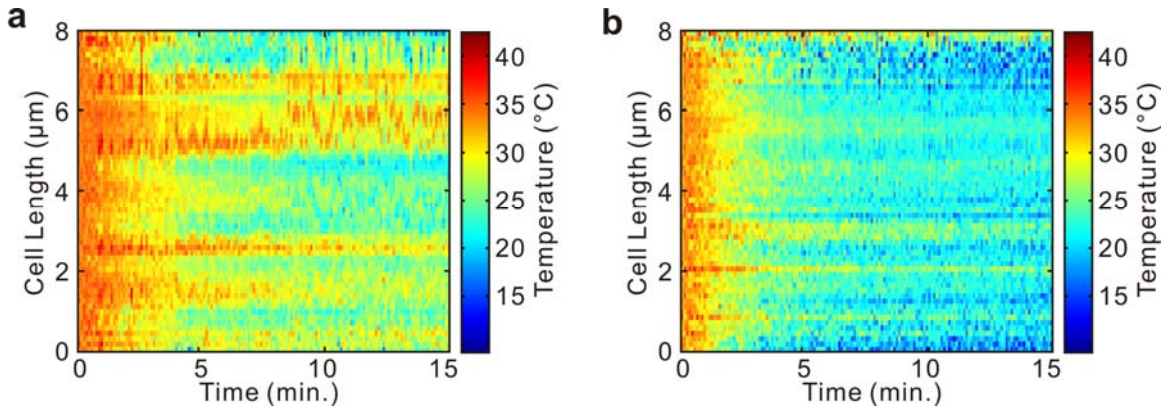

Figure 4.12 a. Temperature profile along the cell length as a function of time following cold shock cooling the sample chamber temperature from 37 to 20°C. **b.** The temperature profile of single dead cell recorded under the same cold exposure.

The statistical significance of the observation was examined by repeating the same experiment over 27 cells. The results are displayed in Figure 4.13a, where red and blue lines are the average temperature of living cells and dead cells, respectively, while the dashed line is the average of the extracellular reference temperature. It shows that on average the cellular temperature was higher than the environment. After 10 minutes into the cold-shock experiments, the average temperature of 27 live cells was about 2.5^{o}C higher than that of the environment and the calculated 95% confidence interval based on normal distribution was 1.5~3.4^{o}C. The same

cold-shock experiments on dead cells show their temperatures were close to the environmental temperature within the ±0.5°C margin. In addition, average temperature of all 27 living cells had larger standard deviations from 0.5 to 2°C during the cold-shock test, as shown in Figure 4.13b. Figure 4.13c and 4.13d show the color-coded histograms of average temperature of individual living and dead cells, respectively, as a function of time following cold shock. It is conspicuous that temperature distribution of live cells were more scattered at higher temperature region. The dead cells exhibit a temperature decay profile more or less following the same trend as the extracellular environment. Figure 4.14 shows the temperature responses of the selected 25 cells, both live and dead together, as function of position and time under cold shock procedure. Living cells consistently exhibited a higher temperature during cold shock experiments, and dead cell experiments were shown as controls.

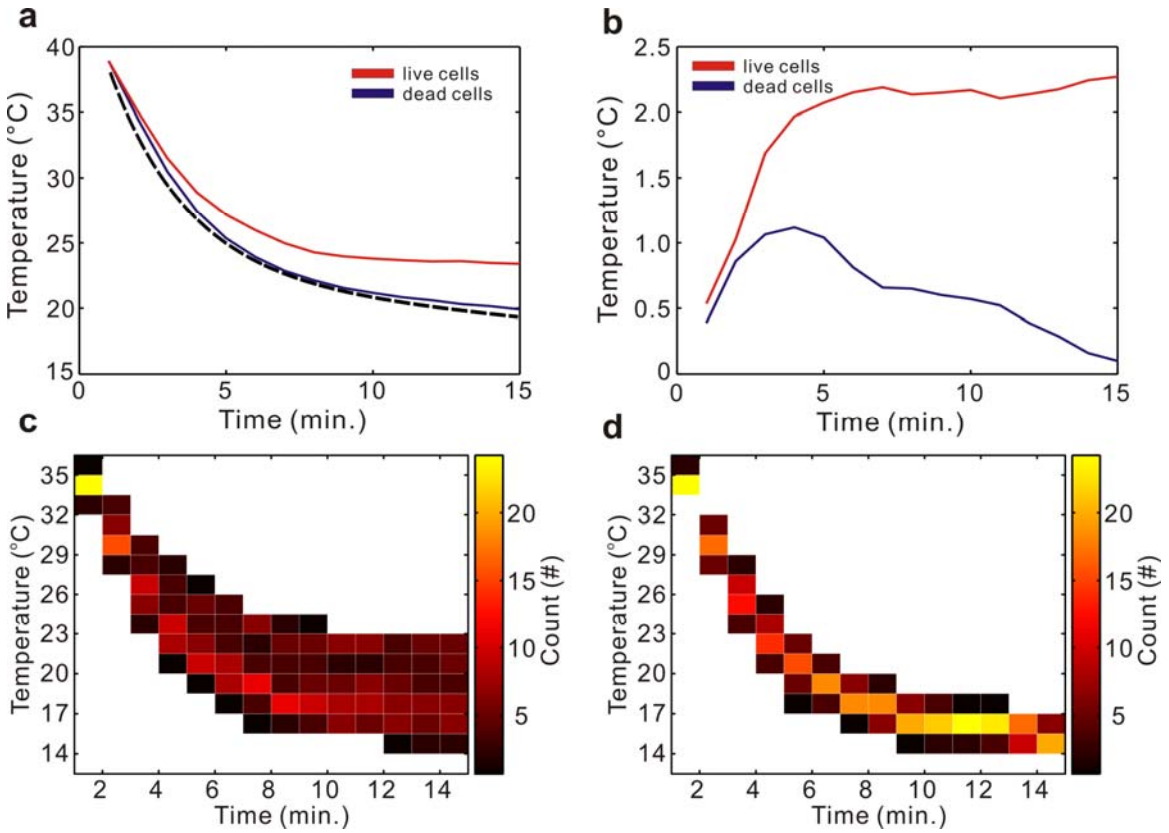

Figure 4.13 a. The average temperature over 27 cells in our cold shock experiments. Red line indicates the living cells while blue line indicates the dead cells. The dashed line is the controlled environmental temperature. **b.** The standard deviation of the temperature distribution over 27 cells over time. **c.** The color-coded histogram of the average temperature of 27 single living cells recorded under cold shock. **d.** The color-coded histogram of the average temperature of 27 dead cells (same cells as those in Figure 4.13c after they were fixed) under cold shock.

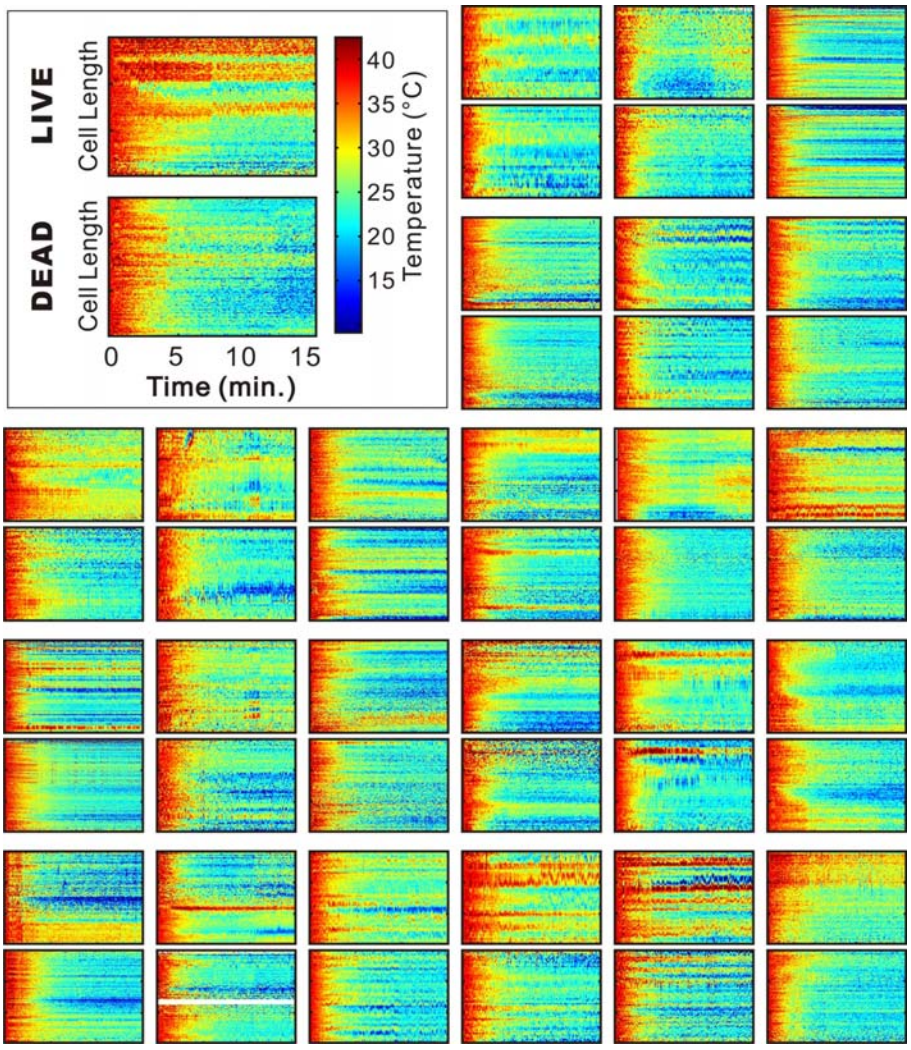

Figure 4.14 The selected temperature maps of 25single cell in cold exposure experiments. The data show in both live and dead temperature maps of cells.

4.4.5 Intracellular Temperature Distribution

The data shown in Figure 4.12 and 4.14 display several hot spots in red and yellow within a single living cell a few minutes into the cold shock experiment and the temperature profile across a single cell became non-uniform. This suggests that the intracellular temperature difference can exist within a single living cells and the temperature distribution can have wider ranges as compared with that of dead cells. This observation was highlighted by focusing on the temperature difference on the QDs temperature measurements during cold shock. Figure 4.15a and 4.15b shows the color-coded histogram of intracellular temperature differences of live and dead cells under cold shock, respectively. The figures were generated by plotting the histogram of maximum temperature differences with 1 degree interval for 27 cells for every minute. The average temperature differences within live cells were recorded about 6^{o}C after 10 minutes into the cold shock experiment. The observed hot spots and intracellular temperature differences

illustrate the feasibility of using QDs as local temperature sensors with submicron spatial resolution.

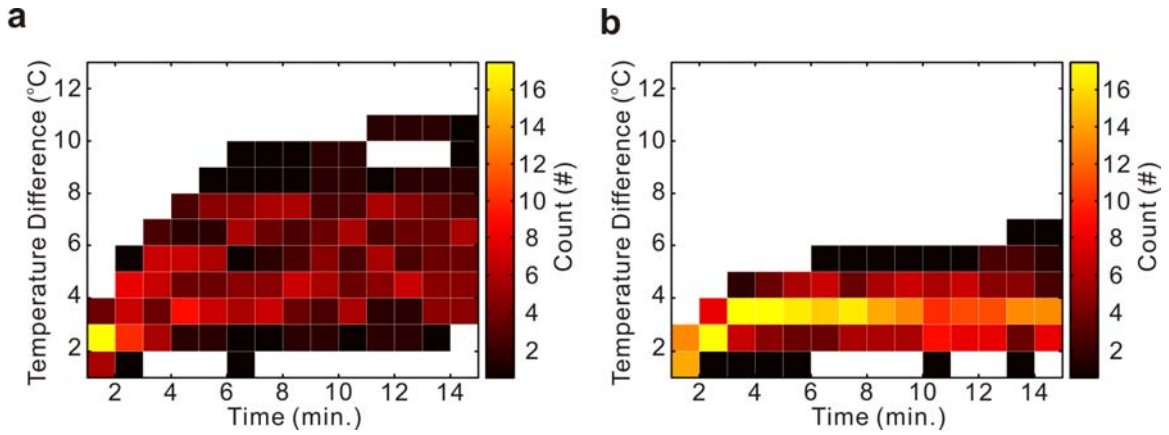

Figure 4.15 a. The color-coded histogram of intracellular temperature difference of 27 living cells under cold shock. **b.** The color-coded histogram of intracellular temperature difference of 27 dead cells under cold shock.

These observations reveals the possibility of heat-generating "hot spots" inside living cells at which the biochemical processes are dominated by exothermic reactions. If an endocytosed quantum dot cluster is in close proximity to such a hot spot, then the quantum dots will be able to sense the excess thermal energy production before the heat is dissipated at locations away from the hot spot. In a rested living cell under physiologic conditions, we do not expect to observer great temperature differences within the cell because we anticipate the intracellular temperature gradient to reach steady-state equilibrium. When the cell is subjected to cold shock, the thermal and biochemical steady state is severely perturbed. Biochemically, such a cold-shock perturbation will shift chemical equilibrium to increase the reaction rate of heat-producing reactions. Hot spots contain more exothermic reactions and their local temperature will decrease slower as compared to the temperature of the cell's environment.

4.4.6 Viability Study

We have extensively studied the cellular behavior under cold exposure. The determination of cell viability is important to show that cells are alive during our cold shock procedure. Separate control experiments have been conducted to examine the cell viability after 10-20 minutes of cold exposure. After the cold shock test, cell layer was dispersed by 0.25% trypsin - 0.53 mM EDTA solution. The cell suspension was then stained by 0.4% trypan blue for 5 minutes at room temperature. The number of viable cells and dead cells was counted under Hemocytometer. The viability of the NIH/3T3 cells was slightly decreased when cells were exposed to cold environment for a longer time, as shown in Figure 4.16. About 80% of cells were alive after 20 minutes of cold shock.

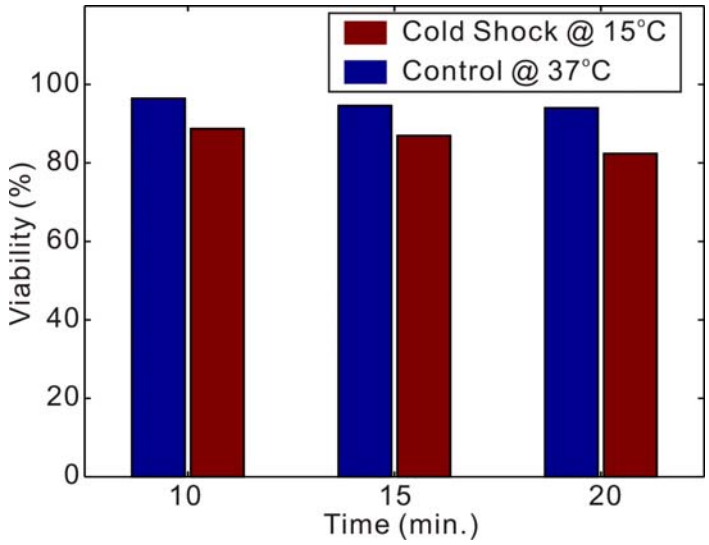

Figure 4.16 Viability study of the NIH/3T3 cells under different period of cold exposure at 15°C.

4.4.7 Theoretical Modeling

The thermal diffusivity D [m^2s^{-1}] was calculated through the cytoplasm of the cell using $D = k/\rho C_p$, where k is thermal conductivity [W $m^{-1}K^{-1}$], ρ is density [kg m^{-3}], and C_p is specific heat [J $kg^{-1}K^{-1}$]. The cytoplasm was approximated by water, where k = 0.58 J $m^{-1}s^{-1}K^{-1}$, ρ = 1000 kg m^{-3}, and C_p = 4.2 kJ $kg^{-1}K^{-1}$. The thermal diffusivity through the cell was calculated to be 1.38×10^{-7} m^2s^{-1}. The time t [s] of heat transport was formulated by $t = x^2 / 2D$, where x [m] is heat transported distance between two spots. In a single cell, the time for heat transfer across the cell was calculated to be 3 ms, assuming the length of the cell is 30 μm. This indicated that any temperature differences should reach the equilibrium state within three millisecond inside the cell in pure heat conduction event. If living cells response and actively generate heat during the experiments, the measured temperature profile can be represented as the quasi-steady state temperature.

To further verify the temperature differences across the cell were not coming from the thickness difference of the cell, we have preformed computational modeling for our system with finite element software (COMSOL Multiphysics). In the cooling experiment, the solution has little convection since the warmer solution was remained on top of the Petri dish. Therefore, only heat conduction is considered in the system. The simulation model has included the glass bottom Petri dish, culture media, one cell, and surrounding air (Figure 4.17a,b). The material and thermal properties of the cell and culture media were approximated as water. Figure 4.17c shows the cooling profiles of the model at two points, at the top of the cell and at the bottom of the cell, separated by ten micrometers. The profiles show that two points almost have exactly the same temperature during the cooling process. This indicated that the temperature we have measured were not cause by the thickness difference, and should be coming from the adaptive thermogenesis of the cell.

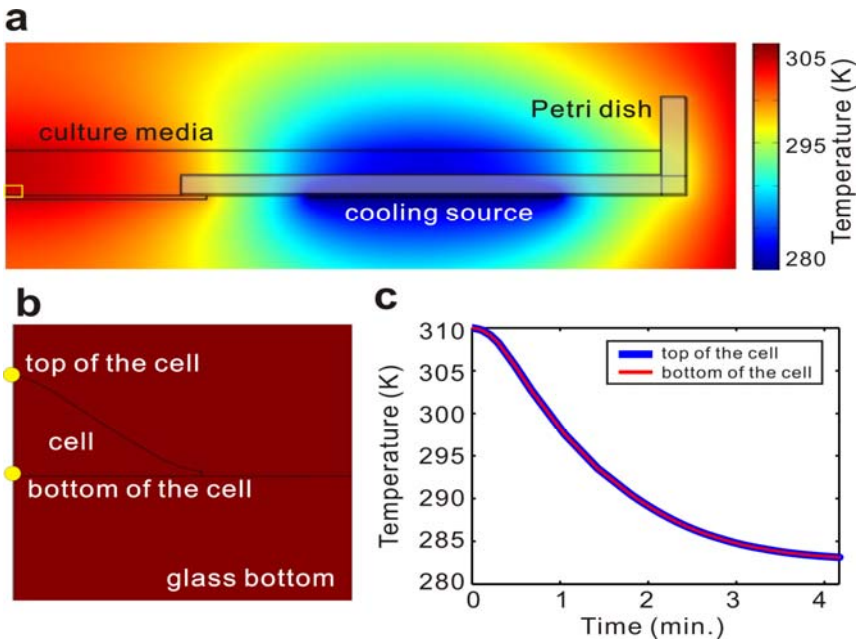

Figure 4.17 COMSOL multiphysics simulation of the system under cooling process. **a.** The temperature profile of the whole system with one cell, culture media, and Petri dish. **b.** The blow up of the cell in **a.** **c.** The simulated cooling profile of two different locations of the cell.

During the cooling process, we have observed that the cells exhibited 4 to 8 degrees temperature differences within the single cells. In order to maintain this temperature difference continuously, cells must actively generate heat. The required heat generation rate $\dot{q}$ [w] was calculated by a simplified one-dimension heat conduction model $\dot{q} = -\left(kA\frac{\partial T}{\partial x}\right)$, where k is thermal conductivity [W $m^{-1}K^{-1}$], A is the cross-sectional surface area of heat conduction [m^2], and T is temperature [K]. The cytoplasm was approximated by water, where k = 0.58 $Jm^{-1}s^{-1}K^{-1}$, and the size of the cell is about 30μm, and thus A = 7×10^{-10} m^2. The required heat generation was calculated to be about 10 μW. In a finite element model, the required heat source to maintain this temperature separation was obtained as 1-10 μW in the simulated microenvironment.

4.4.8 Summary

Our results present the usage of quantum dot-based temperature tracking is an effective way to measure temperature at selected domains inside single cells. The experiments show that at the single cell level, cells showed a temperature that is relatively higher than its environmental temperature during cold shock. It indicated that cells can counteract the sub-physiological temperature by locally heating up subcellular compartments, and consequently have hot spots in those compartments and result a higher cellular temperature in average. The experiments were repeated for 27 cells and the results were consistent. A theoretical model showed that the temperature difference between cells and environment does not come from the heat variations due to the thickness of the cell, since the time constant of the thermal diffusion events are in micro-second scale. Moreover, the experiment results implied possible heat generation during

cold exposure, presumably resulting from the complicated biochemical reaction networks, as a self-defense mechanism by living NIH/3T3 fibroblast cells.

4.5 2D Thermal Imaging by Scanning Confocal Microscopy

In the previous experiments, a home-built imaging / spectroscopy microscope was used to characterize the emission spectra of QDs. The setup was limited in imaging a strip of cells by the entrance slit of the spectrograph. Therefore the collected data have only one dimensional spatial information verse temperature. For two dimensional thermal imaging of single cells, scanning confocal microscopy has been explored and discussed in this section.

4.5.1 Concept of 2D Scanning Thermal Imaging

Scanning confocal microscopy represents one of the most significant advances in optical microscopy. The technique enables deep visualization in live and fixed cells and tissues and is capable of collecting sharply defined optical sections from which three-dimensional renderings can be created. Confocal microscopy offers several advantages over conventional wide field optical microscopy, including the ability to control the depth of field and eliminate or reduce the background noise. They also have the capability to collect serial optical sections from thick specimens. The basic key to the confocal approach is the use of spatial filtering techniques, point illumination and a pinhole in an optically conjugate plane in front of the detector, to eliminate out-of-focus light or glare in specimens whose thickness exceeds the immediate plane of focus. As results, only light produced by fluorescence very close to the focal plane can be detected. By scanning through the whole specimens, one can recreate the 2D or 3D images with high spatial resolution.

Examination of the spectra information of the QDs via scanning confocal microscope can be accomplished by comparing the emission intensity of two channels. The idea is to use a dichroic mirror that separates the red and blue components of quantum dot emission during confocal scanning imaging (Figure 4.18). In this configuration, the total intensity was calculated by considering the photons from two detectors, and the spectral fluctuations can be defined as

$$\chi_{spec.} = \frac{I_b - I_r}{I_b + I_r} \qquad \text{Euqation 4.1}$$

where I_b and I_r the emission intensities recorded from detector B and detector R, respectively. Therefore, $\chi_{spec} < 0$ for red-shifted emission and $\chi_{spec} > 0$ for blue shifted emission. This approach has been found to be extremely sensitive to emission frequency shift in spectral fluctuations from individual quantum dots [130] and single gold nanoparticles [131].

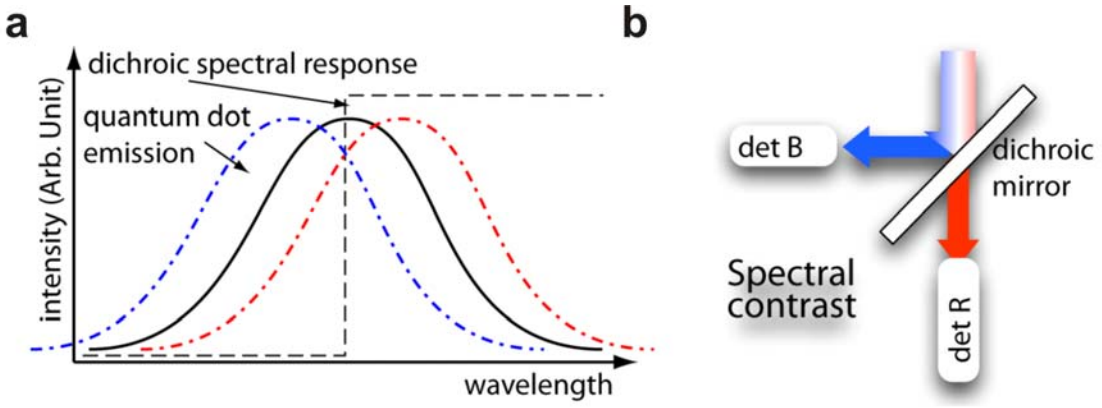

Figure 4.18 a. Conceptual illustration of two-channel detection of spectral shift. **b.** Detector configuration.

4.5.2 Two Dimensional Thermal Imaging

A Zeiss confocal microscope (LSM-700) was used to carry out the 2D thermal imaging experiments. It equipped a variable dichroic beamsplitter, which can manually adjust the dichroic cut-off frequency. The cut-off frequency was set to the average peak wavelength of the quantum dots, which is 653 nm. The optical path is illustrated in Figure 4.19.

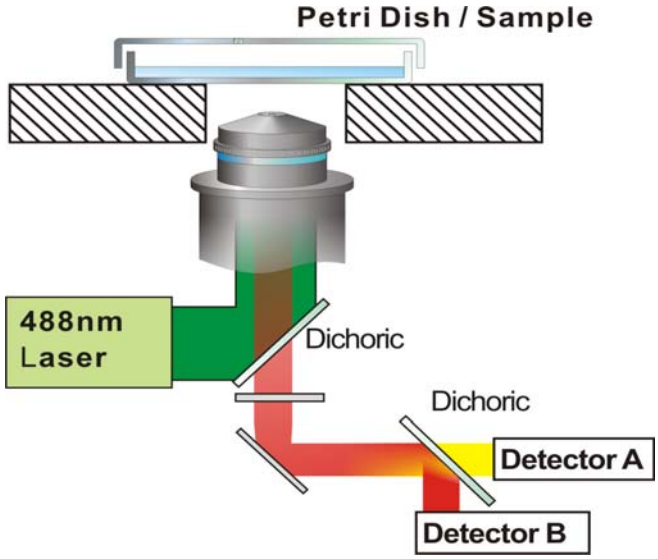

Figure 4.19 The optical setup of the cellular temperature measurement via spectral shift of quantum dots, with two detectors to resolve spectral fluctuations.

The calcium flux experiments as described previously were reproduced and imaged by confocal microscope to generate the 2D temperature map of the single cell. The experimental procedure is similar. Cells were incubated in the glass bottom Petri dish at room temperature and placed at confocal imaging station. Both red and blue channels which bisected by variable dichroic beamsplitter were recorded. After 2 minutes into the experiments, ionomycin (10 µL of

0.5 mM solution) was added to the culture dish, containing 500 μL of the medium, to the final concentration 1 μM. The emission intensities from both channels were used to calculate the spectra fluctuations and the corresponding temperature variations. Figure 4.19 shows the reconstructed time lapse thermal images of NIH/3T3 cells under the Ca^{2+} stress. Local temperature was increased during the experiments at several regions indicated by arrow heads. The results show the spectra information can be characterized by scanning confocal imaging and spectra dichroism. Therefore, two-dimensional temperature maps can be realized. Furthermore, the confocal images are much cleaner since they only image in a focal plan of about 100 nm in thickness. Therefore, high spatial resolution of thermal images can be generated. Three-dimensional temperature measurement can be achieved if one incorporates with vertical stacks scanning.

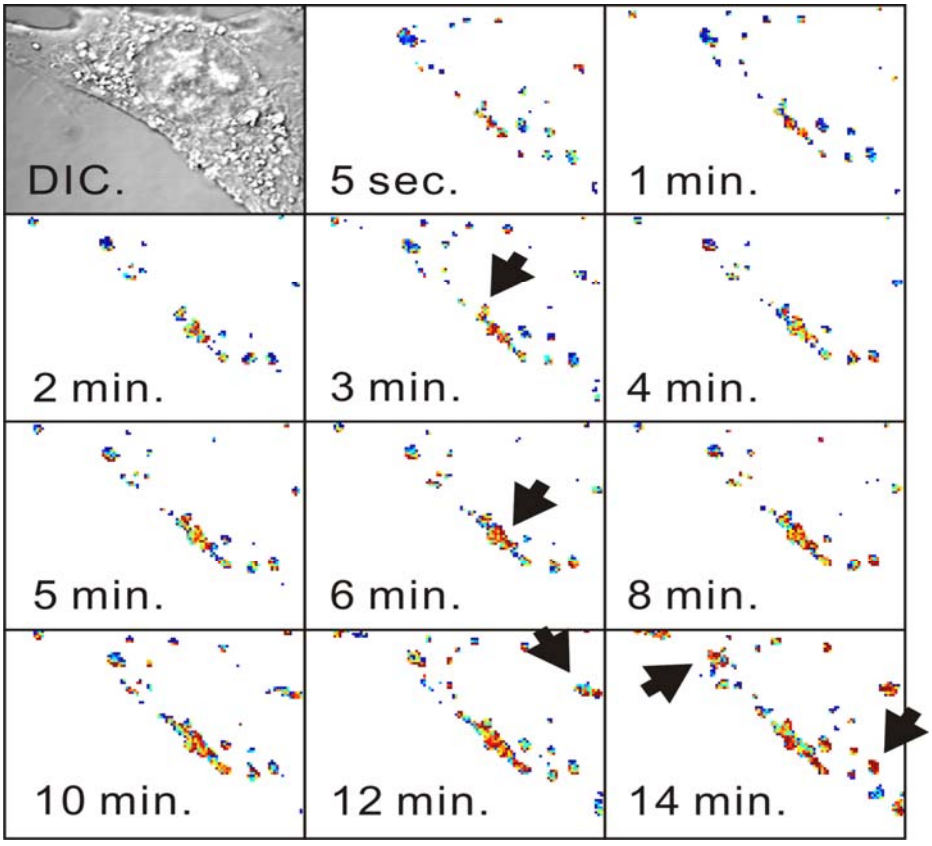

Figure 4.20 Time lapse thermal images of NIH/3T3 cells under Ca^{2+} stress. Arrow heads indicate the spots with temperature increase.

4.6 Summary

NIH/3T3 cells showed measureable temperature increase with respect to influx of high concentration calcium solution. A cold-shock assay was conducted in a 15-min experiment, whereby the ambient temperature of cell culture was precipitously lowered from 37 to 20°C. We found that single living cells exhibited higher average temperature than the environmental stimulations during cold-shock experiment. This implies possible heat generation during cold exposure, presumably resulting from the complicated biochemical reaction, as a self-defense

mechanism by living NIH/3T3 fibroblast cells. Moreover, the observations of temperature distribution were in sharp contrast between live and dead cells, in both calcium influx and cold shock experiments. A negative control experiment using heat-shock was performed and results showed the temperature of NIH/3T3 fibroblasts followed closely with the external environmental temperature in a heating process from 35 to 50^{o}C. In these experiments, intracellular temperature differences have been observed and recorded as large as 5^{o}C during cold shock experiments. This observation also indicated that heat production within sub-compartments of single cells. Additionally, the observed hot spots inside living cells illustrate the feasibility of using QDs as local temperature sensors with submicron spatial resolution (800 nm per pixel with 20x objective).

Chapter 5
Conclusion and Future Works

5.1 Dissertation Summary

In this dissertation, a far field, non-invasive temperature measurement technique with potential nanoscale spatial resolution has been presented. The semiconductor nanocrystalline particles, or quantum dots, were introduced and used for temperature measurements. Experiments have been developed to investigate the emission spectra of single CdSe/ZnS core shell QDs as a function of environmental temperature. It was found that the peak wavelength of a single QD exhibited a red-shift to longer wavelengths as the temperature increases. The spectral shift of a single quantum dot was characterized as 0.1 nm/°C around room-temperature range. Furthermore, the emission intensities of single quantum dots decrease as the temperature increases.

A proof-of-concept experiment has been performed to demonstrate the practical usage of quantum dots as temperature markers. A fabricated micro-heater was used to create a temperature distribution across a length of 1200 μm. The temperature profile of the heater can be controlled and manipulated by the input power and were successfully reconstructed using emission spectral shift of quantum dots, with a 1°C temperature resolution and a 267-nm spatial resolution which is limited by the optical setup. A theoretical model has been derived and used to describe the temperature profiles, mathematically. Both experimental and simulation results show good consistency. Thus, this technique has the potential to be applied to noncontact micro/nano temperature measurements with sub-micron spatial resolution.

Experiments have been design to internalize QDs into NIH/3T3 cells. QDs with bio-compatible coating were delivered into cytoplasm of living cells by endocytosis. The internalized QDs distributed across the cytoplasm region with no specific target sites. The viability study showed that the internalized QDs didn't affect cell culture. A collagen layer with fixed QDs was left at the surface of the culture dish to sever as an in-situ temperature reference. The temperature-dependent spectra characteristics of internalized QDs were characterized from 17-47^{o}C, with 5^{o}C increments, and the emission peak-wavelength with respect to temperature was approximated as linear with a slope of 0.06 nm/°C. A control experiment has been performed to explore the spectral shift due to intracellular pH changes. The results showed that across a range of 5 pH scales from 4-10, the peak wavelength changes about 0.029 nm per 1 pH value changes. This demonstrated that the spectral shift of QDs were not greatly affected by the pH shift, and could be used as the temperature indicator.

Two experiments have been designed to explore the possible applications on cellular temperature measurements. The first approach is to induce the thermogenesis of single living cells with the infusion of calcium ions. NIH/3T3 cells showed a measureable temperature rise with respect to high extracellular calcium concentration. Live cells exhibited about 1^{o}C temperature increase after calcium influx, comparing with no temperature changes in dead cells. The results of dead cell experiments also showed that the emission spectra of QDs are not affect by ion concentrations. In the second experiments, a cold-shock assay was conducted in a 15-minute experiment, whereby the ambient temperature of cell culture was precipitously lowered

from 37 to 20^{o}C. Single living cells exhibited a higher average temperature than the environment temperature during the cold-shock experiment. The control experiments on dead cells showed temperatures inside deal cells were following the environmental temperatures. These suggest that heat generation was a characteristic of living cells. A negative control experiment using heat-shock was performed and results showed the temperature of NIH/3T3 fibroblasts trace closely with the external environmental temperature in a heating process from 35 to 50^{o}C. This is predictable as there are no known active mechanisms that allow a cell to dissipate excessive heat rapidly.

Furthermore, thermal imaging within living cells, in both calcium influx and cold shock experiments, exhibited clearly temperature gradients. The thermal image showed several hot spots within a single living cell a few minutes into the experiment and the temperature profile across a single cell became non-uniform. These hot spots implied that some cellular compartments c contain more exothermic reactions than others when the cell was subject to external stresses. The observed hot spots inside living cells illustrate that QDs were able to sense the excess local thermal energy production before the heat dissipations.

These experiments suggest that QDs could be widely used as temperature markers to study thermodynamic aspect of cell and biological systems. Thermoregulation is a complicated process and is needed to elucidate their physiological functions. Being able to follow intracellular temperature in living cells for a prolonged period of time could allow researchers to start studying how single cells regulate their temperature.

5.2 Future Directions

Quantum dots as temperature markers have been demonstrated in MEMS micro-heater and cellular environments. Further improvement could include higher signal-to-noise ratio and better temperature resolution, including applications in MEMS and thermodynamic cellular studies.

5.2.1 Optical System Improvement

The current measurement setup has suffered a major problem in low temperature resolution of 1^{o}C, due to the drift of QDs. The movements of the QDs at the imaging surface were caused by combination of the optical stage movements, the migration of living cells, and the movements of quantum dots-vesicles inside the cells. These slight movements result in a spectra shift dispersed by the spectrograph and reduce the temperature resolution. To resolve the drifting problem, a second imaging device should be added into the optical system, and collect the wide field images of the samples simultaneously. With the position information from the second camera, the spectra information can be calibrated with respect to location changes. However, the emission intensity imaged in the spectral camera will be reduced because of the additional optical path for the second camera. Alternative, the quantum-dot spectral shift can be resolved by two spectrally filtered channels, with a dichroic mirror which separates the red and blue components of the emission. In this approach, it requires two detectors but the emission intensities are not wasted since both images are used to produce spectral information.

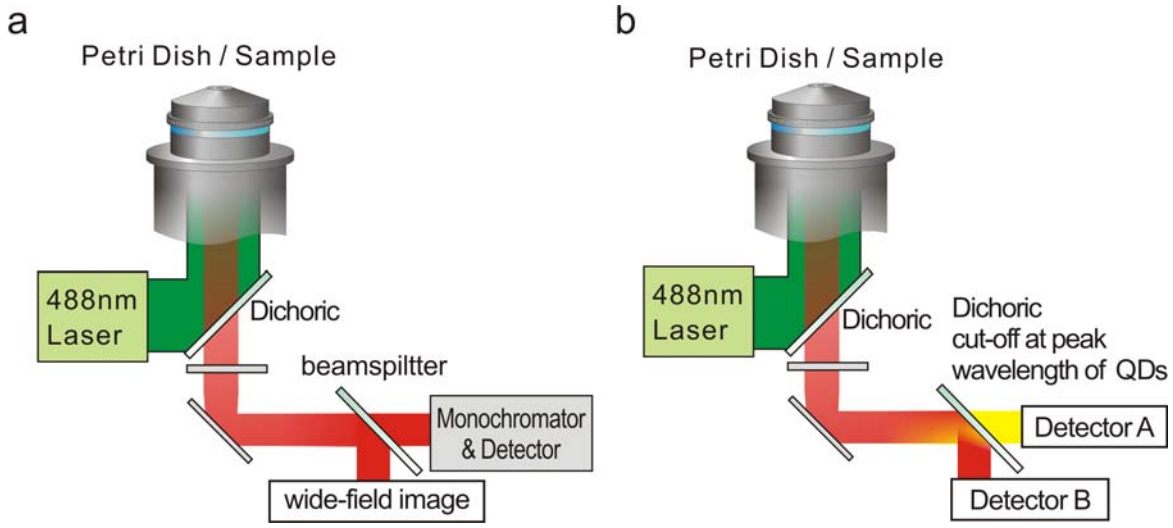

Figure 5.1 Schematic drawing of optical system improvement. **a.** A second detector is added to the optical path to record the position information. **b.** A dichoric with cut-off wavelength at peak wavelength of QDs is used to separate the red and blue components of the emission.

5.2.2 Multicolor Labeling for Temperature Resolution Improvement

In the dissertation, spectral shift of QDs with respect to changes of pH level has been explored and characterized as 0.029 nm shift per 1 pH value changes. Although the influence of pH changes is small comparing to temperature changes, it should not be ignored when a precise temperature measurement is needed. However, *in-situ* pH measurement at small scale is also difficult. With multicolor labeling of QDs, more than one environmental factor can be monitored simultaneously. QDs with different color or materials would have different spectra-environmental factors relationships. For example, with two color labeling and two spectral shift data, one can extract two environmental factors, such as temperature and pH level, as illustrated in Figure 5.2. By this, temperature resolution via QDs spectral shift can be improved.

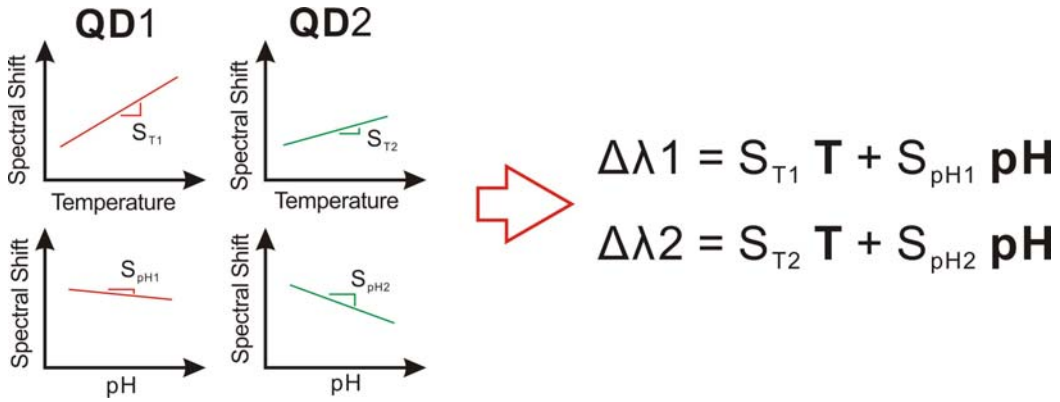

Figure 5.2 Illustration of using multicolor QDs to resolve multiple environmental factors.

5.2.3 Microfluidics Device Integration

A microfluidics device with multiple cell culture chambers is useful for culturing different cell lines or different stress conditions to observe multiple behaviors at the same time. For example, one chamber can be used as control samples, such as QDs or dead cells with QDs, while the other can be used to investigate the behaviors of living cells under various stresses. This way, both control and live samples are studied at the same chip at the same time, which can minimize the influence by running the experiments separately. Furthermore, a micro-heat can be fabricated and integrated with microfluidics devices. The integrated device can provide a precise temperature control at small scale as well as faster temperature responses. Electrical stimulation would also be accessible as long as a pair of electrodes is added on the device.

5.2.4 NEMS/MEMS Application

The applications of this technique in MEMS research area are abundant. For example, microchips are compact and embedded with billions of transistors, which can produce large amount of heat when fully loaded. Investigating the localized heat spot with high spatial resolution thermal images can study the heat sources and advance the heat dissipation processes. These studies have the potential to improve the architecture of the microchips.

Moreover, QDs could be used for the measurements of the heat dissipation of high frequency resonator in MEMS devices, such as accelerometers, gyroscopes, and filters, to name a few. The temperature rise in the resonators are caused by lattice vibration and interaction with surrounding substance, and can result in frequency shift, material fatigues, high background noise, and so on. With the ability to characterize device operation temperature, researchers can incorporate the information into design consideration, and therefore, increase the device performance, reliability and life-time.

Last but not the least, QDs can be used to probe the thermal properties of nanostructures, such as nano-wires and carbon-nano-tubes, to name a few. These advanced nanostructures have unusual material properties to be characterized. Micro- to nanoscale temperature measurement technique is an important tool to characterize the performance of microchips, MEMS and NEMS devices.

5.2.5 Cellular Studies in Thermodynamic Aspects

The application of this technique in biological system can have a great impact in fundamental cell biology and molecular cell biology. It is important to address the temperature aspect of living single cells, using QDs as nanoscale temperature sensors to study and follow local heat production. QDs should be delivered into specific compartments of the cell to address their temperature variations individually. Practically, mitochondrion is the primary energy production organelle in a cell. It plays a major role in caloric management and has been implied in regulating cellular networks controlling such important processes as ageing and apoptosis. Evidences have suggested that the number, distribution, and morphology of mitochondria are dynamic and strongly correlated with cellular state and the variations in mitochondrial temperature are an important parameter for mitochondrial physiology. QDs could be applied in these studies to investigate temperature changes of individual mitochondria in living cells.

Methods of targeting quantum dots to nucleus and mitochondria have been reported previously. Briefly, the Mito-8 mitochondrion-targeting signal sequence (NH_2-MSVLTPL-

LLRGLTGSARRLPVPRAKIHWLC-COOH) can be synthesized chemically and used to deliver quantum dots, or nanoparticles, to mitochondria. The N terminus will be tagged with a biotin moiety for coupling with the streptavidin coating on QDs. These peptide-quantum dots have the ability to translocate itself across the plasma membrane to the specific targets, i.e. mitochondria. With these approaches, the cellular temperature at specific organelles can be determined, potentially, with multi-color labeling via QDs to various compartments.

QDs-based temperature tracking method developed in this dissertation is directly transferrable to other cell types. This technique could afford important examinations of common assumptions in the design and interpretation of *in-vitro* experiments - temperature is constant inside a living cell. For instance, thermoregulation is a complicated process. Being able to follow intracellular temperature and mitochondrial temperature in living cells for a prolonged period of time could allow us to start asking the question if and how single cells regulate their temperature. Many other possibilities can be envisioned. For example, disease-presenting cells may have different intracellular temperature profile compared to healthy cells. If true, a new approach of differentiating normal and unhealthy/cancer cells could be investigated. The natural extension along this line of research could be new avenues for designing temperature-specific drug delivery (or release) strategies.

Bibliography

[1] A. J. DeMello, "Microfluidics - DNA amplification moves on," *Nature*, vol. 422, pp. 28-29, 2003.

[2] E. M. Lucchetta, J. H. Lee, L. A. Fu, N. H. Patel, and R. F. Ismagilov, "Dynamics of Drosophila embryonic patterning network perturbed in space and time using microfluidics," *Nature*, vol. 434, pp. 1134-1138, 2005.

[3] F. Hauet-Broere, L. Wieten, T. Guichelaar, S. Berlo, R. van der Zee, and W. Van Eden, "Heat shock proteins induce T cell regulation of chronic inflammation," *Annals of the Rheumatic Diseases*, vol. 65, pp. 65-68, 2006.

[4] K. C. Kregel, "Heat shock proteins: modifying factors in physiological stress responses and acquired thermotolerance," *Journal of Applied Physiology*, vol. 92, pp. 2177-2186, 2002.

[5] S. Xanthoudakis and D. W. Nicholson, "Heat-shock proteins as death determinants," *Nature Cell Biology*, vol. 2, pp. E163-E165, 2000.

[6] P. Lonnbro and I. Wadso, "Effect of Dimethyl-Sulfoxide and Some Antibiotics on Cultured Human T-Lymphoma Cells as Measured by Microcalorimetry," *Journal of Biochemical and Biophysical Methods*, vol. 22, pp. 331-336, 1991.

[7] J. K. Jaiswal, H. Mattoussi, J. M. Mauro, and S. M. Simon, "Long-term multiple color imaging of live cells using quantum dot bioconjugates," *Nature Biotechnology*, vol. 21, pp. 47-51, 2003.

[8] B. Q. Sun, Y. L. Xu, G. S. Yi, and D. P. Chen, "Photoluminescence properties of semiconductor nanocrystals and their applications in biological fluorescent probes," *Chinese Journal of Analytical Chemistry*, vol. 30, pp. 1130-1136, 2002.

[9] A. Hoshino, K. Fujioka, T. Oku, S. Nakamura, M. Suga, Y. Yamaguchi, K. Suzuki, M. Yasuhara, and K. Yamamoto, "Quantum dots targeted to the assigned organelle in living cells," *Microbiology and Immunology*, vol. 48, pp. 985-994, 2004.

[10] A. M. Derfus, W. C. W. Chan, and S. N. Bhatia, "Intracellular delivery of quantum dots for live cell labeling and organelle tracking," *Advanced Materials*, vol. 16, pp. 961, 2004.

[11] P. A. Kinzie, *Thermocouple Temperature Measurement*. New York: Wiley & Sons, 1973.

[12] P. R. N. Childs, J. R. Greenwood, and C. A. Long, "Review of temperature measurement," *Review of Scientific Instruments*, vol. 71, pp. 2959-2978, 2000.

[13] I. Wadso, "Microcalorimetric techniques for characterization of living cellular systems. Will there be any important practical applications?," *Thermochimica Acta*, vol. 269, pp. 337-350, 1995.

[14] Y. Wang and C. H. Chen, "Acetylcholine Receptor-Enriched Membrane-Vesicles in Response to Ethanol - Activity and Microcalorimetric Studies," *Biophysical Chemistry*, vol. 43, pp. 51-59, 1992.

[15] M. Monti, P. Hedner, J. Ikomikumm, and S. Valdemarsson, "Erythrocyte Thermogenesis in Hyperthyroid Patients - Microcalorimetric Investigation of Sodium-Potassium Pump and Cell-Metabolism," *Metabolism-Clinical and Experimental*, vol. 36, pp. 155-159, 1987.

[16] I. Tasaki, K. Kusano, and P. M. Byrne, "Rapid Mechanical and Thermal-Changes in the Garfish Olfactory Nerve Associated with a Propagated Impulse," *Biophysical Journal*, vol. 55, pp. 1033-1040, 1989.

[17] H. F. Arata, Y. Rondelez, H. Noji, and H. Fujita, "Temperature alternation by an on-chip microheater to reveal enzymatic activity of beta-galactosidase at high temperatures," *Analytical Chemistry*, vol. 77, pp. 4810-4814, 2005.

[18] T. M. Pearce, J. A. Wilson, S. G. Oakes, S. Y. Chiu, and J. C. Williams, "Integrated microelectrode array and microfluidics for temperature clamp of sensory neurons in culture," *Lab on a Chip*, vol. 5, pp. 97-101, 2005.

[19] T. Yamamoto, T. Nojima, and T. Fujii, "PDMS-glass hybrid microreactor array with embedded temperature control device. Application to cell-free protein synthesis," *Lab on a Chip*, vol. 2, pp. 197-202, 2002.

[20] J. Khandurina, T. E. McKnight, S. C. Jacobson, L. C. Waters, R. S. Foote, and J. M. Ramsey, "Integrated system for rapid PCR-based DNA analysis in microfluidic devices," *Analytical Chemistry*, vol. 72, pp. 2995-3000, 2000.

[21] J. V. Howarth, R. D. Keynes, and J. M. Ritchie, "Origin of Initial Heat Associated with a Single Impulse in Mammalian Non-Myelinated Nerve Fibres," *Journal of Physiology-London*, vol. 194, pp. 745, 1968.

[22] R. D. Keynes and J. M. Ritchie, "Initial Heat Production of Amphibian Myelinated Nerve Fibres," *Journal of Physiology-London*, vol. 210, pp. P29, 1970.

[23] M. Suzuki, V. Tseeb, K. Oyama, and S. Ishiwata, "Microscopic detection of thermogenesis in a single HeLa cell," *Biophysical Journal*, vol. 92, pp. L46-L48, 2007.

[24] W. Haeberle, M. Pantea, and J. K. H. Hoerber, "Nanometer-scale heat-conductivity measurements on biological samples," *Ultramicroscopy*, vol. 106, pp. 678-686, 2006.

[25] H. H. Roh, J. S. Lee, D. L. Kim, J. Park, K. Kim, O. Kwon, S. H. Park, Y. K. Choi, and A. Majumdar, "Novel nanoscale thermal property imaging technique: The 2 omega method. I. Principle and the 2 omega signal measurement," *Journal of Vacuum Science & Technology B*, vol. 24, pp. 2398-2404, 2006.

[26] R. K. P. Benninger, Y. Koc, O. Hofmann, J. Requejo-Isidro, M. A. A. Neil, P. M. W. French, and A. J. deMello, "Quantitative 3D mapping of fluidic temperatures within microchannel networks using fluorescence lifetime imaging," *Analytical Chemistry*, vol. 78, pp. 2272-2278, 2006.

[27] K. Dowling, S. C. W. Hyde, J. C. Dainty, P. M. W. French, and J. D. Hares, "2-D fluorescence lifetime imaging using a time-gated image intensifier," *Optics Communications*, vol. 135, pp. 27-31, 1997.

[28] O. Filevich and R. Etchenique, "1D and 2D temperature imaging with a fluorescent ruthenium complex," *Analytical Chemistry*, vol. 78, pp. 7499-7503, 2006.

[29] S. M. Jeon, J. Turner, and S. Granick, "Noncontact temperature measurement in microliter-sized volumes using fluorescent-labeled DNA oligomers," *Journal of the American Chemical Society*, vol. 125, pp. 9908-9909, 2003.

[30] D. Ross, M. Gaitan, and L. E. Locascio, "Temperature measurement in microfluidic systems using a temperature-dependent fluorescent dye," *Analytical Chemistry*, vol. 73, pp. 4117-4123, 2001.

[31] J. A. Stasiek and T. A. Kowalewski, "Thermochromic liquid crystals applied for heat transfer research," *Opto-Electronics Review*, vol. 10, pp. 1-10, 2002.

[32] S. W. Allison and G. T. Gillies, "Remote thermometry with thermographic phosphors: Instrumentation and applications," *Review of Scientific Instruments*, vol. 68, pp. 2615-2650, 1997.

[33] T. Glawdel, Z. Almutairi, S. Wang, and C. Ren, "Photobleaching absorbed Rhodamine B to improve temperature measurements in PDMS microchannels," *Lab on a Chip*, vol. 9, pp. 171-174, 2009.

[34] V. N. Hoang, G. V. Kaigala, and C. J. Backhouse, "Dynamic temperature measurement in microfluidic devices using thermochromic liquid crystals," *Lab on a Chip*, vol. 8, pp. 484-487, 2008.

[35] P. M. Kodzwa, C. J. Elkins, D. Mukerji, and J. K. Eaton, "Thermochromic liquid crystal temperature measurements through a borescope imaging system," *Experiments in Fluids*, vol. 43, pp. 475-486, 2007.

[36] T. Nozaki, T. Mochizuki, N. Kaji, and Y. H. Mori, "Application of Liquid-Crystal Thermometry to Drop Temperature-Measurements," *Experiments in Fluids*, vol. 18, pp. 137-144, 1995.

[37] C. D. Richards and R. F. Richards, "Transient temperature measurements in a convectively cooled droplet," *Experiments in Fluids*, vol. 25, pp. 392-400, 1998.

[38] T. B. Roth and A. M. Anderson, "A light transmission based liquid crystal thermography system," *Journal of Heat Transfer*, vol. 130, pp. 1-4, 2008.

[39] K. Kemnitz, N. Nakashima, K. Yoshihara, and H. Matsunami, "Temperature-Dependence of Fluorescence Decays of Isolated Rhodamine-B Molecules Adsorbed on Semiconductor Single-Crystals," *Journal of Physical Chemistry*, vol. 93, pp. 6704-6710, 1989.

[40] P. Low, N. Takama, K. Beomjoon, and C. Bergaud, "Using dried rhodamine B fluorescence for temperature characterization of sub-micron scale devices," in *TRANSDUCERS '07 & Eurosensors XXI. 2007 14th International Conference on Solid-State Sensors, Actuators and Microsystems*: IEEE, 2007, pp. 1055-1058.

[41] Y. Shiraishi, R. Miyamoto, X. Zhang, and T. Hirai, "Rhodamine-based fluorescent thermometer exhibiting selective emission enhancement at a specific temperature range," *Organic Letters*, vol. 9, pp. 3921-3924, 2007.

[42] S. Someya, S. Yoshida, Y. R. Li, and K. Okamoto, "Combined measurement of velocity and temperature distributions in oil based on the luminescent lifetimes of seeded particles," *Measurement Science & Technology*, vol. 20, 2009.

[43] O. Zohar, M. Ikeda, H. Shinagawa, H. Inoue, H. Nakamura, D. Elbaum, D. L. Alkon, and T. Yoshioka, "Thermal imaging of receptor-activated heat production in single cells," *Biophysical Journal*, vol. 74, pp. 82-89, 1998.

[44] S. M. Borisov and O. S. Wolfbeis, "Temperature-sensitive europium(III) probes and their use for simultaneous luminescent sensing of temperature and oxygen," *Analytical Chemistry*, vol. 78, pp. 5094-5101, 2006.

[45] C. F. Chapman, Y. Liu, G. J. Sonek, and B. J. Tromberg, "The Use of Exogenous Fluorescent-Probes for Temperature-Measurements in Single Living Cells," *Photochemistry and Photobiology*, vol. 62, pp. 416-425, 1995.

[46] M. Engeser, L. Fabbrizzi, M. Licchelli, and D. Sacchi, "A fluorescent molecular thermometer based on the nickel(II) high-spin/low-spin interconversion," *Chemical Communications*, pp. 1191-1192, 1999.

[47] C. Gota, K. Okabe, T. Funatsu, Y. Harada, and S. Uchiyama, "Hydrophilic Fluorescent Nanogel Thermometer for Intracellular Thermometry," *Journal of the American Chemical Society*, vol. 131, pp. 2766, 2009.

[48] C. Gota, S. Uchiyama, and T. Ohwada, "Accurate fluorescent polymeric thermometers containing an ionic component," *Analyst*, vol. 132, pp. 121-126, 2007.

[49] O. Haugen and T. H. Johansen, "Temperature dependent photoluminescence down to 4.2 K in EuTFC," *Journal of Luminescence*, vol. 128, pp. 1479-1483, 2008.

[50] K. Iwai, Y. Matsumura, S. Uchiyama, and A. P. de Silva, "Development of fluorescent microgel thermometers based on thermo responsive polymers and their modulation of sensitivity range," *Journal of Materials Chemistry*, vol. 15, pp. 2796-2800, 2005.

[51] S. Uchiyama, Y. Matsumura, A. P. de Silva, and K. Iwai, "Fluorescent molecular thermometers based on polymers showing temperature-induced phase transitions and labeled with polarity-responsive benzofurazans," *Analytical Chemistry*, vol. 75, pp. 5926-5935, 2003.

[52] C. Gota, S. Uchiyama, T. Yoshihara, S. Tobita, and T. Ohwada, "Temperature-dependent fluorescence lifetime of a fluorescent polymeric thermometer, Poly(N-isopropylacrylamide), labeled by polarity and hydrogen bonding sensitive 4-sulfamoyl-7-aminobenzofurazan," *Journal of Physical Chemistry B*, vol. 112, pp. 2829-2836, 2008.

[53] C. B. Muller, K. Weiss, A. Loman, J. Enderlein, and W. Richtering, "Remote temperature measurements in femto-liter volumes using dual-focus-Fluorescence Correlation Spectroscopy," *Lab on a Chip*, vol. 9, pp. 1248-1253, 2009.

[54] J. Sakakibara and R. J. Adrian, "Measurement of temperature field of a Rayleigh-Benard convection using two-color laser-induced fluorescence," *Experiments in Fluids*, vol. 37, pp. 331-340, 2004.

[55] V. Zeeb, M. Suzuki, and S. Ishiwata, "A novel method of thermal activation and temperature measurement in the microscopic region around single living cells," *Journal of Neuroscience Methods*, vol. 139, pp. 69-77, 2004.

[56] R. Samy, T. Glawdel, and C. L. Ren, "Method for microfluidic whole-chip temperature measurement using thin-film poly(dimethylsiloxane)/Rhodamine B," *Analytical Chemistry*, vol. 80, pp. 369-375, 2008.

[57] N. Millot, P. Borman, M. S. Anson, I. B. Campbell, S. J. F. Macdonald, and M. Mahmoudian, "Rapid determination of enantiomeric excess using infrared thermography," *Organic Process Research & Development*, vol. 6, pp. 463-470, 2002.

[58] M. A. Paulik, R. G. Buckholz, M. E. Lancaster, W. S. Dallas, E. A. Hull-Ryde, J. E. Weiel, and J. M. Lenhard, "Development of infrared imaging to measure thermogenesis in cell culture: Thermogenic effects of uncoupling protein-2, troglitazone, and beta-adrenoceptor agonists," *Pharmaceutical Research*, vol. 15, pp. 944-949, 1998.

[59] V. A. Patil and V. Narayanan, "Spatially resolved temperature measurement in microchannels," *Microfluidics and Nanofluidics*, vol. 2, pp. 291-300, 2006.

[60] T. Sikanen, T. Zwinger, S. Tuomikoski, S. Franssila, R. Lehtiniemi, C. M. Fager, T. Kotiaho, and A. Pursula, "Temperature modeling and measurement of an electrokinetic separation chip," *Microfluidics and Nanofluidics*, vol. 5, pp. 479-491, 2008.

[61] G. Galiana, R. T. Branca, E. R. Jenista, and W. S. Warren, "Accurate temperature imaging based on intermolecular coherences in magnetic resonance," *Science*, vol. 322, pp. 421-424, 2008.

[62] M. E. Lacey, A. G. Webb, and J. V. Sweedler, "Monitoring temperature changes in capillary electrophoresis with nanoliter-volume NMR thermometry," *Analytical Chemistry*, vol. 72, pp. 4991-4998, 2000.

[63] R. Klingeler, S. Hampel, and B. Buchner, "Carbon nanotube based biomedical agents for heating, temperature sensoring and drug delivery," *International Journal of Hyperthermia*, vol. 24, pp. 496-505, 2008.

[64] A. Vyalikh, A. U. B. Wolter, S. Dampel, D. Haase, M. Ritschel, A. Leonhardt, H. J. Grafe, A. Taylor, K. Kramer, B. Buchner, and R. Klingeler, "A carbon-wrapped nanoscaled thermometer for temperature control in biological environments," *Nanomedicine*, vol. 3, pp. 321-327, 2008.

[65] K. L. Davis, K. L. K. Liu, M. Lanan, and M. D. Morris, "Spatially Resolved Temperature-Measurements in Electrophoresis Capillaries by Raman Thermometry," *Analytical Chemistry*, vol. 65, pp. 293-298, 1993.

[66] K. L. K. Liu, K. L. Davis, and M. D. Morris, "Raman-Spectroscopic Measurement of Spatial and Temporal Temperature-Gradients in Operating Electrophoresis Capillaries," *Analytical Chemistry*, vol. 66, pp. 3744-3750, 1994.

[67] P. Chamarthy, S. V. Garimella, and S. T. Wereley, "Non-intrusive temperature measurement using microscale visualization techniques," *Experiments in Fluids*, vol. 47, pp. 159-170, 2009.

[68] K. Chung, J. K. Cho, E. S. Park, V. Breedveld, and H. Lu, "Three-Dimensional in Situ Temperature Measurement in Microsystems Using Brownian Motion of Nanoparticles," *Analytical Chemistry*, vol. 81, pp. 991-999, 2009.

[69] V. Hohreiter, S. T. Wereley, M. G. Olsen, and J. N. Chung, "Cross-correlation analysis for temperature measurement," *Measurement Science & Technology*, vol. 13, pp. 1072-1078, 2002.

[70] A. W. Lawson and E. A. Long, "On the Possible Use of Brownian Motion for Low Temperature Thermometry," *Physical Review*, vol. 70, pp. 220-221, 1946.

[71] J. S. Park, C. K. Choi, and K. D. Kihm, "Temperature measurement for a nanoparticle suspension by detecting the Brownian motion using optical serial sectioning microscopy (OSSM)," *Measurement Science & Technology*, vol. 16, pp. 1418-1429, 2005.

[72] A. Dodge, G. Turcatti, I. Lawrence, N. F. de Rooij, and E. Verpoorte, "A microfluidic platform using molecular beacon-based temperature calibration for thermal dehybridization of surface-bound DNA," *Analytical Chemistry*, vol. 76, pp. 1778-1787, 2004.

[73] C. Nellaker, U. Wallgren, and H. Karlsson, "Molecular beacon-based temperature control and automated analyses for improved resolution of melting temperature analysis using SYBR I Green chemistry," *Clinical Chemistry*, vol. 53, pp. 98-103, 2007.

[74] M. P. Raphael, J. A. Christodoulides, S. N. Qadri, S. A. Qadri, M. M. Miller, L. K. Kurihara, and J. M. Byers, "The use of DNA molecular beacons as nanoscale temperature probes for microchip-based biosensors," *Biosensors & Bioelectronics*, vol. 24, pp. 888-892, 2008.

[75] S. Chowdhury, C. Maris, F. H. T. Allain, and F. Narberhaus, "Molecular basis for temperature sensing by an RNA thermometer," *Embo Journal*, vol. 25, pp. 2487-2497, 2006.

[76] S. Chowdhury, C. Ragaz, E. Kreuger, and F. Narberhaus, "Temperature-controlled structural alterations of an RNA thermometer," *Journal of Biological Chemistry*, vol. 278, pp. 47915-47921, 2003.

[77] T. Waldminghaus, A. Fippinger, J. Alfsmann, and F. Narberhaus, "RNA thermometers are common in alpha- and gamma-proteobacteria," *Biological Chemistry*, vol. 386, pp. 1279-1286, 2005.

[78] J. Lee, A. O. Govorov, and N. A. Kotov, "Nanoparticle assemblies with molecular springs: A nanoscale thermometer," *Angewandte Chemie-International Edition*, vol. 44, pp. 7439-7442, 2005.

[79] W. Zhang, A. O. Govorov, and G. W. Bryant, "Semiconductor-metal nanoparticle molecules: Hybrid excitons and the nonlinear Fano effect," *Physical Review Letters*, vol. 97, 2006.

[80] A. Al Salman, A. Tortschanoff, M. B. Mohamed, D. Tonti, F. van Mourik, and M. Chergui, "Temperature effects on the spectral properties of colloidal CdSe nanodots, nanorods, and tetrapods," *Applied Physics Letters*, vol. 90, 2007.

[81] A. Narayanaswamy, L. F. Feiner, and P. J. van der Zaag, "Temperature dependence of the photoluminescence of InP/ZnS quantum dots," *Journal of Physical Chemistry C*, vol. 112, pp. 6775-6780, 2008.

[82] D. Valerini, A. Creti, M. Lomascolo, L. Manna, R. Cingolani, and M. Anni, "Temperature dependence of the photoluminescence properties of colloidal CdSe/ZnS core/shell quantum dots embedded in a polystyrene matrix," *Physical Review B*, vol. 71, 2005.

[83] G. W. Walker, V. C. Sundar, C. M. Rudzinski, A. W. Wun, M. G. Bawendi, and D. G. Nocera, "Quantum-dot optical temperature probes," *Applied Physics Letters*, vol. 83, pp. 3555-3557, 2003.

[84] X. H. Gao, L. L. Yang, J. A. Petros, F. F. Marshal, J. W. Simons, and S. M. Nie, "In vivo molecular and cellular imaging with quantum dots," *Current Opinion in Biotechnology*, vol. 16, pp. 63-72, 2005.

[85] S. Li, K. Zhang, J. M. Yang, L. W. Lin, and H. Yang, "Single quantum dots as local temperature markers," *Nano Letters*, vol. 7, pp. 3102-3105, 2007.

[86] X. Michalet, F. F. Pinaud, L. A. Bentolila, J. M. Tsay, S. Doose, J. J. Li, G. Sundaresan, A. M. Wu, S. S. Gambhir, and S. Weiss, "Quantum dots for live cells, in vivo imaging, and diagnostics," *Science*, vol. 307, pp. 538-544, 2005.

[87] M. Bruchez, M. Moronne, P. Gin, S. Weiss, and A. P. Alivisatos, "Semiconductor nanocrystals as fluorescent biological labels," *Science*, vol. 281, pp. 2013-2016, 1998.

[88] C. B. Murray, D. J. Norris, and M. G. Bawendi, "Synthesis and Characterization of Nearly Monodisperse Cde (E = S, Se, Te) Semiconductor Nanocrystallites," *Journal of the American Chemical Society*, vol. 115, pp. 8706-8715, 1993.

[89] X. G. Peng, J. Wickham, and A. P. Alivisatos, "Kinetics of II-VI and III-V colloidal semiconductor nanocrystal growth: "Focusing" of size distributions," *Journal of the American Chemical Society*, vol. 120, pp. 5343-5344, 1998.

[90] M. A. Hines and P. Guyot-Sionnest, "Synthesis and characterization of strongly luminescing ZnS-Capped CdSe nanocrystals," *Journal of Physical Chemistry*, vol. 100, pp. 468-471, 1996.

[91] M. Dahan, T. Laurence, F. Pinaud, D. S. Chemla, A. P. Alivisatos, M. Sauer, and S. Weiss, "Time-gated biological imaging by use of colloidal quantum dots," *Optics Letters*, vol. 26, pp. 825-827, 2001.

[92] D. Gerion, F. Pinaud, S. C. Williams, W. J. Parak, D. Zanchet, S. Weiss, and A. P. Alivisatos, "Synthesis and properties of biocompatible water-soluble silica-coated CdSe/ZnS semiconductor quantum dots," *Journal of Physical Chemistry B*, vol. 105, pp. 8861-8871, 2001.

[93] D. M. Willard, L. L. Carillo, J. Jung, and A. Van Orden, "CdSe-ZnS quantum dots as resonance energy transfer donors in a model protein-protein binding assay," *Nano Letters*, vol. 1, pp. 469-474, 2001.

[94] C. Y. Zhang, H. Ma, S. M. Nie, Y. Ding, L. Jin, and D. Y. Chen, "Quantum dot-labeled trichosanthin," *Analyst*, vol. 125, pp. 1029-1031, 2000.

[95] J. Aldana, Y. A. Wang, and X. G. Peng, "Photochemical instability of CdSe nanocrystals coated by hydrophilic thiols," *Journal of the American Chemical Society*, vol. 123, pp. 8844-8850, 2001.

[96] T. Pellegrino, L. Manna, S. Kudera, T. Liedl, D. Koktysh, A. L. Rogach, S. Keller, J. Radler, G. Natile, and W. J. Parak, "Hydrophobic nanocrystals coated with an amphiphilic polymer shell: A general route to water soluble nanocrystals," *Nano Letters*, vol. 4, pp. 703-707, 2004.

[97] B. Dubertret, P. Skourides, D. J. Norris, V. Noireaux, A. H. Brivanlou, and A. Libchaber, "In vivo imaging of quantum dots encapsulated in phospholipid micelles," *Science*, vol. 298, pp. 1759-1762, 2002.

[98] S. Pathak, S. K. Choi, N. Arnheim, and M. E. Thompson, "Hydroxylated quantum dots as luminescent probes for in situ hybridization," *Journal of the American Chemical Society*, vol. 123, pp. 4103-4104, 2001.

[99] Y. A. Wang, J. J. Li, H. Y. Chen, and X. G. Peng, "Stabilization of inorganic nanocrystals by organic dendrons," *Journal of the American Chemical Society*, vol. 124, pp. 2293-2298, 2002.

[100] J. R. Lakowicz, I. Gryczynski, Z. Gryczynski, K. Nowaczyk, and C. J. Murphy, "Time-resolved spectral observations of cadmium-enriched cadmium sulfide nanoparticles and the effects of DNA oligomer binding," *Analytical Biochemistry*, vol. 280, pp. 128-136, 2000.

[101] W. C. W. Chan, D. J. Maxwell, X. H. Gao, R. E. Bailey, M. Y. Han, and S. M. Nie, "Luminescent quantum dots for multiplexed biological detection and imaging," *Current Opinion in Biotechnology*, vol. 13, pp. 40-46, 2002.

[102] Y. P. Varshni, "Temperature Dependence of Energy Gap in Semiconductors," *Physica*, vol. 34, pp. 149, 1967.

[103] A. Joshi, K. Y. Narsingi, M. O. Manasreh, E. A. Davis, and B. D. Weaver, "Temperature dependence of the band gap of colloidal CdSe/ZnS core/shell nanocrystals embedded into an ultraviolet curable resin," *Applied Physics Letters*, vol. 89, pp. -, 2006.

[104] Y. H. Wu, K. Arai, and T. Yao, "Temperature dependence of the photoluminescence of ZnSe/ZnS quantum-dot structures," *Physical Review B*, vol. 53, pp. 10485-10488, 1996.

[105] O. Labeau, P. Tamarat, and B. Lounis, "Temperature dependence of the luminescence lifetime of single CdSe/ZnS quantum dots," *Physical Review Letters*, vol. 90, 2003.

[106] C. D. Donega, M. Bode, and A. Meijerink, "Size- and temperature-dependence of exciton lifetimes in CdSe quantum dots," *Physical Review B*, vol. 74, 2006.

[107] T. J. DiCiccio, M. A. Martin, S. E. Stern, and G. A. Young, "Information bias and adjusted profile likelihoods," *Journal of the Royal Statistical Society Series B-Methodological*, vol. 58, pp. 189-203, 1996.

[108] L. W. Lin, A. P. Pisano, and V. P. Carey, "Thermal bubble formation on polysilicon micro resistors," *Journal of Heat Transfer-Transactions of the ASME*, vol. 120, pp. 735-742, 1998.

[109] M. S. Watanabe, N. Kakuta, K. Mabuchi, and Y. Yamada, "Micro-thermocouple probe for measurement of cellular thermal responses," presented at IEEE Engineering in Medicine and Biology 27th Annual Conference, Shanghai, China, 2005.

[110] P. Kolodner and J. A. Tyson, "Microscopic fluorescent imaging of surface-temperature profiles with 0.01-degrees-C resolution," *Applied Physics Letters*, vol. 40, pp. 782-784, 1982.

[111] V. Romano, A. D. Zweig, M. Frenz, and H. P. Weber, "Time-resolved thermal microscopy with fluorescent films," *Applied Physics B-Photophysics and Laser Chemistry*, vol. 49, pp. 527-533, 1989.

[112] Seiichi Uchiyama, A. Prasanna de Silva, and K. Iwai, "Luminescent Molecular Thermometers " *Journal of Chemical Education*, vol. 83, pp. 720-727, 2006.

[113] D. L. Barton, "Fluorescent microthermographic imaging," *Istfa '94: Proceedings of the 20th International Symposium for Testing and Failure Analysis*, pp. 87-95, 1994.

[114] P. Kolodner and J. A. Tyson, "Remote thermal imaging with 0.7-μm spatial resolution using temperature-dependent fluorescent thin films," *Applied Physics Letters*, vol. 42, pp. 117-119, 1983.

[115] H. Kato, T. Nishizaka, T. Iga, K. Kinosita, and S. Ishiwata, "Imaging of thermal activation of actomyosin motors," *Proceedings of the National Academy of Sciences of the United States of America*, vol. 96, pp. 9602-9606, 1999.

[116] R. Savic, L. B. Luo, A. Eisenberg, and D. Maysinger, "Micellar nanocontainers distribute to defined cytoplasmic organelles," *Science*, vol. 300, pp. 615-618, 2003.

[117] W. C. W. Chan and S. M. Nie, "Quantum dot bioconjugates for ultrasensitive nonisotopic detection," *Science*, vol. 281, pp. 2016-2018, 1998.

[118] K. Hanaki, A. Momo, T. Oku, A. Komoto, S. Maenosono, Y. Yamaguchi, and K. Yamamoto, "Semiconductor quantum dot/albumin complex is a long-life and highly photostable endosome marker," *Biochemical and Biophysical Research Communications*, vol. 302, pp. 496-501, 2003.

[119] L. C. Mattheakis, J. M. Dias, Y. J. Choi, J. Gong, M. P. Bruchez, J. Q. Liu, and E. Wang, "Optical coding of mammalian cells using semiconductor quantum dots," *Analytical Biochemistry*, vol. 327, pp. 200-208, 2004.

[120] S. G. Nadler, M. A. Tepper, B. Schacter, and C. E. Mazzucco, "Interaction of the Immunosuppressant Deoxyspergualin with a Member of the Hsp70 Family of Heat-Shock Proteins," *Science*, vol. 258, pp. 484-486, 1992.

[121] B. B. Lowell and B. M. Spiegelman, "Towards a molecular understanding of adaptive thermogenesis," *Nature*, vol. 404, pp. 652-660, 2000.

[122] K. Fuxe, A. Rivera, K. X. Jacobsen, M. Hoistad, G. Leo, T. L. Horvath, W. Staines, A. De la Calle, and L. F. Agnati, "Dynamics of volume transmission in the brain. Focus on catecholamine and opioid peptide communication and the role of uncoupling protein 2," *Journal of Neural Transmission*, vol. 112, pp. 65-76, 2005.

[123] Z. B. Andrews, S. Diano, and T. L. Horvath, "Mitochondrial uncoupling proteins in the CNS: In support of function and survival," *Nature Reviews Neuroscience*, vol. 6, pp. 829-840, 2005.

[124] G. Mattiasson, M. Shamloo, G. Gido, K. Mathi, G. Tomasevic, S. L. Yi, C. H. Warden, R. F. Castilho, T. Melcher, M. Gonzalez-Zulueta, K. Nikolich, and T. Wieloch, "Uncoupling protein-2 prevents neuronal death and diminishes brain dysfunction after stroke and brain trauma," *Nature Medicine*, vol. 9, pp. 1062-1068, 2003.

[125] D. F. S. Rolfe and G. C. Brown, "Cellular energy utilization and molecular origin of standard metabolic rate in mammals," *Physiological Reviews*, vol. 77, pp. 731-758, 1997.

[126] M. F. Underhill and C. M. Smales, "The cold-shock response in mammalian cells: investigating the HeLa cell cold-shock proteome," *Cytotechnology*, vol. 53, pp. 47-53, 2007.

[127] M. B. Al-Fageeh, R. J. Marchant, M. J. Carden, and C. M. Smales, "The cold-shock response in cultured mammalian cells: Harnessing the response for the improvement of recombinant protein production," *Biotechnology and Bioengineering*, vol. 93, pp. 829-835, 2006.

[128] J. S. Hart, O. Heroux, and F. Depocas, "Cold Acclimation and the Electromyogram of Unanesthetized Rats," *Journal of Applied Physiology*, vol. 9, pp. 404-408, 1956.

[129] D. O. Foster and M. L. Frydman, "Tissue Distribution of Cold-Induced Thermogenesis in Conscious Warm-Acclimated Cold-Acclimated Rats Re-Evaluated from Changes in Tissue Blood-Flow - Dominant Role of Brown Adipose-Tissue in the Replacement of Shivering by Nonshivering Thermogenesis," *Canadian Journal of Physiology and Pharmacology*, vol. 57, pp. 257-270, 1979.

[130] D. Montiel and H. Yang, "Observation of correlated emission intensity and polarization fluctuations in single CdSe/ZnS quantum dots," *Journal Of Physical Chemistry A*, vol. 112, pp. 9352-9355, 2008.

[131] H. Cang, D. Montiel, C. S. Xu, and H. Yang, "Observation of Spectral Anisotropy of Gold Nanoparticles," *J. Chem. Phys.*, vol. 129, pp. 044503, 2008.